

## REPORT DOCUMENTATION PAGE

<p>1. Reporting burden for dissemination of information is estimated to average 1 hour per response, including the time for reviewing instructions, searching existing data sources, gathering and maintaining the data needed, and completing and reviewing the collection of information. Send comment regarding this burden estimate, or any other aspect of this collection of information, including suggestions for reducing this burden, to Washington Headquarters Services, Directorate for Information Operations and Reports (0704-0188) Washington, DC 20330.</p>			
2. AGENCY USE ONLY (Leave Blank)	2. REPORT DATE	3. REPORT TYPE AND DATES COVERED	
	04-18-08	Final (03-01-05 - 12-31-07)	
4. TITLE (and subtitle)		5. FUNDING NUMBERS	
Numerical Investigations of Active Flow Control for Low-Pressure Turbine Blades		FA9550-05-1-0166	
6. AUTHOR(S)		7. PERFORMING ORGANIZATION NAME(S) AND ADDRESS(ES)	
Dr. Hermann F. Fasel		Dept. of Aerospace and Mechanical Engineering, University of Arizona, Tucson, AZ 85721	
8. SPONSORING/MONITORING AGENCY NAME(S) AND ADDRESS(ES)		9. PERFORMING ORGANIZATION REPORT NUMBER	
AIR FORCE OFFICE OF SCIENTIFIC RESEARCH 875 N. Randolph St., Room 3112 Arlington, VA 22203 <i>Pfeff Jeffres/NA</i>		10. SPONSORING/MONITORING AGENCY REPORT NUMBER	
11. SUPPLEMENTARY NOTES The views, opinions and/or findings contained in this report are those of the author(s) and should not be construed as an official Department of the Army position, policy or decision, unless so designated by other documentation.			
12.a. DISTRIBUTION-AVAILABILITY STATEMENT		12.b. DISTRIBUTION CODE	
Approved for public release; distribution unlimited.			
13. ABSTRACT (Maximum 200 words)  The low-pressure turbine (LPT) produces the bulk net power in many jet engines. Low Reynolds number operating conditions in combination with aggressive designs can lead to laminar separation, which can cause significant reductions in turbine and overall engine performance. It was recognized that active flow control (AFC) applied to LPT blades can counter such unfavorable conditions, and that AFC could lead to considerable performance improvements as well as to a reduction in component weight. In collaboration with the experimentalists and with funding from AFOSR, we performed numerical investigations of AFC for LPT separation. We developed reliable simulation tools that allow us to perform high-fidelity simulations of entire turbine blades and of closely related model problems. A computationally less efficient but more versatile finite volume code was employed for simulations of the full geometry. Various AFC strategies such as pulsed vortex generator jets (VGJs), forcing through a two-dimensional slot (comparable to plasma actuators), or flow control by streamwise vortices (e.g. vortex generators) were explored. Using a highly efficient high-accuracy finite difference code we conducted in-detail studies of the VGJ actuation for laminar separation on a flat plate under LPT conditions. These simulations allowed us to extract the relevant physical mechanisms associated with VGJ control. Steady VGJs were shown to generate streamwise vortices but be less effective than pulsed VGJs. Pulsed VGJs were found to result in an accelerated transition to turbulence and to generate spanwise coherent structures which are amplified as a result of a flow instability.			
14. SUBJECT TERMS		15. NUMBER OF PAGES 89	
		16. PRICE CODE	
17. SECURITY CLASSIFICATION OR REPORT UNCLASSIFIED	18. SECURITY CLASSIFICATION ON THIS PAGE UNCLASSIFIED	19. SECURITY CLASSIFICATION OF ABSTRACT UNCLASSIFIED	20. LIMITATION OF ABSTRACT U

NSN 7540-01-280-5506

Standard Form 298 (Rev. 2-89)  
Prescribed by ANSI Std. Z39-18  
298-102

Enclosure 1

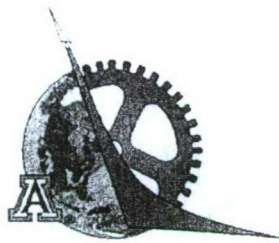
## **FINAL REPORT**

AFOSR GRANT FA 9550-05-1-0166

### **NUMERICAL INVESTIGATIONS OF ACTIVE FLOW CONTROL FOR LOW-PRESSURE TURBINE BLADES**

**Hermann F. Fasel, Andreas Gross, Wolfgang Balzer**

Department of Aerospace and Mechanical Engineering  
The University of Arizona  
Tucson, AZ 85721



Submitted to

Air Force Office of Scientific Research

March 2008

**20080516053**

## ABSTRACT

The low-pressure turbine (LPT) produces the bulk net power in many jet engines (Dunn 2001). Changes in LPT efficiency can significantly affect overall engine efficiency. Modern LPTs have to drive larger fans at lower fan speeds and at the same time be less complex and lighter. The goal is a reduction in stage solidity without compromising performance. LPTs must operate efficiently over a large range of Reynolds numbers (1,000,000 during takeoff and 25,000 during high altitude cruise). Low Reynolds number operating conditions in combination with aggressive designs can lead to laminar separation, which can cause significant reductions in turbine and overall engine performance. In fact, Sharma (1998) reported increases of the loss coefficient as high as 300%. Prediction and control of suction side separation, without sacrificing the benefits of higher loading, is therefore, crucial for improved engine designs.

It was recognized several years ago that active flow control (AFC) applied to LPT blades can counter such unfavorable conditions, and that AFC could lead to considerable performance improvements as well as to a reduction in component weight. In a broadly based experimental research program at the Air Force Research Laboratory (AFRL) at Wright-Patterson Air Force Base, Rivir and co-workers (Bons et al. 1999, 2000, 2001a/b, Sondergaard et al. 2002q/b) systematically explored the potential advantages of AFC using vortex generator jets (VGJs), both steady and pulsed, for LPT separation control. Pulsed blowing was shown to be much more efficient, requiring only a small fraction of the mass flow rate compared to the steady VGJs. Experimental observations (Eldredge and Bons 2004, Hansen and Bons 2006) show how steady angled injection results in the generation of streamwise vortices leading to free-stream momentum entrainment. These vortices maintain their coherence over a larger downstream distance than the counter rotating vortices generated by vertical injection and, therefore, facilitate more free-stream entrainment. Pulsed blowing was shown to cause early boundary layer transition, especially when the jets were employed near the "natural" (uncontrolled) separation location (Bons et al. 2001a/b).

In collaboration with the experimentalists and with funding from AFOSR, we performed numerical investigations of AFC for LPT separation. We chose a two-pronged approach: A computationally less efficient but more versatile finite volume code was employed for simulations of the full geometry. Two- and three-dimensional simulations with and without turbulence models predicted the flow with various degrees of accuracy. Various AFC strategies using e.g. forcing through a two-dimensional slot or three-dimensional VGJ actuation as well as open- and closed-loop control were explored. In-detail studies of the VGJ actuation for a model problem were performed with a highly efficient finite difference code. These high-resolution DNS results shed light on some of the physical mechanisms responsible for the effectiveness of VGJs.

## TABLE OF CONTENTS

ABSTRACT .....	ii
1. INTRODUCTION.....	1
1.1 Technical Background.....	1
1.2 Research at the University of Arizona .....	3
2. NUMERICAL SIMULATIONS OF THE PACKB AND L1M LOW-PRESSURE TURBINE BLADES INVESTIGATED EXPERIMENTALLY AT AFRL .....	6
2.1 Case Description.....	6
2.2 Computational Method .....	6
2.3 Computational Grid and Boundary Conditions.....	7
2.4 Uncontrolled Flow .....	9
2.4.1 Simulation Strategy .....	9
2.4.2 Grid Resolution Study .....	11
2.4.3 Uncontrolled Flow, L1M Blade .....	16
2.5 Controlled Flow .....	20
2.5.1 2-D Simulations for PackB Geometry.....	20
2.5.2 3-D Simulations for PackB Geometry.....	23
2.5.3 3-D Simulations for L1M Geometry.....	39
2.6 Closed-Loop Control .....	44
2.6.1 Open-Loop Control Parameter Study for L1M Blade .....	45
2.6.2 Self-Adaptive Closed-Loop PD Controller.....	47
2.6.3 Neural Network Based Model .....	51
3. DIRECT NUMERICAL SIMULATIONS OF ACTIVE FLOW CONTROL USING VORTEX GENERATOR JETS FOR MODEL GEOMETRY .....	55
3.1 Case Description .....	55
3.2 Computational Method .....	55
3.3 Computational Domain and Boundary Conditions .....	57
3.4 Results .....	60
3.4.1 Uncontrolled "Natural" Flow .....	60
3.4.2 Steady VGJs; Flat Plate Geometry .....	63
3.4.3 Pulsed VGJs; Flat Plate Geometry .....	66
3.4.4 Pulsed VGJs; Curved Wall Geometry .....	71
3.4.5 Effect of Hole Spacing.....	75
3.4.6 Additional Results .....	80
4. SUMMARY AND CONCLUSION .....	83
5. CONFERENCES, PRESENTATIONS, AND PAPERS .....	84
REFERENCES .....	85

## 1. INTRODUCTION

### 1.1 Technical Background

The low-pressure turbine (LPT) produces the bulk net power in many jet engines (Dunn 2001). Changes in LPT efficiency can significantly affect overall engine efficiency. Modern LPTs have to drive larger fans at lower fan speeds and at the same time be less complex and lighter. The goal is a reduction in stage solidity without compromising performance. LPTs must operate efficiently over a large range of Reynolds numbers (1,000,000 during takeoff and 25,000 during high altitude cruise). Low Reynolds number operating conditions in combination with aggressive designs can lead to laminar separation, which can cause significant reductions in turbine and overall engine performance. In fact, Sharma (1998) reported increases of the loss coefficient as high as 300%. Prediction and control of suction side separation, without sacrificing the benefits of higher loading, is therefore, crucial for improved engine designs.

It was recognized several years ago that active flow control (AFC) applied to LPT blades can counter such unfavorable conditions, and that AFC could lead to considerable performance improvements as well as to a reduction in component weight. In a broadly based experimental research program at the Air Force Research Laboratory (AFRL) at Wright-Patterson Air Force Base, Rivir and co-workers (Bons et al. 1999, 2000, 2001a/b, Sondergaard et al. 2002q/b) systematically explored the potential advantages of AFC using vortex generator jets (VGJs), both steady and pulsed, for LPT separation control. Using pulsed VGJs, the momentum deficit at a Reynolds number of 25,000 could be reduced by 65% (Bons et al. 2000). Sondergaard et al. (2002b) showed that the losses encountered when the blade spacing was increased by 50% could also be successfully eliminated with pulsed VGJs. The jets were employed at a skew angle of 90° (the angle formed by the projection of the jet onto the surface and the free stream direction) and a pitch angle of 30° (the angle formed by the jet and the surface). Various jet velocity amplitudes and duty-cycles (ratio of jet on-time to pulsing period) were investigated. Both, steady and pulsed blowing was reported to be effective in reducing separation losses. However, pulsed blowing was shown to be much more efficient, requiring only a small fraction of the mass flow rate compared to the steady VGJs. Experimental observations (Eldredge and Bons 2004, Hansen and Bons 2006) show how steady angled injection results in the generation of streamwise vortices leading to free-stream momentum entrainment. These vortices maintain their coherence over a larger downstream distance than the counter rotating vortices generated by vertical injection and, therefore, facilitate more free-stream entrainment. Pulsed blowing was shown to cause early boundary layer transition,

especially when the jets were employed near the “natural” (uncontrolled) separation location (Bons et al. 2001a/b).

Extensive experimental studies of LPT separation control using steady and pulsed plasma actuators were conducted by Corke and co-workers (Corke and Post 2005, Huang et al. 2006a/b). In these experiments a drastic reduction in boundary layer separation on the suction side of the LPT blade was achieved. Pulsed actuation was shown to be much more efficient than steady actuation and required a lower overall energy input. A modulation frequency that generated approximately two spanwise vortices over the extent of the separated region was found to be optimal.

Rizzetta and Visbal employed a high-order-accurate compressible code for three-dimensional implicit large eddy simulations (ILES) investigating separation control by pulsed VGJs (Rizzetta and Visbal 2003, 2004, 2005) and Plasma actuators (Rizzetta and Visbal 2007) for the same PackB blade. Pulsed VGJs were found to result in an earlier transitioning of the suction side boundary layer. The effect of the Plasma actuator was modeled by a volume force. Pulsed counter-flow plasma actuation was found to be most effective. The effectiveness of the latter was attributed to the generation of spanwise vortical structures that entrain high momentum fluid from the free-stream.

Although the experiments at AFRL by Rivir and co-workers have convincingly demonstrated the potential benefits of VGJs and provided considerable insight into the associated fluid dynamics and in spite of our considerable progress in understanding the fundamental physical mechanisms many questions remain, in particular, when realistic turbine operating environments are being considered. The underlying physics are highly complex, as both *unsteady separation* and *transition* mechanisms are at work interactively. Each of these areas by itself, *transition* from laminar to turbulent flow and *unsteady separation*, belong to the least understood areas of flow physics even without the complications of realistic turbine environments. The main understanding of transition is based on the so-called linear regime, where the amplitudes of the instability waves are small and, as a consequence, the so-called linear stability theory can be employed for modeling. For LPT applications, as a consequence of the strong streamwise amplification of the disturbance waves, the disturbances quickly reach very large amplitudes. The strong amplification is due to the streamwise adverse pressure gradients, the convex wall curvature (suction side of blade), and the elevated free stream turbulence in turbine operations (when compared to external free flow conditions). Therefore, linear theory is not applicable (in particular for high free stream turbulence levels) and the transition mechanisms are not “linear” (not of Tollmien-Schlichting type). Rather, the transition process is of a “by-pass” nature (Morkovin 1969), that is the linear stages are by-passed. Due to the non-linearity and the non-uniqueness of the by-pass mechanisms, slight changes in

"initial" conditions (say, operating conditions) can result in drastically different breakdown-to-turbulence scenarios.

The fundamental understanding of separation is almost as incomplete as that of transition, especially when the separation process is unsteady and three-dimensional as in the application to be investigated here. The unsteadiness is introduced by the pulsing of the VGJs and/or by the naturally present large "coherent" flow structures, which result from the instability of the separated "base flow". The three-dimensionality is caused by the fact that the jets are injected through small holes that are relatively far apart from each other (several hole diameters). For time-dependent, three-dimensional separation, even the definition of unambiguous "separation" criteria is a challenge (see for example the Moore, Rott, Sears (MRS) criterion, (Schlichting and Gersten 2000)). Again, as for transition, boundary layer separation under such conditions is a highly non-linear, non-unique process that exhibits a strong sensitivity to "initial" conditions.

Clearly, for LPT separation, the two mechanisms interact non-linearly, thereby considerably expanding the range of non-uniqueness. Separation, in general, strongly accelerates transition, while transition, in general, delays or can even prevent separation. However, to what degree they affect each other depends on the details of the "initial" conditions and is strongly influenced by the geometry (roughness, wall curvature, wall temperature, jet geometry, frequency and amplitudes of forcing, etc.). Thus, when both of these non-linear, non-unique mechanisms are at work at the same time, as is the case for the LPT, surprises are likely, both positive and negative. For example, when frequencies and amplitudes of the pulsed blowing are "just right", the effectiveness of separation control is indeed stunning, requiring a very small energy input. In other instances, although unintentional and often due to a lack of understanding, AFC is not effective in the sense that separation is not prevented/delayed or that an unacceptable energy input is required. Therefore, in light of the complex physics that are at work in active flow control for LPTs using vortex generator jets, it is obvious that a better understanding of the most relevant physical mechanisms needs to be achieved before this technology can be transitioned successfully into practice and to ensure safe, reliable and effective operation.

## 1.2 Research at the University of Arizona

During the previous years with funding from AFOSR a research program at the University of Arizona in collaboration with AFRL (Rivir, Sondergaard) and Brigham Young University (Bons) focused on extracting the relevant physics of separation control by VGJs for LPT applications. The hope was that, with the synergism between the experimental effort and our numerical simulations,

the chances for major advances in the understanding of the relevant physical mechanisms would be significantly increased. While narrow parameter ranges may be explored more easily in the experiments, larger changes of the flow parameters (e.g. geometry, locations of the AFC devices, forcing frequencies and amplitudes etc.) can be more easily investigated with numerical simulations. Most importantly, numerical simulations can provide insight into flow details that is not possible in experiments. The synergism of simulations and experiments has proven to be highly fruitful: We have made major strides towards understanding some of the most relevant physical aspects of separation control using VGJs as discussed in section 2 and 3.

We investigated separation control for the PackB LPT blade of the experiments by Rivir and co-workers using a high-order compressible code (Postl et al. 2003, 2004, Gross and Fasel 2005a/b). The laminar separation bubble that forms in the uncontrolled case was found to shed spanwise coherent vortices in a self-excited fashion that break down to turbulence upstream of the trailing edge. Since the disturbances that seed the spanwise structures were not introduced deliberately into the flow and since the wake shedding was self-sustained one may speculate that the separated flow was absolutely unstable (Theofilis and Sherwin 2004, Abdessemed et al. 2004, 2006). It was shown in 3-D simulations that the flow can be successfully controlled with pulsed blowing through a slot (Gross and Fasel 2005a/b), with pulsed VGJs, or with streamwise vortices. Pulsed VGJs resulted in earlier boundary layer transition compared to the uncontrolled flow. Depending on the actuation parameters, spanwise coherent structures were found to reside in the turbulent flow at reattachment. Separation control by harmonic blowing through a spanwise slot was found to enhance the spanwise structures and delay transition. In fact, this strategy was found to be even more effective than control by pulsed VGJs. Streamwise vortices were found to be very effective means for separation control. They are, however, different from the spanwise structures not amplified by the flow which makes this type of flow control inefficient. We also carried out simulations of the L1M geometry where we investigated separation control by pulsed VGJs and harmonic forcing through a slot (Gross and Fasel 2007b)

In addition, we performed highly resolved three-dimensional simulations of a flat plate model geometry subjected to the same streamwise pressure gradient as measured in the experiments of Rivir and co-workers. The deliberate geometric simplification (exclusion of the effects of curvature) allowed us to investigate separation control by VGJs using fully resolved DNS with up to 200 million grid points. "Weak" steady VGJs were found to result in by-pass transition while "stronger" VGJs were found to generate steady streamwise vortices that greatly enhanced free-stream entrainment. The effectiveness of pulsed VGJs was attributed partially to an earlier transitioning of the flow. The dominant mechanism, however, and this was unexpected, was the generation of coherent vortical

structures that greatly enhanced free-stream entrainment. The development of these structures was found to be a direct consequence of the in-phase actuation of the VGJs which introduces a 2-D perturbation component. The exploitation of hydrodynamic instabilities of the flow by the pulsed actuation explains why this type of flow control is significantly more effective than steady VGJ actuation. In particular, we found that pulsed actuation becomes very effective when the 2-D inviscid shear layer instability of the inflectional velocity profiles in the separated flow region is exploited.

## **2. NUMERICAL SIMULATIONS OF THE PACKB AND L1M LOW-PRESSURE TURBINE BLADES INVESTIGATED EXPERIMENTALLY AT AFRL**

We have taken a two-pronged approach aimed at uncovering the fundamental mechanisms for active control of separation for LPT blades. In the first approach, simulations were performed for the flow around the entire LPT blades that was investigated experimentally by Rivir and co-workers at AFRL (Bons et al. 2001, 2002, Sondergaard et al. 2002a, Bons et al. 2005) where we investigated separation control by pulsed vortex generator jets (VGJs), by pulsed blowing through a slot, and by streamwise vortices. In the second approach, a laminar boundary layer on a flat or curved plate was subjected to the same streamwise pressure gradient as measured in the experiments. This simpler approach allowed us to focus the available computational resources on resolving all relevant scales of motion from the laminar to the turbulent flow regime and to extract the relevant physics associated with separation control by steady and pulsed VGJs. The comparison of the flat and curved plate results will allow us to extract the effect of curvature on VGJ actuation.

### **2.1 Case Description**

The geometries chosen for our studies are the Pratt and Whitney PackB LPT blade and the L1M blade (Bons et al. 2005). Both blades have an inflow angle of 55° and a design exit angle of 30° (both measured from the plane of the cascade). Our simulations were set up according to the earlier experiments by Rivir and co-workers (Bons et al. 2001, 2002, Sondergaard et al. 2002a) and Bons et al. (Bons et al. 2005) where upstream wakes and surface roughness were not considered. This deliberate simplification, when compared to the environment in real jet engines, allows for an easier extraction of the flow physics with or without VGJs used for flow control. The PackB simulations were carried out for a Reynolds number based on axial chord of 25,000. The ratio of blade spacing,  $d$ , and axial chord,  $C_x$ , was 0.88 for the original cascade of Rivir and co-workers and 1.1 for a cascade with 25% larger blade spacing. The L1M simulations are for a Reynolds number of 20,000. The blade spacing was 1.01. In our simulations, both the number of blades and the span were assumed to be infinite (periodic boundary conditions) and the level of free-stream turbulence intensity was zero.

### **2.2 Computational Method**

For the computations of entire LPT blades we employ a finite volume code based on the

compressible Navier-Stokes equations in curvilinear coordinates that was developed in our group (Gross and Fasel 2008). The convective terms are computed with high-order-accurate (up to ninth-order-accurate) upwind schemes based on a weighted essentially non-oscillatory extrapolation of the characteristic variables and the Roe scheme (Gross and Fasel 2002). A fourth-order-accurate discretization is employed for computing the viscous terms and a second-order-accurate implicit Adams-Moulton method is employed for advancing the governing equations in time. For implicit large eddy simulations (ILES), the convective terms are discretized with a second-order-accurate total variation diminishing scheme and the viscous terms are computed with a second-order-accurate discretization. For flow simulation methodology (FSM) simulations (Speziale 1998, Fasel et al. 2002a) the 1998  $k-\omega$  turbulence model equations are solved based on a second-order-accurate discretization and the Reynolds-stresses are computed from the explicit algebraic stress model (EASM) by Rumsey and Gatski (2001). The code was parallelized using the message passing interface (MPI) and scales very well on large numbers of processors (Fig. 1).

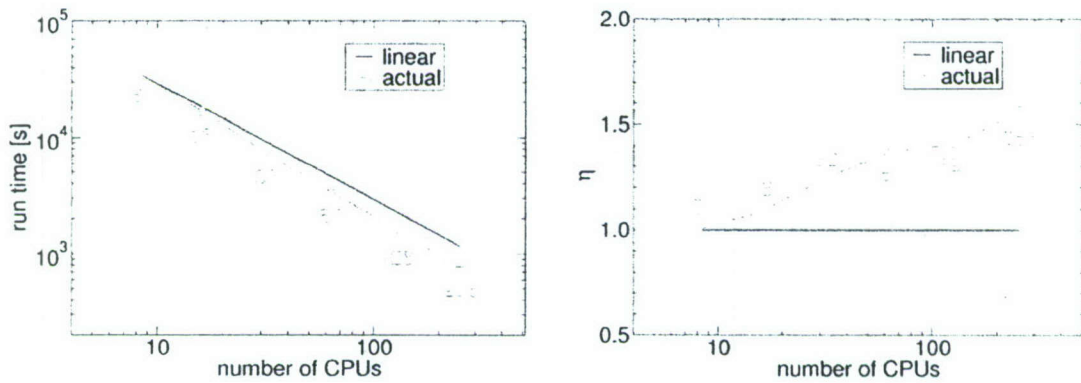


**Fig. 1: Parallel scalability of compressible code for test case with 3 million cells. Simulations were performed on IBM P4+ at NAVO. Shown are speed-up (left) and parallel efficiency (right).**

### 2.3 Computational Grid and Boundary Conditions

In our simulations, both the number of blades and the span were assumed to be infinite (periodic boundary conditions). Following Rizzetta and Visbal4 (2003, 2004, 2005) who performed a grid size study for the PackB blade, the spanwise extent of the computational domain,  $\Delta Z$ , was set to  $0.2C_x$ . We generated grids with 3 different grid resolutions, coarse, medium, and fine. Each of these grids consisted of 5 blocks, where the block structure is shown in Fig. 2. The grids were generated such that continuity of neighboring cells at the boundaries of each block was ensured. Grid points were clustered near the wall, in the separated flow region on the suction side of the

blade, and in the wake. Table 1 summarizes the block and total grid resolutions of the 3 different grids employed for the present simulations.

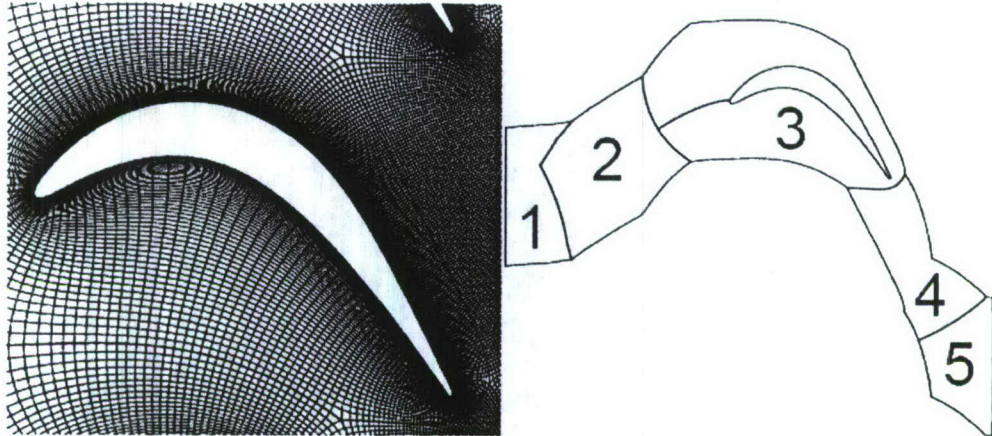


*Fig. 2: Computational grid for PackB LPT simulations.*

	block	coarse	medium
1	5×15	10×30	20×60
2	10×10	20×20	40×40
3	250×50	500×100	1000×150
4	130×50	260×100	520×200
5	52×55	105×110	210×220
total	352,560	2,824,000	19,392,000

*Tab. 1: Block grid resolutions for PackB LPT simulations.*

An identical block structure with block grid resolutions of 10x30, 20x20, 500x100, 260x100, 104x110 and a total of 2.82million cells was employed for the L1M simulations.

The no-slip condition was applied at the wall except at the forcing slot/hole where a wall-normal forcing velocity was prescribed. The wall was treated as adiabatic. A characteristics based boundary condition was applied at the in- and outflow boundaries (Gross 2007a). Periodicity conditions were employed at all other boundaries.

## 2.4 Uncontrolled Flow

### 2.4.1 Simulation Strategy

We first explored the different flow control strategies that are available to us: (1) ninth-order-accurate scheme, no model (direct numerical simulation, DNS), (2) fifth-order-accurate scheme with flow simulation methodology (FSM), or (3) second-order-accurate scheme, no model (implicit large eddy simulation, ILES). These tests were carried out for the PackB geometry with the medium resolution grid.



*Fig. 3: Iso-contours of spanwise vorticity for PackB. 3-D (left) and 2-D result (right).*

Instantaneous contours of spanwise vorticity for the PackB blade at the design blade spacing obtained from a 3D DNS and a 2-D simulation (here referred to as 2D DNS) are shown in Fig. 3. The laminar boundary layer separates approximately at the beginning of the uncovered turning. As a result of a hydrodynamic instability of the separated boundary layer (inflectional velocity profile, Kelvin-Helmholtz instability, possibly a global instability (Theofilis and Sherwin 2004, Abdessamed et al. 2004, 2006)) disturbances are strongly amplified, leading to a roll-up of the separated boundary layer and the formation of spanwise vortical structures. These structures increase wall normal mixing and cause flow reattachment in the mean, when flow quantities are averaged in time. In the 2-D simulation all 3-D motion is suppressed, of course, and the intensity of the 2-D structures is over-predicted. In the 3-D simulations, the flow is allowed to transition. As a consequence, the eddy-viscosity introduced by small scale turbulent structures weakens the coherence of the 2-D structures thereby delaying reattachment.

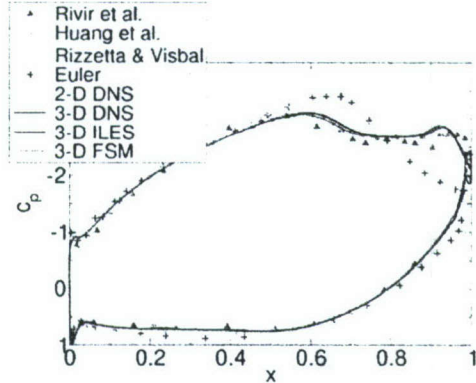


**Fig. 4: Wall pressure coefficient for PackB.**

Time-averaged curves for the wall pressure coefficient,  $c_p$ , are shown in Fig. 4. Also included in Fig. 4 are measurements by Bons et al. (2001), Sondergaard et al. (2002a), and Huang et al. (2003, 2006a) as well as results from a 3-D ILES by Rizzetta and Visbal (2003). Compared to the experiments, the 2-D results show a somewhat later separation and a slightly larger plateau pressure in the separated region. The “hump” near the trailing edge for the 2-D calculation which is not visible in the 3-D simulations appears to be an “artifact” of strong 2-D structures as discussed above. Otherwise, the 2-D calculations predict the mean flow wall pressure surprisingly well.

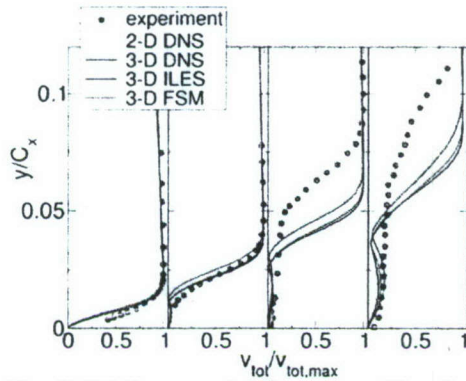


**Fig. 5: Wall-normal velocity profiles for PackB.**

Time-averaged wall normal profiles of total velocity averaged in the spanwise direction are shown in Fig. 5. The computed results are compared with experimental data (Bons et al. 2001, Sondergaard et al. 2002a). At 68% and 77%, the computed velocity profiles obtained from the 3-D simulations match the experimental data quite well while at 84% and 92% the thickness of the separation bubble is under-predicted. A fundamental difference in the setup between the simulations and the experiment may be the reason for the observed differences. A likely difference

is the free stream turbulence intensity which is zero in our simulations (Bons, private communication), or differences in the setup with respect to e.g. the inflow and outflow angles, or imperfections of the blade. Further insight will be obtained from future investigations including the effect of FST. The bubble thickness is under-predicted in the 2-D simulations indicating overly strong mixing due to the large spanwise structures.

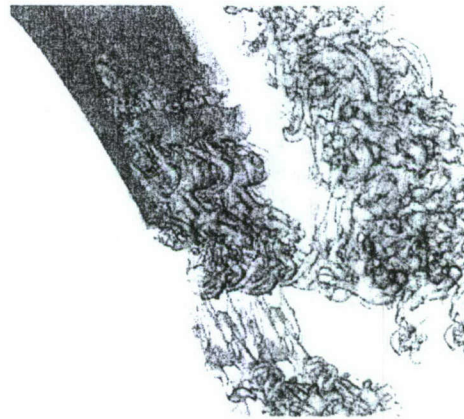


*Fig. 6: 3-D DNS of PackB (uncontrolled). Iso-surface of  $Q=1$ . Perspective view near trailing edge.*

A visualization of instantaneous data obtained from a 3-D DNS is shown in Fig. 6. Shown are iso-surfaces of the Q-criterion (Hunt et al. 1988). A positive Q-criterion indicates areas where rotation dominates strain. The 2-D spanwise structures that periodically develop as a consequence of the shear layer instability become unstable with respect to 3-D disturbances. These disturbances initially cause a 3-D modulation of the 2-D structures, and eventually lead to a rapid breakdown to turbulence upstream of the trailing edge.

#### 2.4.2 Grid Resolution Study

We also carried out a grid resolution study for the PackB (the grid resolutions are listed in Tab.1). For these simulations we employed the ninth-order accurate scheme. A comparison of instantaneous flow visualizations is shown in Fig. 7. The most pronounced difference between the three results is the increasing amount of random 3-D turbulent motion as the grid resolution is increased, or in other words, the decrease in dimension of the smallest resolved structures.

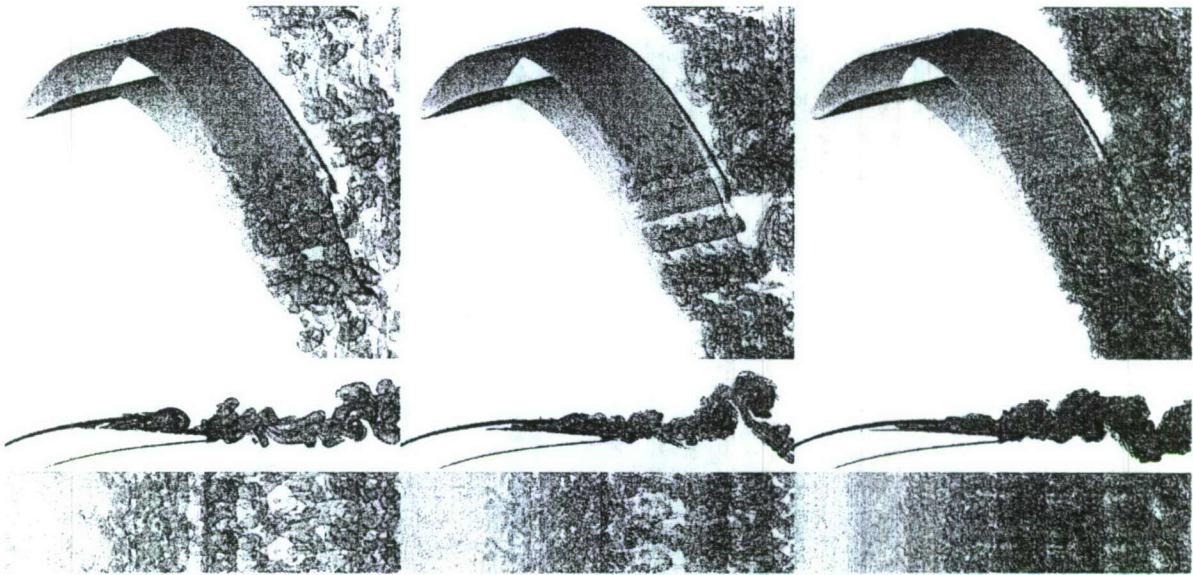


**Fig. 7: Iso-surfaces of vortex identification criterion,  $Q = 1$ , and iso-contours of spanwise vorticity,  $w_z$ , at  $z=0$ . From left to right: Coarse, medium, fine grid solution. From top to bottom: Perspective view of blade (computational domain was repeated once in spanwise direction), side view of wake, and top down view of wake.**

Distributions of the wall-pressure coefficient,  $c_p(x,z,t)$  averaged in time and in the spanwise direction are shown in Fig. 8a. Averages were computed over time intervals of 15 (coarse and medium grid) and 4 (fine grid). For comparison, experimental data by Bons et al. (2001), Sondergaard et al. (2002a), and Huang et al. (2003, 2006a) were included. The simulation results are in excellent agreement with the measurements for the wall pressure coefficient. The good agreement of the wall pressure coefficient coincides with a good agreement of the streamfunction distribution (of the temporal and spanwise average of the flow) as shown in Fig. 8b. Size and shape of the laminar separation bubble nearly coincide for all 3 grid resolutions.

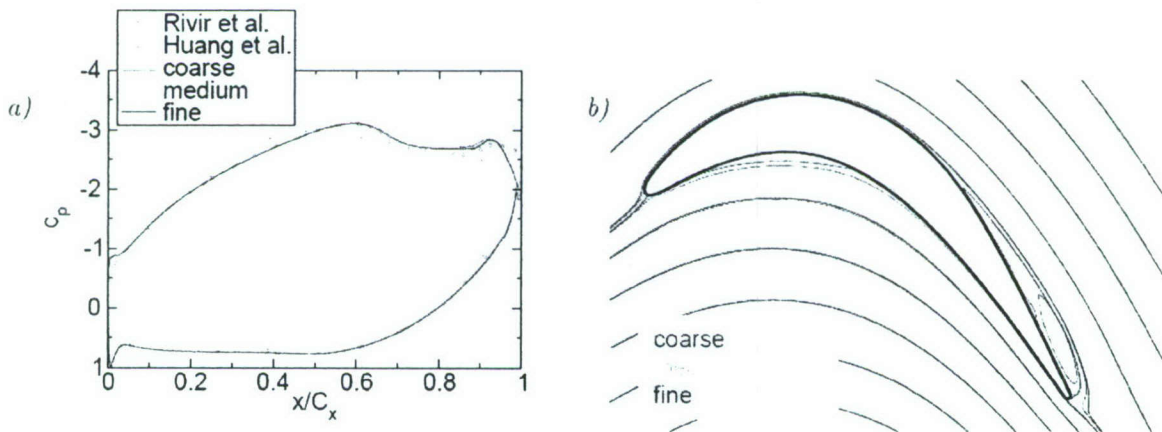


**Fig. 8: a) Wall pressure coefficient,  $c_p$ , and b) Iso-contours of streamfunction.**

The near wall grid resolution in wall units is shown in Fig. 9. The arc length,  $s$ , was measured from the leading edge of the blade. The wall-normal grid resolution in wall units,  $n^+$ , is close to or smaller than 1 for all cases. When resorting to Fig. 8 one may argue that the better resolution does not improve the quality of the time-averaged solution (in the separation bubble region) because the turbulent motion is mainly confined to the wake region. A second observation is that the wake turbulence appears to be concentrated in "lumps". In analogy to other wake flows, the blade is shedding counter-rotating coherent structures. In top-down views of the wake the spanwise coherent structures appear as spanwise concentrations of small-scale turbulent motion.

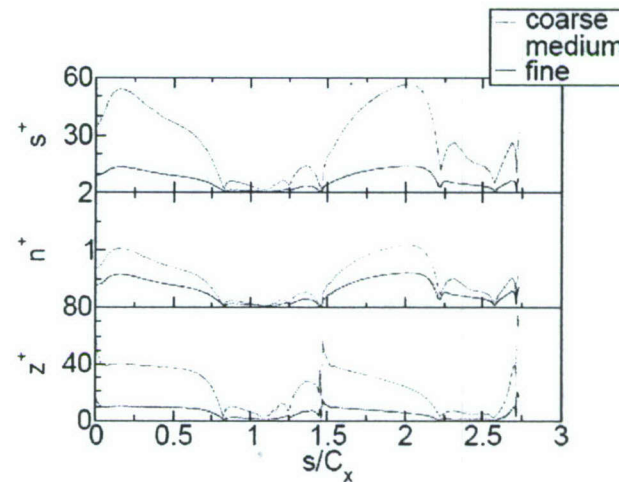


**Fig. 9: Streamwise,  $s^+$ , wall-normal,  $n^+$ , and spanwise,  $z^+$ , near-wall grid line spacing in wall units.**

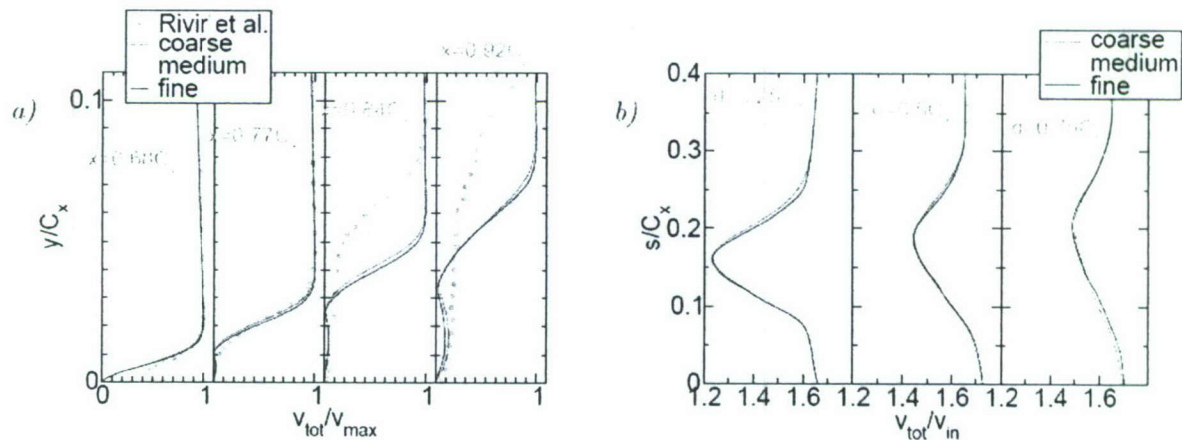


**Fig. 10: a) Wall-normal profiles and b) wake velocity profiles (distance to trailing edge,  $d$ , is measured in downstream direction, which is at  $30^\circ$  angle to cascade plane; profiles are taken perpendicular to outflow direction).**

Wall-normal velocity profiles (normalized by the local velocity maxima) and wake profiles (normalized by the inlet velocity and taken perpendicular to the design exit flow direction at a distance  $d$  from the trailing edge) averaged in  $t$  and  $z$  are shown in Fig. 10. The profiles show good grid convergence and good agreement with the experimental data at  $x = 68\%C_x$  and  $77\%C_x$ . At this point, we cannot offer a conclusive explanation for the pronounced mismatch of the velocity profiles at  $x/C_x = 0.84$  and  $0.92$ . Transition and separation are both very sensitive to freestream turbulence and geometric imperfections. In the simulation the inflow turbulence is zero and the surface is close to perfectly smooth. Such ideal conditions cannot be obtained in the experiment. From our simulations we know that an earlier transition will weaken the spanwise structures ("rollers") and result in an enlarged separation. This statement is based on a comparison of earlier 2D and 3D simulations where we found the extent of the separated flow region to be smaller in the former. This was argued to be due to the stronger wall-normal momentum exchange facilitated by "pure" 2-D "rollers" when compared to spanwise structures superimposed with small scale 3D motion. Conversely, as the current simulations were found to be underresolved in the reattachment region this may result in an underprediction of turbulent mixing in the simulations and an overprediction of the strength of the spanwise structures and a reduction of the bubble size. One may think of other possible explanations for the mismatch between the numerical and experimental data. Until proven, all of these arguments will, however, remain speculative. At this point we, therefore, acknowledge the mismatch and postpone further investigations that may proof one or another argument.

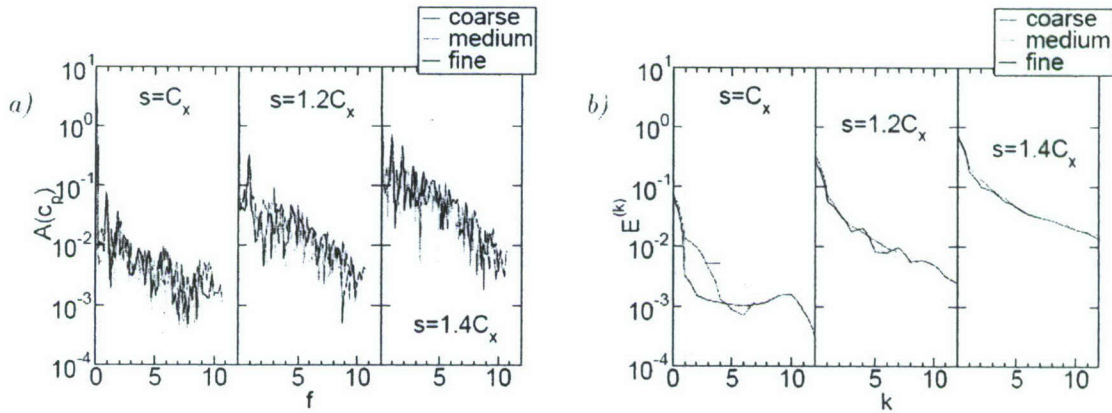


**Fig. 11: a) Frequency spectra of mode  $k = 0$  of wall pressure coefficient,  $c_p$ . b) Modal “energy contents”.**

The flow was also analyzed with respect to the dynamics of the flow structures in the separation bubble. In Fig. 11a, frequency spectra of mode  $k = 0$  of the wall pressure coefficient,  $c_p$ , are shown for 3 downstream locations. The fundamental ( $f=1$ ) grows in amplitude by a factor of roughly 10

between  $s/C_x = 1$  and  $1.4$ . For  $s/C_x = 1.4$ , the spectrum begins to fill up as the flow transitions to turbulence and higher harmonics of appreciable amplitude appear. The low frequency part of the spectrum which contains the bulk of the kinetic energy is approximately identical in all three cases, again indicating grid convergence of the solution (with respect to the flow dynamics of the separation bubble).

Following Bernoulli, the fluctuating kinetic energy can be related to the pressure fluctuations at the wall (where the velocities are zero and  $p$  is the temporal average of the static pressure). Then the wall pressure coefficient can be regarded as some measure of the fluctuating kinetic energy contents of the flow. Therefore, by computing Fourier transforms of the wall pressure coefficient the modal "energy contents" of the flow can be estimated (Fig. 11b). At  $s = C_x$  the flow is mainly two-dimensional (2D) and most of the energy is in the spanwise mode  $k=0$ , which is the spanwise average of the data. A non-zero  $k = 0$  amplitude indicates the presence of 2D disturbances or spanwise vortical structures. At  $s = 1.2C_x$  and  $s = 1.4C_x$  the higher modes fill up indicating the onset of transition. Also, the energy spectra coincide, thus indicating grid independence of the solution. As the modal energy contents does not drop down to machine accuracy for  $k >> 0$  the turbulence energy spectrum is not fully resolved for all of the three cases. The fact that the energy spectra nevertheless coincide may be attributed to the diffusion characteristics of the numerical scheme used for the current simulations. Margolin and Rider (2002) showed that certain upwind schemes exhibit similar diffusion characteristics at the smallest resolved scales as standard sub-grid scale turbulence models used in LES.

On the medium resolution grid, we also computed Favre-averaged turbulence quantities, the Reynolds stresses, the turbulence kinetic energy, and the dissipation. The fluctuating velocity components were computed relative to a mean flow that was averaged over a time interval of 20 and which was also averaged in the spanwise direction. Spanwise averages of the Reynolds stresses are shown in Fig. 12. The Reynolds stresses obtain considerable magnitudes in the reattachment region near the trailing edge of the blade and in the wake. The normal stresses are not of the same magnitude indicating anisotropy of the turbulence and hinting at the presence of coherent structures. This is supported by the observation that the  $u'v'$  component is larger than the  $v'w'$  and  $w'u'$  components.

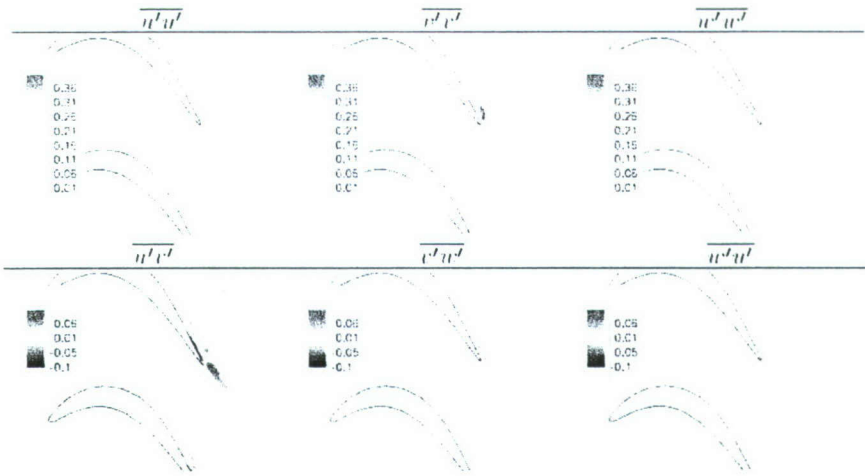


**Fig. 12: Favre-averaged Reynolds stresses for medium resolution grid.**

Finally, the “physical” grid resolution can be estimated by considering the ratio of local grid resolution,  $\max(\Delta x, \Delta y, \Delta z)$ , to the local Kolmogorov length scale,  $L_k$ , which is the length scale of the smallest dissipating eddies in the flow. Results for the medium resolution grid are shown in Fig. 13. The grid line spacing in the reattachment region is approximately 10 times the Kolmogorov length scale.

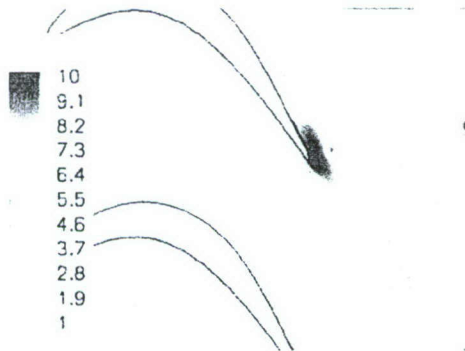


**Fig. 13: “Physical” grid resolution,  $\max(\Delta x, \Delta y, \Delta z)/L_k$ , for medium resolution grid.**

#### 2.4.3 Uncontrolled Flow, L1M Blade

We also performed simulations of the L1M blade (Bons et al. 2005) using our flow simulation methodology (FSM). The L1M blade was designed for an integrated flow control and exhibits a large separated flow region in the uncontrolled case. Compared to the PackB which is more aft-loaded the L1M blade is characterized by a more balanced loading. Also the blade spacing is larger ( $0.88C_x$  for PackB and  $1.01C_x$  for L1M). Results from our simulations are shown in Figs. 14 and 15.

Although, compared with the PackB blade (Fig. 8) the extent of the separated flow region is considerably increased the same phenomena as for the PackB blade can be observed. Spanwise vortices form in the separated boundary layer. A secondary instability mechanism leads to the amplification of 3-D disturbances resulting in the appearance of 3-D structures near the trailing edge and in the wake (Fig. 15). The 3-D structures weaken the coherence of the spanwise structures, resulting in a considerable enlargement of the separation bubble.



**Fig. 14: 3-D FSM simulation of L1M. Spanwise vorticity (left) and streamfunction (right).**



**Fig. 15: 3-D FSM of L1M (uncontrolled). Iso-surface of  $Q=1$ .**

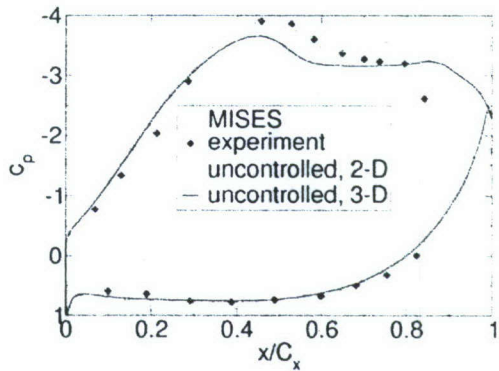


**Fig. 16: Wall pressure coefficient for L1M.**

A comparison of the computed wall pressure coefficient, with experimental data (Bons et al. 2005) and data obtained from the MISES design code (Clark 2004) is shown in Fig. 16. The agreement between the 3-D simulation and the MISES prediction is adequate. Again, a pronounced “hump” for the 2-D computation near the trailing edge can be detected which can be attributed to overly strong spanwise structures. The later separation in the 2-D case causes the pressure in the separated flow region (“pressure plateau”) to be lower than in the 3-D case. The significantly smaller size of the separation bubble in the experiments (Fig. 5 in (Reimann et al. 2006)) can likely be attributed to the FSTI of about 3% in the experiment.

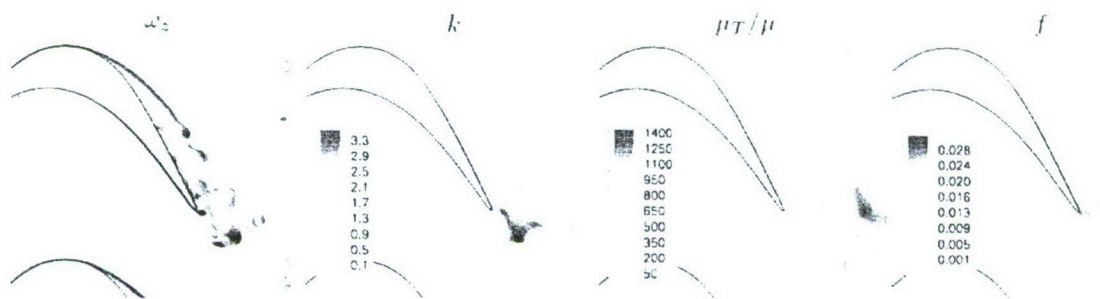


**Fig. 17: Iso-contours of spanwise vorticity, turbulence kinetic energy, eddy viscosity, and contribution function for FSM of L1M blade.**

To allow for a more detailed analysis of the 3-D simulation iso-contourlines of different quantities in the spanwise plane  $z = 0$  are shown in Fig. 17. Turbulence kinetic energy,  $k$ , is produced in the separated flow region and in the wake. This is in qualitative agreement with our PackB results (Fig. 12). The eddy viscosity distribution approximately follows the  $k$ -distribution. The model contribution,  $f$ , is clearly related to prominent instantaneous flow features. It is larger in areas of turbulence

production (regions of shear, strain and rotation) and approximately 2% in the separated flow region and in the wake and almost zero on the pressure side of the blade and near the leading edge. Starting from the separation location the model contribution gradually increases in the downstream direction in the separated boundary layer. In this region FSM changes from DNS ( $f = 0$ ) to LES ( $0 < f < 1$ ) and thus structures in the aft part of the blade and in the wake have to be interpreted as coherent structures.

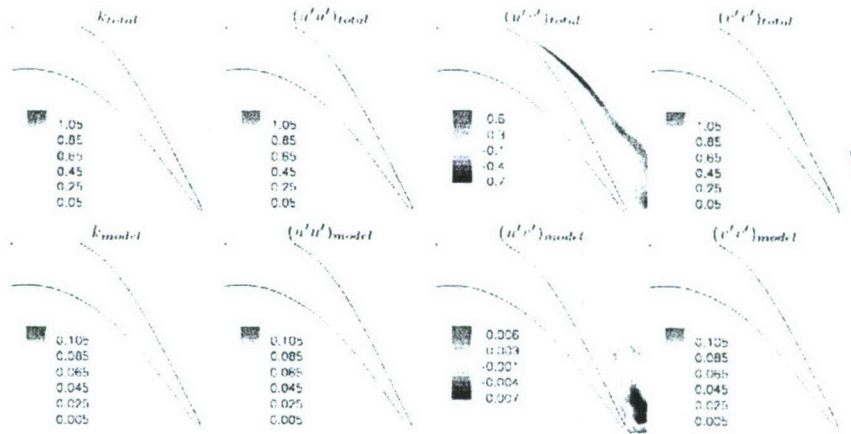


**Fig. 18: Total and unresolved (modeled) turbulence kinetic energy and Reynolds stresses.**

Based on these results for the uncontrolled PackB and L1M geometries we concluded that our numerical tools (ILES and/or FSM) are capable of performing accurate LPT flow simulations. Turbulence quantities were time-averaged over a time interval of  $\Delta t = 7$ . In Fig. 18 spanwise averages of the total and unresolved (modeled) turbulence kinetic energy,  $k$ , and the total Reynolds stresses are shown in the top row. The total quantities were computed by summation of the time-averaged resolved and unresolved (model contribution) quantities. Spanwise averages of the unresolved quantities are shown in the bottom row. Only the region in the immediate vicinity of the separation bubble is shown because the time-averages are even poorer in the wake and do not allow for a meaningful analysis. In general, the model contribution is larger in the wake than in the separated flow region on the suction side of the blade. The following approximate numbers can be extracted from Fig. 18: Maxima of the ratios of the unresolved to total turbulence kinetic energy,  $u'u'$ , and  $v'v'$  are about 10% and the maximum ratio of the unresolved to total Reynolds shear stress,  $u'v'$ , is about 1%.

Finally, the time-averaged contribution function is shown in Fig. 19a. When considering the physical grid resolution,  $\Delta/L_k$ , (Fig. 19b) it can be concluded that for a true DNS, which would require a  $\Delta/L_k$  of order 1, the grid resolution near the trailing edge is not fine enough by a factor of about 15. This justifies the hybrid turbulence modeling approach taken here.

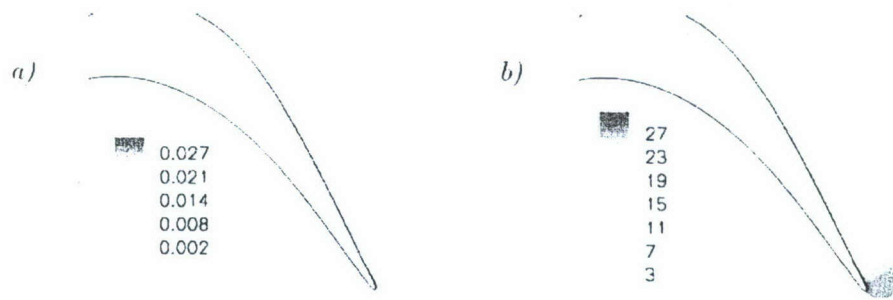


**Fig. 19: Uncontrolled flow. a) Model contribution and b) physical grid resolution.**

## 2.5 Controlled Flow

### 2.5.1 2-D Simulations for PackB Geometry

In the beginning, we investigated if the shear layer instability of the separated boundary layer could be exploited for controlling separation for the PackB blade at a 25% increased blade spacing. As 3-D simulations are expensive for AFC parameter studies we decided to employ 2-D simulations for studying the response of the flow to reduced duty cycle actuation through a slot. With a blade spacing of  $d/C_x=1.1$  (the previous blade spacing was 0.88) the separated region, and hence the performance losses, are much larger. The area enclosed by the  $c_p$ -curves (Fig. 20) is larger than for the design blade spacing (Fig. 8) since each individual blade has to exert a larger aerodynamic force on the flow. Important parameters associated with the forcing are the momentum coefficient,  $c_\mu$ , the blowing ratio,  $B$  (ratio of maximum forcing velocity to free-stream velocity), and the duty cycle,  $\tau$  (ratio of forcing on-time to forcing period).

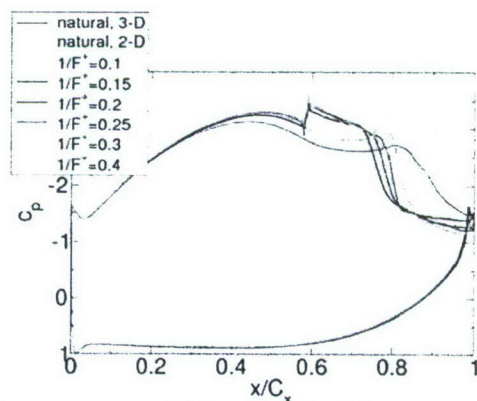


**Fig. 20: Wall pressure coefficient for PackB at 25% larger blade spacing.**

In the experiments by Rivir and co-workers it was found that forcing with a reduced duty cycle of the pulsed blowing resulted in a very effective flow control (Bons et al. 2001, 2002, Sondergaard et al. 2002a). In the experiments, blowing ratios in the range of 1 to 4 and duty cycles in the range of 1 to 50% were explored. Here, wall-normal blowing through a slot of width  $b=0.01C_x$ , located at 58% axial chord, with blowing ratio  $B=1$  and duty cycle of  $\tau=10\%$  was explored for different forcing frequencies. The momentum coefficient was  $c_\mu=10^{-3}$ . Instantaneous visualizations of the controlled flow for two different forcing frequencies are shown in Fig. 21.



**Fig. 21:** Iso-contours of spanwise vorticity for PackB at 25% larger blade spacing. Control with  $F^+=2.5$  (left) and 6.67 (right).

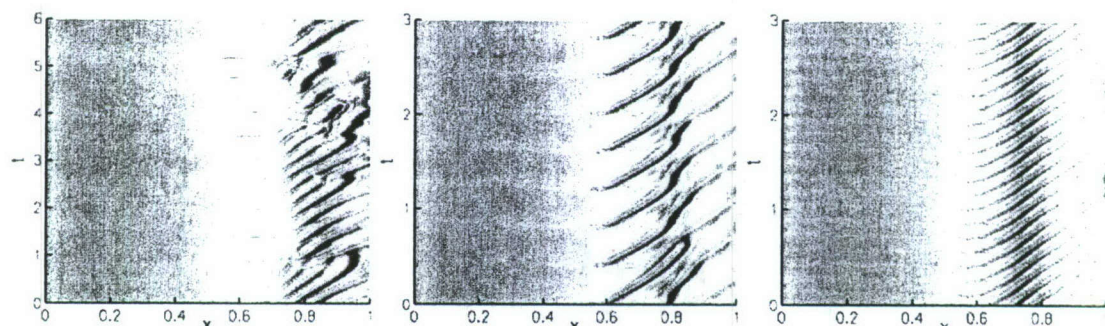


**Fig. 22:**  $t$ - $x$  diagrams of wall vorticity on suction side of PackB blade(25% larger blade spacing) ( $\omega_z=-1200 \dots 1200$ ) for uncontrolled case (left) and controlled cases with  $F^+=2.5$  (center) and 6.67 (right).

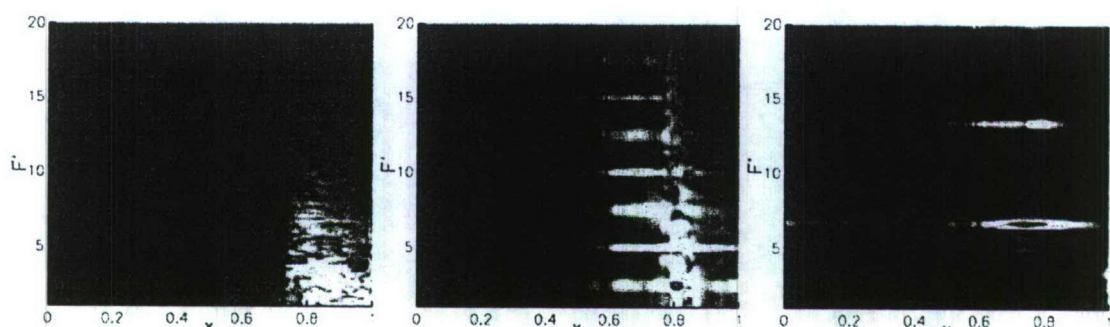


**Fig. 23:** Fourier transform of wall vorticity on suction side of PackB blade ( $A(\omega_z)=0 \dots 400$ ) for uncontrolled case (left) and controlled cases with  $F^+=2.5$  (center) and 6.67 (right).

Fig. 22 shows time-space diagrams of the wall vorticity for the uncontrolled case and 2 controlled cases. The (uncontrolled) flow shows little periodicity and a very broad frequency spectrum (Fig. 23). More energy is contained in the lower frequency range of the spectrum than for the design blade spacing (not shown) since the separation bubble and the associated length scales are larger. For the controlled cases, separation is reduced considerably (Figs. 20 & 22). The shortest separated flow region is obtained when the flow is forced with  $F^*=6.67$ . For this forcing frequency the introduced disturbances are most amplified as shown in Fig. 24(left).

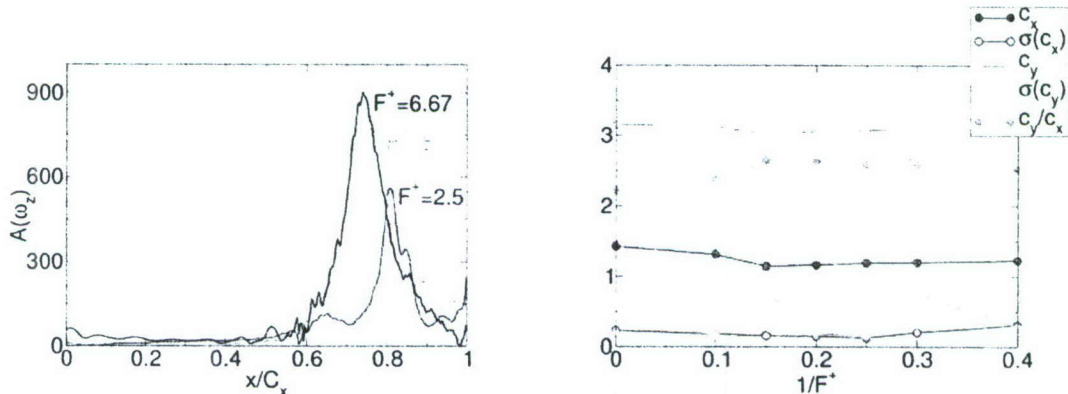
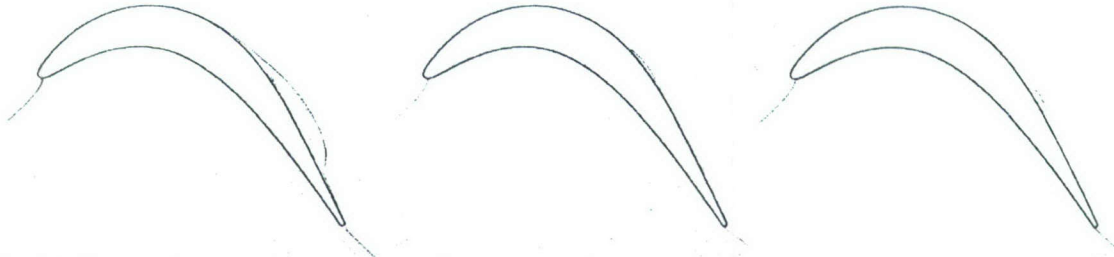


Fig. 24: PackB blade at 25% larger blade spacing. Left: Amplitude of the fundamental disturbance (forcing frequency) for three different forcing frequencies. Amplitudes were obtained from Fourier transform of wall vorticity. Right: Time-averages and standard deviations,  $\sigma$ , of aerodynamic coefficients,  $c_x$  and  $c_y$ ,  $1/F^*=0$  result is for uncontrolled case.

The time-averaged ratio of the non-dimensionalized normal and axial aerodynamic forces,  $c_y/c_x$ , is increased by as much as 19.4% for forcing with  $F^*=6.67$  (Fig. 24(right)). A simple momentum balance shows that this parameter is a measure for the total flow turning (difference between cascade inflow and outflow angle). When considering the individual aerodynamic forces it becomes clear that the gain in aerodynamic performance is mostly due to a reduction of  $c_x$ . The separation bubble is located near the trailing edge of the blade in the area of uncovered turning where the pressure recovery takes place. In the uncontrolled case, the flow cannot negotiate the adverse pressure gradient and separates, resulting in a pressure distribution that is above the design pressure in the aft part of the blade (Fig. 20). Due to the curved geometry of the blade, this loss shows up mainly in the  $c_x$ -coefficient. When the control is turned on, separation is reduced, and the pressure at the aft part of the blade is lowered. When the flow "locks in" to the forcing, as for example for  $F^*=3.33$  and  $F^*=6.67$ , the dynamic aerodynamic loads on the blade can become very large (Fig. 24). This can be avoided by forcing with  $F^*=5$  (a frequency that is slightly lower than the most amplified frequency). For this case the fundamental ( $F^*=5$ ) and higher harmonic ( $F^*=10$ ) are both close to  $F^*=6.67$  and are both amplified. The loss in aerodynamic performance due to this compromise is very small. The increase in lift over drag of the controlled cases can be associated

with a larger circulation and a smaller time-averaged separation bubble (Fig. 25) when compared with the uncontrolled case.



*Fig. 25: Streamfunction iso-contours for uncontrolled case (left) and controlled cases with  $F^+=2.5$  (left) and 6.67 (right) for PackB blade at 25% larger blade spacing.*

### 2.5.2 3-D Simulations for PackB Geometry

We investigated controlling the flow using pulsed vortex generator jets (VGJs) and using harmonic blowing through a slot. All studies of the controlled flow were conducted using the medium resolution grid assuming that the grid resolution study for the uncontrolled flow was proof enough that the medium resolution grid was also sufficiently well resolved for the cases with flow control. For the VGJ control we employed a reduced duty cycle forcing

$$v_f(t) = \begin{cases} Br_{in} & \text{if } 0 \leq t \leq \tau T \\ 0 & \text{if } \tau T < t < T \end{cases}$$

$$v_f(t+T) = v_f(t).$$

with a duty cycle of  $\tau=10\%$  (experiments (Bons et al. 2001, 2002):  $\tau = 50\%$ ). The forcing period was  $T = 0.2$  (the forcing frequency in the experiments was  $f = 10\text{Hz}$  which corresponds to a non-dimensional forcing frequency of 0.843 and a period of 1.19) and the blowing ratio which is defined as the maximum jet exit velocity divided by the inlet velocity,  $B$ , was 1 and 2 (experiments:  $B = 0:2$ ). The forcing period in the simulations was based on the 2-D simulations where we determined the most effective forcing frequency for controlling the separation bubble. The holes were placed at  $x=0.630C_x$  (same as in experiments), had approximate hole dimensions,  $\Delta s \times \Delta z$ , of  $0.0330 \times 0.0438$ , and were resolved with  $7 \times 7$  cells (experiments: hole diameter  $1\text{mm}=0.001/0.1778=0.00562$ ). The hole spacing was identical to the spanwise extent of the domain,  $\Delta Z = 0.2C_x$ , meaning that only one VGJ was computed. The hole spacing in the experiments was  $0.0562C_x$ , which makes the disturbance input more continuous in the spanwise direction (or in the terminology used here more 2-D). The jets were issued into the boundary layer at a  $30^\circ$  pitch angle and a  $90^\circ$  skew angle (same as in experiments).

For the case with harmonic blowing a slot of width  $b = \Delta s = 0.0144$  which was resolved with 3 cells was located at  $x = 0.622C_x$ . The wall-normal velocity component over the slot surface was

$$v_f(t) = \frac{1}{2} \left( 1 + \cos 2\pi \frac{t}{T} \right) B v_{in}$$

The forcing period was 0.2 and the blowing ratio was 0.1. The momentum coefficient,

$$c_\mu = \frac{\int \int \left( \frac{1}{T} \int \rho_f v_f^2 dt \right) dx dz}{\frac{1}{2} \rho_{in} v_{in}^2 C_x \Delta Z}$$

is a measure for the energy expense of the forcing. It is integrated over the forcing slot/ jet exit hole and over one forcing period, T. For the subsonic cases considered here the density variation can be neglected. The momentum coefficient is computed relative to the zero forcing signal and not, as is the case for the oscillatory momentum coefficient,  $\langle c_\mu \rangle$ , relative to the time-averaged forcing signal. For reduced duty cycle blowing through circular holes with radius, R, and spanwise hole spacing,  $\Delta z$  and assuming a parabolic velocity distribution over the hole (this approach was chosen here),

$$v_f(r, t) = \begin{cases} B v_{in} \left( 1 - \frac{r^2}{R^2} \right) & 0 < t < \tau T \\ 0 & \text{otherwise} \end{cases}$$

the momentum coefficient can be computed as

$$c_\mu = \frac{2}{3} \frac{\pi R^2}{C_x \Delta Z} \tau B^2$$

Here, the cross-sectional area of the holes was taken as  $\pi ab \sin 30^\circ = \pi 0.0330/2 0.0438/2 0.5 = 5.68 \cdot 10^{-4}$  (experiments:  $2.48 \cdot 10^{-5}$ ). For harmonic blowing through a slot the momentum coefficient becomes

$$c_\mu = \frac{3}{4} \frac{b}{C_x} B^2$$

Alternatively, the flow was also controlled by steady streamwise vortices. In the experiment this would be accomplished by e.g. vortex generators or isolated roughness elements, by a corrugated wall, or by vortex generator jets. We decided to generate streamwise vortices with volume forces acting in a circular segment between the angular positions  $\theta_1 = 53.12^\circ$  and  $\theta_2 = 39.48^\circ$  as shown in Fig. 26.

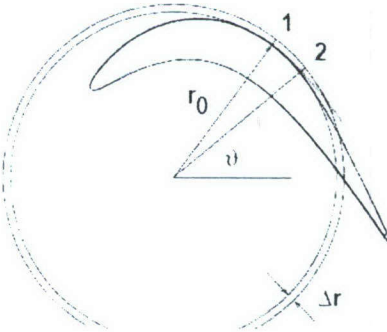


**Fig. 26: Temporal and spanwise average of uncontrolled flow. Iso-contours of spanwise vorticity,  $\omega_z$ . Also indicated is area where streamwise vortices are forced for  $\Delta r = 0.025$ .**

In particular for  $r_0 < r < r_0 + \Delta r$  the volume force is applied in the radial and spanwise directions. The primary spanwise wavelength that is being forced is  $\lambda_z = 2\Delta Z/k$  where  $k$  is the number of streamwise vortices per  $\Delta Z$ . The radius of  $r$  is measured from the origin ( $x_0 = 0.2834$ ,  $y_0 = 0.1896$ ) and the radius  $r_0 = 0.5484$  was chosen such that the resulting circle was closely aligned with the suction side wall of the turbine blade between  $\theta_1$  and  $\theta_2$ . The volume forces were added to the right-hand-sides of the 3 momentum equations. A momentum coefficient can be computed as

$$c_\mu = \frac{\int \int \int \rho f dxdydz}{\frac{1}{2} \rho_{in} v_{in}^2 C_x \Delta Z}$$

where

$$f = \sqrt{f_r^2 + f_z^2} = A^* \sin \left( \pi \frac{r - r_0}{\Delta r} \right) \sqrt{1 + \left( 4 \cos^2 \left[ \pi \frac{r - r_0}{\Delta r} \right] - 1 \right) \sin^2 \left( k \pi \frac{z}{\Delta Z} \right)}$$

and  $\Delta r \times \Delta z/k$  is the wall-normal and spanwise extent of one vortex. The momentum coefficient then becomes

$$c_\mu = 2(\vartheta_1 - \vartheta_2) \frac{kA}{C_x^2 \Delta Z} \int_0^{\Delta Z/k} \int_{r_0}^{r_0 + \Delta r} f r dr dz$$

where  $A$  is the non-dimensional volume forcing amplitude (or acceleration). This equation can be integrated numerically. For our simulations, we chose  $\Delta r = 0.025$  which is roughly 2 times the local boundary layer thickness. Table 2 provides a summary of the momentum coefficients employed in the various simulations. Since the suction side boundary layer of the turbine blade is convex, streamwise vortices are not amplified in the boundary layer (no Görtler instability). This may explain why relatively large momentum coefficients were required for generating streamwise vortices. As mentioned earlier, streamwise vortices of similar intensity can likely be generated in the experiment by passive means (geometry modifications). On the contrary spanwise vortices (which can be generated by harmonic blowing and suction through a slot or by plasma actuators), are amplified by

the shear layer instability and, therefore, require comparatively low momentum coefficients.

	Spanwise wavelength, $\lambda_z$	Amplitude	Momentum coefficient, $c_p$
VGJs, 30°_ pitch and 90°_ skew angle	0.2	B = 1, $\tau=0.1$	$7.6 \cdot 10^{-4}$
	0.2	B = 2, $\tau=0.1$	
slot, harmonic blowing	N.A.	B = 0.1	$1.1 \cdot 10^{-4}$
VGJs, wall normal harmonic blowing	0.2	B = 0.39	$2.2 \cdot 10^{-4}$
	0.0667	B = 0.23	$2.2 \cdot 10^{-4}$
streamwise vortices, steady volume force	0.2	A = 1	$3.5 \cdot 10^{-3}$
		A = 10	$3.5 \cdot 10^{-2}$
	0.1	A = 1	$4.4 \cdot 10^{-3}$
		A = 10	$4.4 \cdot 10^{-2}$
	0.0667	A = 1	$4.7 \cdot 10^{-3}$
		A = 10	$4.7 \cdot 10^{-2}$
	0.05	A = 1	$4.4 \cdot 10^{-3}$
		A = 10	$4.4 \cdot 10^{-2}$

Tab. 2: Summary of different flow control cases for Pack LPT blade.

Instantaneous visualizations of the controlled flows are shown in Fig. 27. All simulations were initialized with the uncontrolled flow. All three control techniques appear to prevent or at least reduce

flow separation. Control with VGJs seems to lead to an earlier transitioning of the flow. With  $B = 1$  spanwise coherent structures appear. For  $B = 2$  such structures are not immediately evident. Control with harmonic blowing through a slot results in the formation of pronounced spanwise structures (or "rollers") and a transition delay compared with the uncontrolled flow. Small scale motion appears considerably farther downstream in the wake.

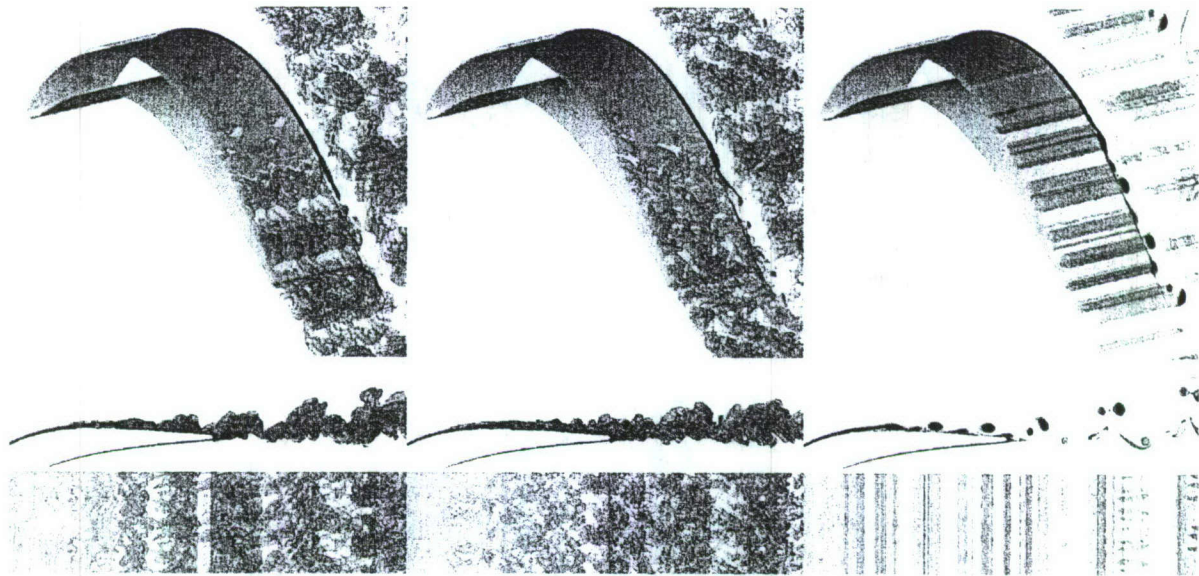


**Fig. 27:** Iso-surfaces of vortex identification criterion,  $Q = 1$ , and iso-contours of spanwise vorticity,  $\omega_z$ . From left to right: Jets ( $B = 1$ ), jets ( $B = 2$ ), and slot ( $B = 0.1$ ). From top to bottom: Perspective view of blade (computational domain was repeated once in spanwise direction), side view of wake, and top down view of wake.

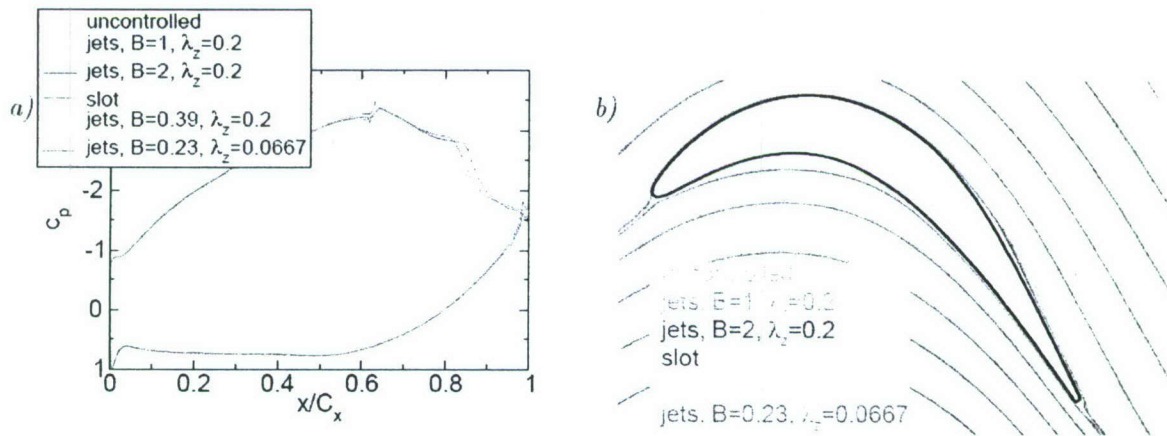


**Fig. 28:** a) Wall pressure coefficient and b) Iso-contours of streamfunction.

When compared with the uncontrolled flow, flow control results in a significant reduction of the mean separation (Fig. 28) and a larger suction near 60% chord combined with a stronger pressure recovery near the trailing edge starting around 80% chord. Harmonic forcing through a slot results in a more effective separation control than control by pulsed VGJs. Disregarding the concomitant increase in energy expense, control with pulsed VGJs is slightly more effective for  $B = 2$  than for  $B = 1$ . The  $B = 0.39$  and  $B = 0.23$  cases are discussed later.

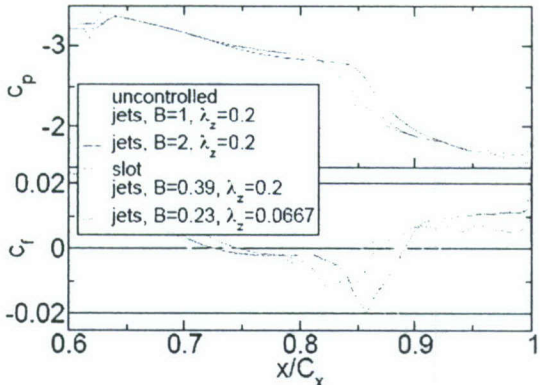


**Fig. 29: Wall pressure coefficient,  $c_p$ , and skin friction coefficient,  $c_f$ .**

A comparison of the wall pressure and skin friction distribution is shown in Fig. 29. The uncontrolled flow separates near 70% chord and does not reattach. The separated flow region can be associated with a "pressure plateau". The skin friction in the upstream part of the bubble is very low. This stagnant or "dead air" region can be associated with the laminar separated boundary layer. A secondary separation can be seen near 90% chord. This secondary separation (in the time mean) can be associated with the strong 2D spanwise coherent structures. Downstream of 90% a strong increase in  $c_f$  can be seen which must be associated with the spanwise structures and the onset of turbulent motion. This region can be associated with the end of the constant pressure region and a rapid pressure increase. Investigations of a generic separation bubble on a flat plate in a wind tunnel for a chord Reynolds number of 100,000 that were carried out by Sohn et al. (1998) showed similar results. The viscous shear stress in the laminar upstream part of the bubble (so-called "dead-air" region) was found to be very small. Downstream of the maximum bubble height discrete spanwise vortices were found to develop due to the K-H instability. This lead to a sharp increase in negative  $c_f$  and the rapid closing of the bubble. The shortest bubble is obtained with the slot forcing. The bubble length is also significantly reduced when the flow is forced with pulsed VGJs. Here, forcing with  $B=2$  results in a slightly shorter bubble than forcing with  $B=1$ .

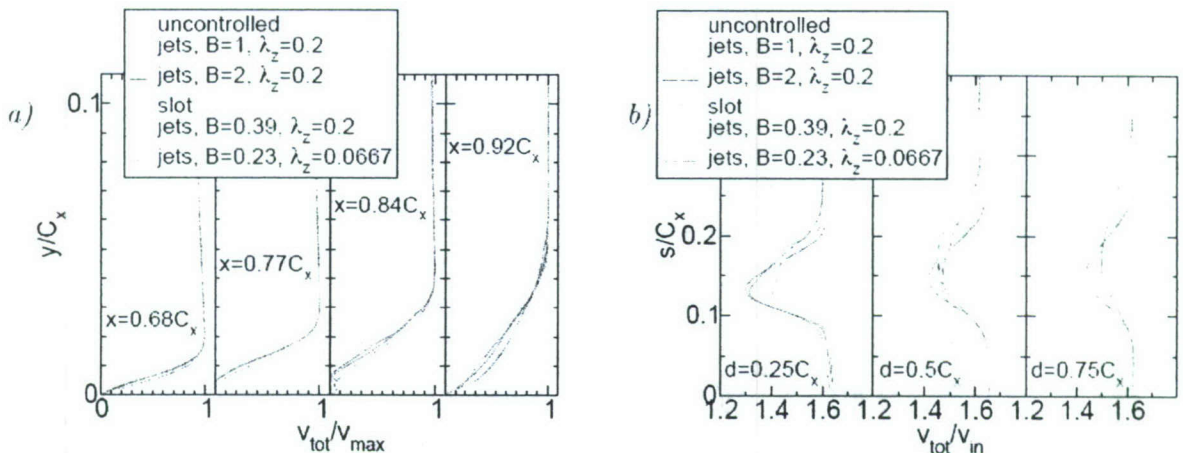


**Fig. 30:** a) Wall-normal profiles and b) wake velocity profiles (distance to trailing edge,  $d$ , is measured in downstream direction, which is at  $30^\circ$  angle to cascade plane; profiles taken perpendicular to out flow direction).

Wall-normal velocity profiles on the blade (normalized by the respective velocity maxima) and wake profiles (averaged in  $t$  and  $z$ ) are shown in Fig. 30. With flow control, a weak reverse flow can be detected at  $s = 0.84C_x$ . Fully attached flow is obtained at  $s = 0.92C_x$ . The fullest velocity profile at  $s = 0.92C_x$  is obtained for the slot. The fuller the profile the more resistant the flow is to separating from the wall. The profile is fuller for the slot forcing because the laminar spanwise vortices entrain more freestream fluid compared to the smaller scale more random structures seen for the case with flow control by pulsed VGJs. Flow control also results in a reduction of the wake width and momentum deficit. Turbulent wake profiles are obtained for the cases with VGJ control.

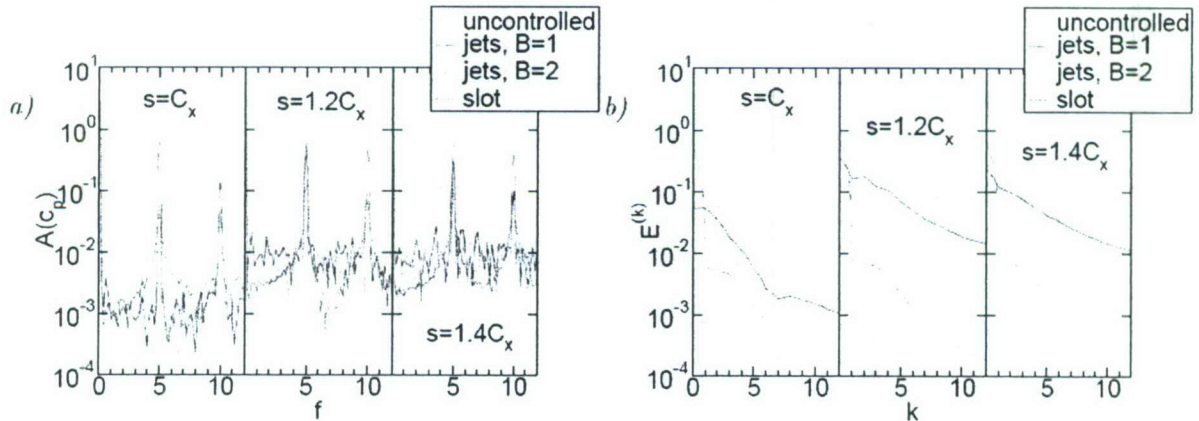


**Fig. 31:** a) Frequency spectra of mode  $k = 0$  of wall pressure coefficient,  $cp$ . b) Modal “energy contents”.

Frequency spectra of mode  $k = 0$  of the wall pressure coefficient in Fig. 31a show pronounced peaks near the forcing frequency and its higher harmonics. At all 3 streamwise stations the highest

peak amplitudes are obtained for the slot forcing. At  $s = 1.2C_x$  and  $s = 1.4C_x$  the peak amplitudes for  $B = 1$  are higher than for  $B = 2$ . Further insight is obtained when considering the modal "energy content", Fig. 31b. At  $s = C_x$  significant 3D mode ( $k > 0$ ) amplitudes are obtained only with pulsed VGJs where the energy contents of the 3D modes is generally higher for  $B = 2$ . Both, the uncontrolled and the controlled case with slot are essentially 2D. At  $s = 1.2C_x$  and  $s = 1.4C_x$  the case with slot forcing remains 2D and the 3D mode amplitudes are noticeably lower than for the uncontrolled flow. With pulsed VGJs at  $s = 1.2C_x$  more energy is contained in the 3D modes than for the uncontrolled flow indicating earlier transition. At  $s = 1.4C_x$  spectra for the cases with VGJ control approximately coincide with the spectrum for the uncontrolled flow. At both,  $s = 1.2C_x$  and  $s = 1.4C_x$ , the energy contents of the 2D mode ( $k = 0$ ) is lower for  $B = 2$  when compared to  $B = 1$  which coincides with the weaker coherence of the spanwise structures in the flow visualizations, Fig. 27.

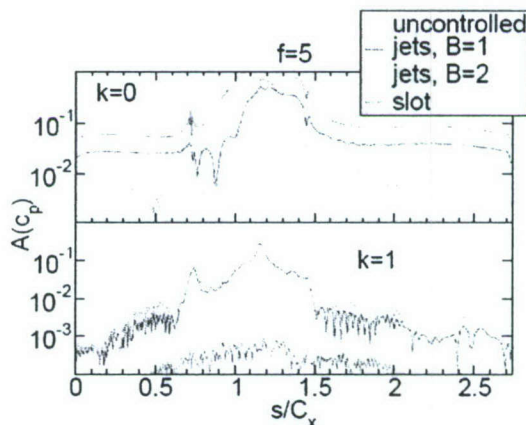


**Fig. 32: Amplitude of  $f = 5$  disturbance component of spanwise modes  $k = 0$  and  $1$  of wall pressure coefficient.**

Finally, amplitude distributions of the  $f = 5$  and  $k = 0, 1$  disturbances of the wall pressure coefficient are shown in Fig. 32. For control with harmonic blowing through a slot the  $k = 0$  mode experiences linear amplification beginning roughly at  $s = 0.8C_x$ . Around  $s = C_x$  saturation is reached. The linear (exponential) amplification in combination with the two-dimensionality of the flow (the 3D modes remain essentially zero) explain the superior efficacy of this flow control compared with the control by pulsed VGJs. With pulsed VGJs linear growth of the 2D mode is also observed, starting, however, later and from a lower amplitude level and reaching saturation farther downstream compared to the case with slot forcing. The harmonic slot forcing is a far more effective way of introducing a 2D disturbance than the pulsed VGJs where the 2D disturbance component is introduced by the in-phase actuation of the VGJs.

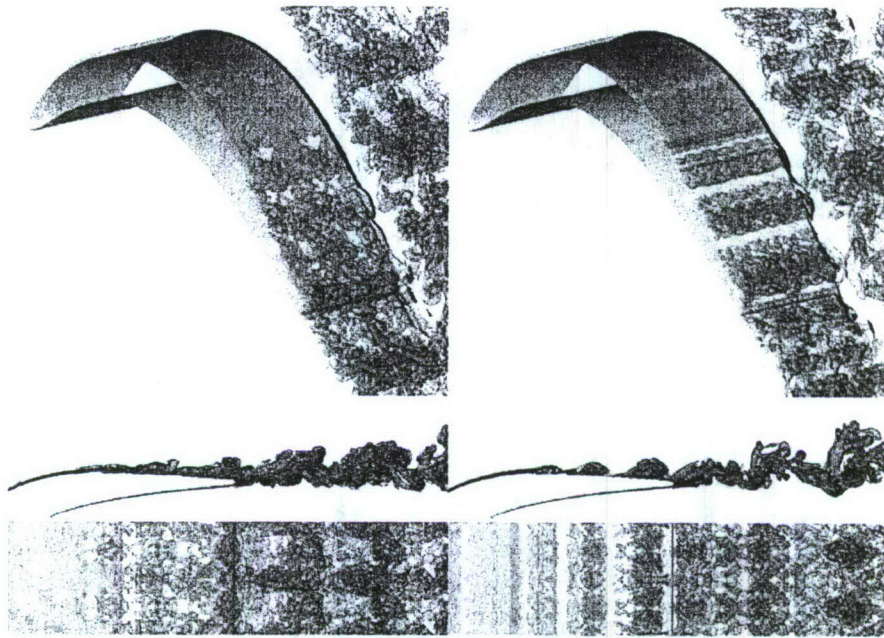


**Fig. 33: Iso-surfaces of vortex identification criterion,  $Q = 1$ , and iso-contours of spanwise vorticity,  $\omega_z$ . Jets with wall-normal harmonic blowing and left:  $B = 0.390$ ,  $\lambda_z/C_x = 0.2$  and left:  $B = 0.225$ ,  $\lambda_z/C_x = 0.0667$ . From top to bottom: Perspective view of blade (computational domain was repeated once in spanwise direction), side view of wake, and top down view of wake.**

Finally we carried out a simulation where we investigated harmonic wall-normal blowing through the VGJ holes, where the momentum coefficient is computed as  $c_p = \frac{1}{4} \pi R^2 / (C_x \Delta Z) B^2$  (where the hole area is taken as  $\pi r_{ab}^2$  because the jets are issued in wall-normal direction). We investigated VGJs with a spanwise spacing of  $\lambda_z=0.2$  and  $B = 0.390$  and VGJs with a spanwise spacing of  $\lambda_z=0.0667$  and  $B = 0.225$ . In both cases,  $B$  was chosen such that the momentum coefficient was equal 2 times the momentum coefficient of the case with harmonic slot forcing. Results are shown in Fig. 33. As the number of holes in the spanwise direction is increased the 2-D component of the actuation becomes larger and the spanwise coherent structures that are shed are seen to become more coherent. When also considering Figs. 28, 29 & 30, it is seen that as the number of holes the "slot" case is approached. Since harmonic blowing through a slot was found to be most effective the lesson learned here is that for low-Reynolds number LPT applications more and more narrowly spaced VGJ holes will likely make the flow control more effective.

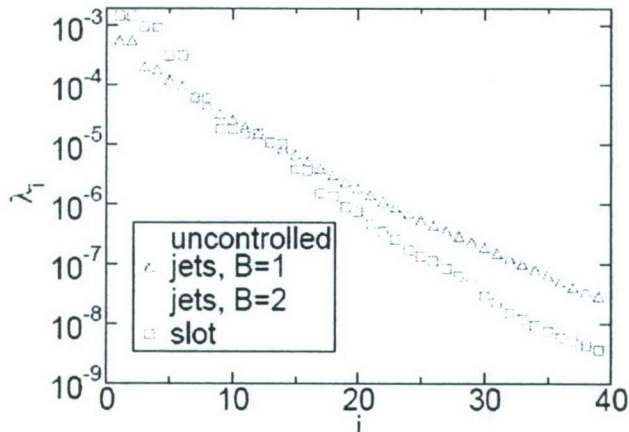


*Fig. 34: Eigenvalues of POD modes (mode energy content).*

Using the snapshot method (Sirovich 1987) we performed a proper orthogonal decomposition (POD) of the time-dependent data. We analyzed 40 instantaneous velocity fields (for the entire computational domain) taken at constant intervals in time. For the uncontrolled flow we considered a time-interval of 1 (corresponding to the period of the dominant frequency signal, Fig. 9); for the controlled flow we considered time-intervals of 0.2 (corresponding to the period of the forcing). Figure 34 shows the POD eigenvalue spectra. The eigenvalue magnitude is identical to twice the kinetic energy content of the corresponding mode. The two most energetic unsteady POD modes,  $i = 1$  and  $2$ , are shown in Fig. 35. These modes appear in pairs indicating that they are related to waves that are traveling in downstream direction. With flow control the time-dependent flow can be captured with less POD modes, indicating that the flow is more "regular": the drop-off in mode energy content towards the higher POD modes is more pronounced than for the uncontrolled flow. This is especially true for the case where the flow is controlled by harmonic blowing through a slot. The main difference between the POD eigenvalue spectra for the cases with pulsed VGJ flow control is the higher energy content for modes 1 and 2 for  $B = 1$ . These modes correspond to spanwise coherent structures that result from the in-phase actuation (in spanwise direction) of the VGJ actuators which introduces a 2D disturbance into the flow that is amplified by the shear layer instability (Fig. 32). When compared with the results for  $B = 1$ , for  $B = 2$  the 2D structures (also referred to as "spanwise rollers") appear weakened (Fig. 27).

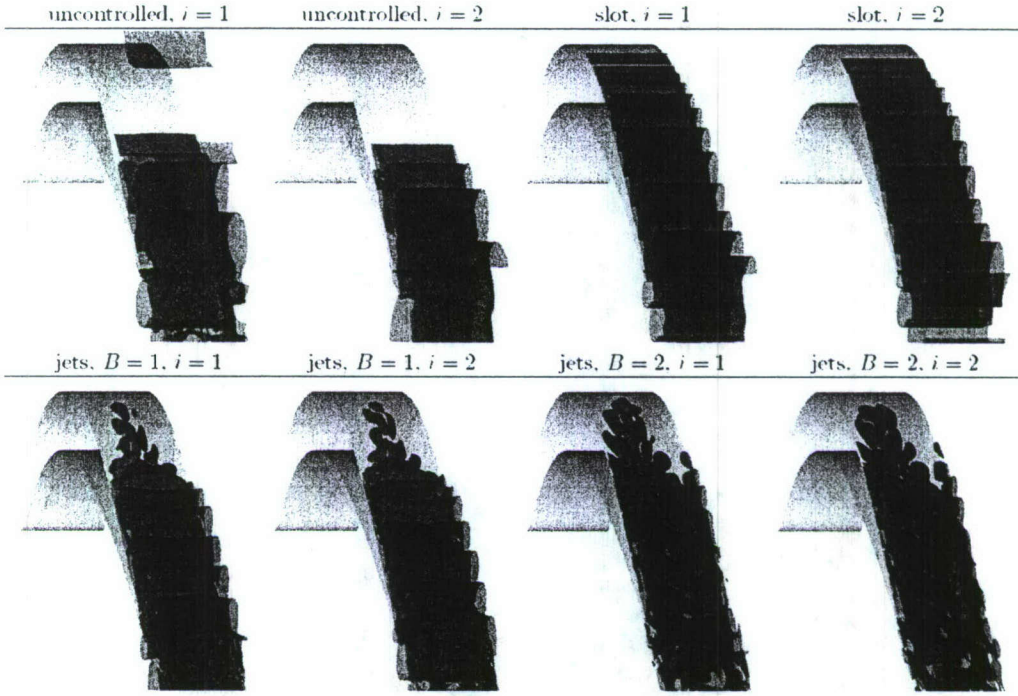


*Fig. 35: POD modes  $i = 1$  and  $i = 2$ . Iso-surfaces of  $q_2 = -0.02$  (blue) and  $q_2 = 0.02$  (red).*

The POD mode time signals are shown in Fig. 36. When considering the uncontrolled flow, the oscillation period of modes 1 and 2 can hardly be determined from the time-signals which appear rather random which is an indication of transitioning and turbulent flows. One has to resort to the frequency spectra obtained from the Fourier transforms of data taken over the significantly longer time interval of 20 (Fig. 11) to estimate a period of roughly 1 for the dominant modes which constitute spanwise vortical structures (also referred to as "spanwise rollers", Fig. 35). These structures can also be discerned when scrutinizing instantaneous visualizations of the time-dependent data (Fig. 7). As these structures were not artificially introduced into the flow they are likely the result of an instability mechanism of the flow (such as a shear layer instability).

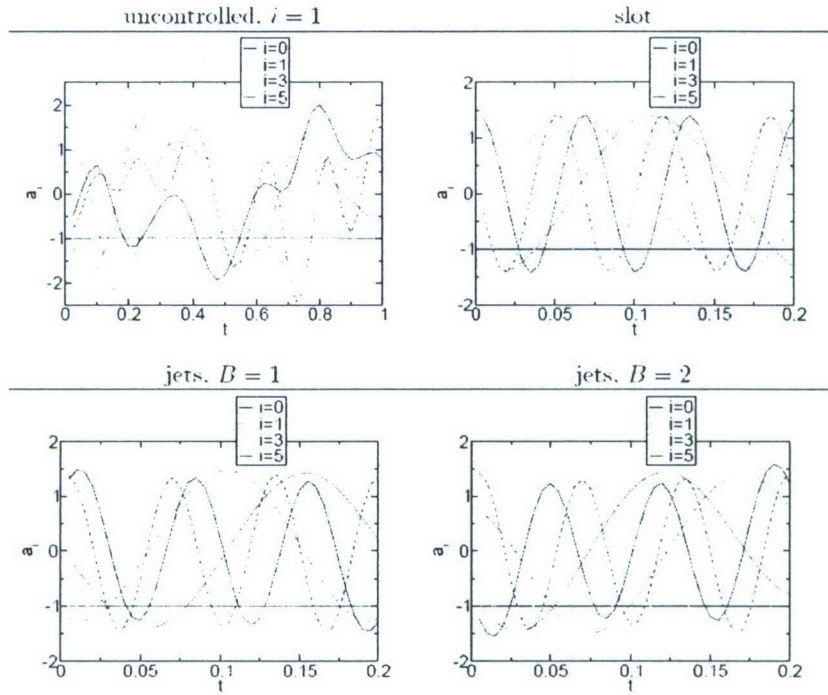


**Fig. 36: POD mode time-signals,  $a_i$ .**

With pulsed VGJs for  $B = 1$  the dominant structures are also spanwise coherent structures (Figs. 27 & 35). The period of the corresponding mode 1 and 2 time-signals is 0.2 (Fig. 24) which leads to the conclusion that the spanwise structures are a direct consequence of the actuation. When resorting to Fig. 32 it can be seen that disturbances with  $f = 5$  (which can be associated with the POD modes 1 and 2) are amplified by the flow by roughly two orders of magnitude. One may argue that for  $B = 1$  the dominant flow control mechanism appears to be the additional wall-normal mixing facilitated by these spanwise coherent structures which are introduced by the in-phase actuation of the pulsed VGJs and which are amplified by the flow ("at no cost"). When the VGJ amplitude is increased to  $B = 2$  the time signals of the dominant POD modes are equally linked to the actuation (the mode 1 & 2 periods are 0.2, Fig. 24). However, compared to  $B = 1$  the dominant structures are no longer spanwise structures but oblique structures (Figs. 27 & 35). Also, compared to the  $B = 1$  case less energy is contained in modes 1 and 2 (Fig. 34). The difference in the control effectiveness which can be determined from the wall pressure distribution (Fig. 28) or wake velocity profiles (Fig. 30) is marginal.

Finally, for pulsed actuation through a slot, modes 1 & 2 up to 15 & 16 (fundamental and higher harmonics) appear in pairs of equal eigenvalue magnitude (Fig. 34) where the mode shape (Fig.

35) and time-coefficients (Fig. 36) belonging to each pair are similar but shifted (in streamwise direction and time, respectively) by a quarter wavelength. Again, the mode 1 and 2 time-signal is directly related to the actuation. When also considering the Fourier mode amplitudes (Fig. 32) it can be seen that the disturbances (mode  $k = 0, f = 5$ ) which are introduced by the actuation are strongly amplified in downstream direction. An effective control is established for very small disturbance inputs and thus at "little cost". Was it not for the harsh turbine operating environment and related doubts about life time limitations and maintenance issues plasma actuators would certainly be a good choice for introducing such disturbances. When also considering the instantaneous flow visualizations (Fig. 27) it appears that transition is delayed. The concept of transition delay at low Reynolds number conditions by spanwise vortices was first investigated by Embacher and Fasel (2007). It was shown that for a certain frequency range of the spanwise coherent structures the growth rates of secondary instabilities could be reduced resulting in a transition delay and (this was shown in a full DNS) relaminarization of an already turbulent flow. This is advantageous as it was found that laminar spanwise vortices facilitate a stronger wall-normal momentum exchange than the small scale structures associated with a turbulent boundary layer resulting in fuller velocity profiles (Fig. 30a) and a more effective separation control.

Since the forcing of spanwise coherent structures was found to delay transition and prevent separation while requiring only a very low energy input we decided to investigate if similar effects could be obtained by introducing streamwise vortices of sufficient strength into the flow. From the onset of this investigation it was clear that the flow, because of the convex curvature on the suction side and despite the slight streamwise excess velocity near the wall, would likely not support or amplify streamwise vortices and that, therefore, large forcing amplitudes would be required to generate streamwise vortices of considerable strength. This was, however, perceived to be of little concern as streamwise structures can be generated by passive means such as vortex generators (VGs) which require no external power. For VGs the maximum disturbance amplitude input is limited by concerns such as flow separation near the device. Using volume forces we forced streamwise vortices with spanwise wavelengths of  $\lambda_z = C_x = 0.05, 0.0667, 0.1$ , and  $0.2$  and non-dimensional volume forcing amplitudes of  $A = 1$  and  $10$ . With the current grid resolution of 32 cells in  $z$  the lower resolution limit of 8 cells per wavelength is reached for  $\lambda_z = 0.05$ . At this resolution, reasonably accurate results can still be expected with the ninth-order-accurate scheme employed for the current investigations. All simulations were initialized with the uncontrolled flow.

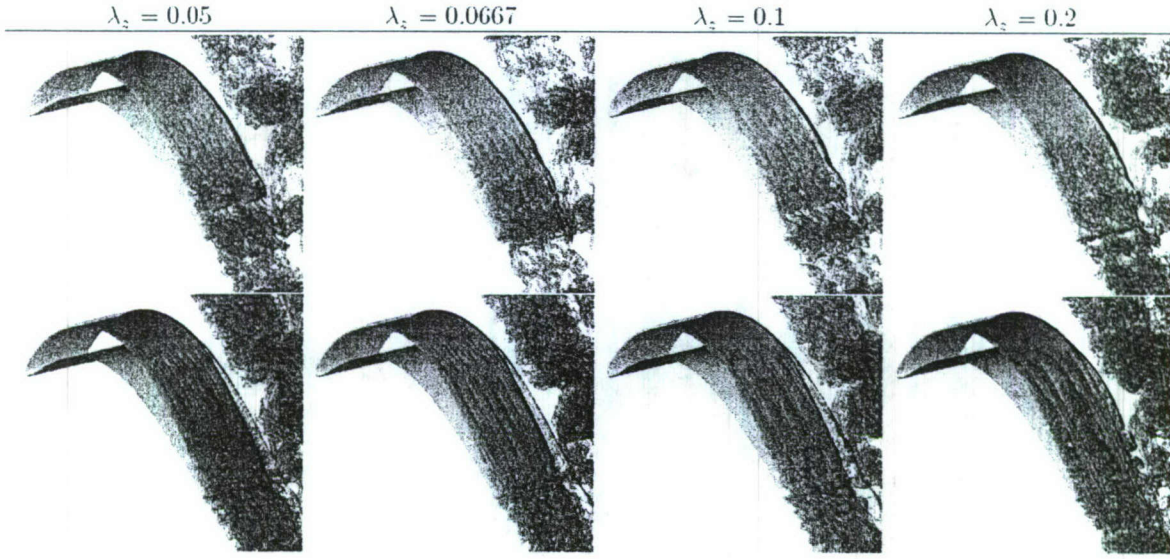


**Fig. 37:** Streamwise vortices with spanwise wavelength,  $\lambda_z$ , and amplitude  $A = 1$  (top) and  $A = 10$  (bottom) forced for  $0.61 < x < 0.71$ . Iso-surfaces of vortex identification criterion,  $Q = 1$ , and iso-contours of spanwise vorticity,  $\omega_z$ , at  $z = 0$ .

Instantaneous visualizations of the flow are shown in Fig. 37. For  $A = 10$  and  $\lambda_z = 0.05$ ;  $0.0667$  flow transition appears delayed compared to the uncontrolled flow (Fig. 7) and high frequency short wavelength spanwise structures are seen to develop on top of the streamwise vortices. These structures are too far away from the wall to imprint a pressure signal on the wall that was large enough to be detected over the background noise. When the wavelength is increased to  $\lambda_z = 0.1$  spanwise coherent structures appear near the trailing edge. For  $\lambda_z = 0.2$  regions of turbulent flow develop in between the streamwise vortices. Clearly, there seems to be an optimal spanwise wavelength for delaying/suppressing transition with streamwise vortices.

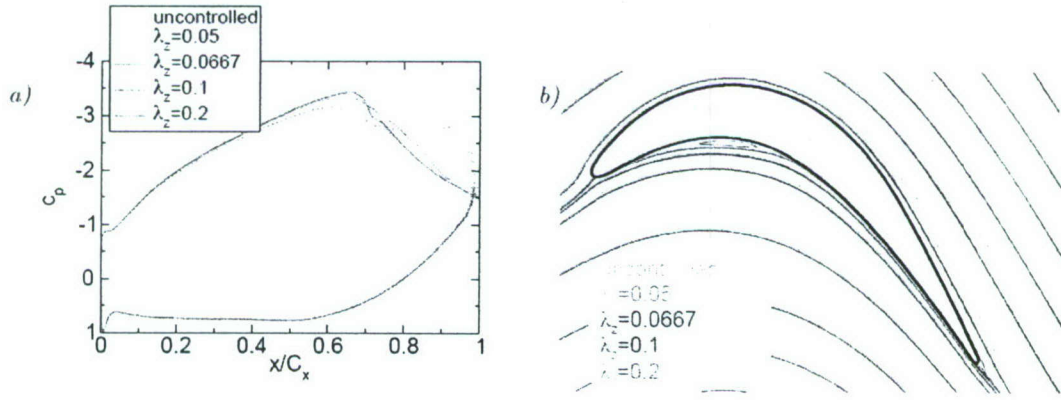


**Fig. 38:** a) Wall pressure coefficient (dotted lines:  $A = 1$  and solid lines:  $A = 10$ ) and b) Iso-contours of streamfunction for  $A = 10$ .

A comparison of the computed wall pressure distributions is given in Fig. 38a. For  $A = 1$  the effect of the streamwise vortices on the flow is minimal and the computed pressure distributions follow the pressure distribution of the uncontrolled flow. A complete suppression of flow separation is accomplished for  $A = 10$  and  $\lambda_z = 0.05$  and  $0.0667$ . For  $\lambda_z = 0.1$  the  $c_p$ -distribution is flat near the trailing edge indicating flow separation. For  $\lambda_z = C_x = 0.2$  a slightly higher  $c_p$  is obtained near 65% chord and the  $c_p$ -distribution in the pressure recovery region does not follow the curves for  $\lambda_z = 0.05$  and  $0.0667$  indicating a less effective control. Iso-contours of the streamfunction (averaged in  $t$  and  $z$ , Fig. 38b) also indicate fully attached flow for  $A = 10$ .

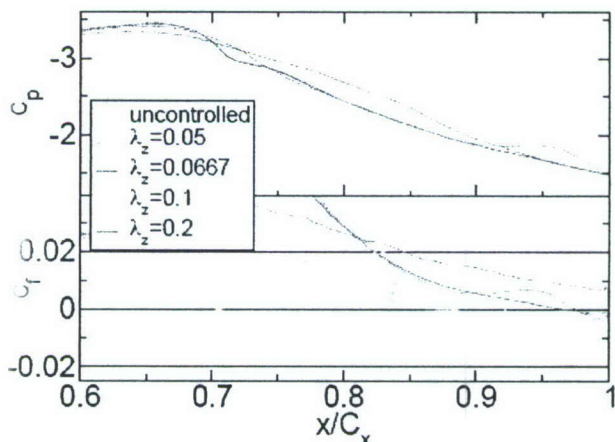


**Fig. 39: Wall pressure coefficient,  $c_p$ , and skin friction coefficient,  $c_f$  ( $A = 10$ ).**

A comparison of the wall pressure and skin friction distribution for  $A = 10$  is shown in Fig. 39. Separation is completely eliminated for  $\lambda_z = 0.05$  and  $\lambda_z = 0.2$ . The appearance of spanwise coherent structures near the trailing edge for  $\lambda_z = 0.1$  can be associated with a small "pressure plateau" and a skin friction increase.

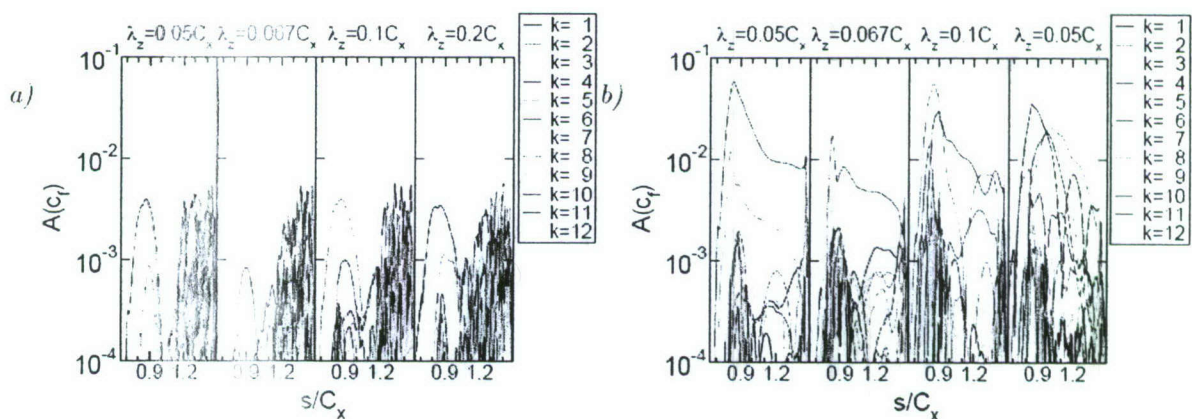


**Fig. 40: Fourier transforms of skin friction coefficient,  $c_f$ . Amplitudes of spanwise modes with mode number  $k$  of time-averaged solution ( $n = 0$ ). a)  $A = 1$  and b)  $A = 10$ .**

Amplitude distributions of the spanwise modes  $k = 1 \dots 12$  of the time-averaged ( $n = 0$ ) wall skin friction coefficient,  $c_f$ , are compared in Fig. 40. The initial amplitudes near  $s = 0.9$  (the streamwise vortices are forced between  $x = 0.61 \dots 0.71$  which corresponds to  $s = 0.83 \dots 0.93$ ) are about the same in all three instances and one order of magnitude larger for  $A = 10$  compared to  $A = 1$ . For  $A = 1$  the amplitude of the fundamental (the dominant disturbance wavelength introduced by the forcing) decays quickly and has little effect on the other modes. For  $A = 10$  the amplitude of the fundamental is still seen to decay independent of the spanwise wavelength. This is not surprising as the boundary layer is convex and, hence, not Görtler-unstable. However, the decay rate near  $s = 1.2$  is the smallest for  $k = 4$  ( $\lambda_z = 0.05$ ). If the goal was to delay or prevent separation by streamwise vortices then, out of the 3 wavelengths studied,  $\lambda_z = 0.05$  would be the preferred spanwise wavelength.

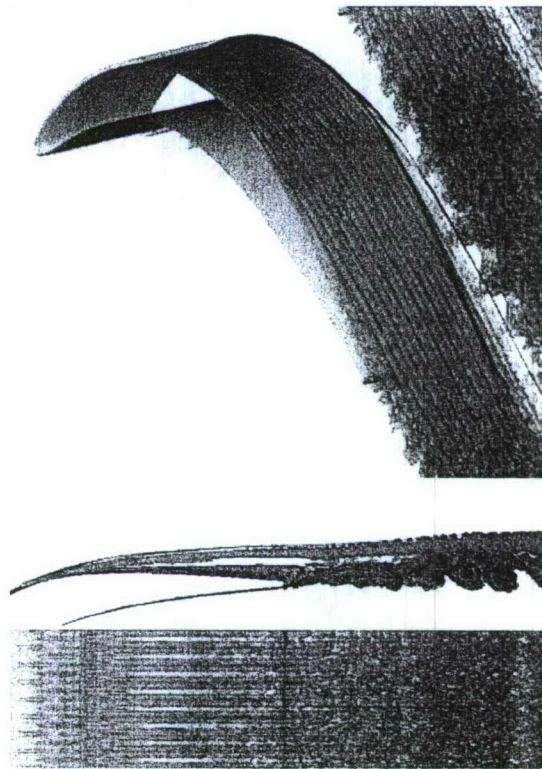


**Fig. 41: Fine grid solution. Streamwise vortices with spanwise wavelength,  $\lambda_z = 0.05$ , and amplitude  $A = 10$  forced for  $0.61 < x < 0.71$ . Iso-surfaces of vortex identification criterion,  $Q = 1$ , and iso-contours of spanwise vorticity,  $\omega_z$ , at  $z = 0$ . From top to bottom: Perspective view of blade (computational domain was repeated once in spanwise direction), side view of wake, and top down view of wake.**

For verification, we repeated the  $\lambda_z = 0.05$  and  $A = 10$  simulation for the fine grid. An instantaneous flow visualization is shown in Fig. 41. The flow looks qualitatively very similar to the result obtained with the medium resolution grid (Fig. 37 bottom left). On the fine grid the formation of the high frequency spanwise structures that are situated on top of the streamwise structures is delayed. Wall pressure coefficient distributions as well as iso-contourlines of the streamfunction (both quantities were averaged in  $t$  and  $z$ ) for the medium and the fine grid are shown in Fig. 42a. The pressure distribution for the fine grid is leveling off near the trailing edge indicating incipient flow separation. Iso-contourlines of the streamfunction also indicate a slight thickening of the suction side boundary layer near the trailing edge (Fig. 42b). But overall the agreement between the medium and the fine grid solution is very good.

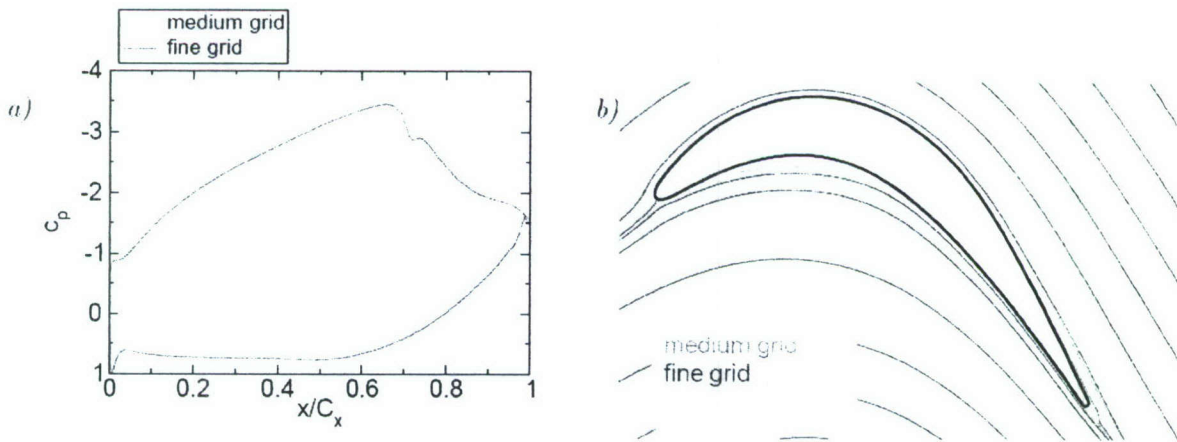


**Fig. 42: a) Wall pressure coefficient and b) iso-contours of streamfunction for  $\lambda_z = 0.05$  and  $A = 10$ .**

### 2.5.3 3-D Simulations for L1M Geometry

Following numerous LPT experiments (Bons et al. 2005, Reimann et al. 2006) we decided to also investigate AFC by pulsed VGJs for the L1M geometry using 3-D FSM (Gross2007b). The jet exit holes were positioned at  $x=0.56C_x$  and had a  $30^\circ$  pitch and  $90^\circ$  skew angle (same as in the experiments). The hole spacing was identical to the spanwise extent of the computational domain,  $\Delta z=0.2C_x$ . Each hole was resolved by  $7\times 7$  cells and had a diameter of  $d=0.0388C_x$ . At this resolution the near-hole fluid dynamics are only minimally resolved. Forcing frequency, duty cycle, and blowing ratio were  $f=7$ ,  $\tau=10\%$ , and  $B=4$ , respectively. The momentum coefficient was  $c_\mu=0.00473$ . In addition, the flow was also controlled by harmonic blowing through a slot with  $f=7$  and  $B=0.1$ . The slot was located at  $x=0.55C_x$ , had a width of  $b=0.015C_x$ , and was resolved by 3 cells. The momentum coefficient was  $c_\mu=0.0000563$ .

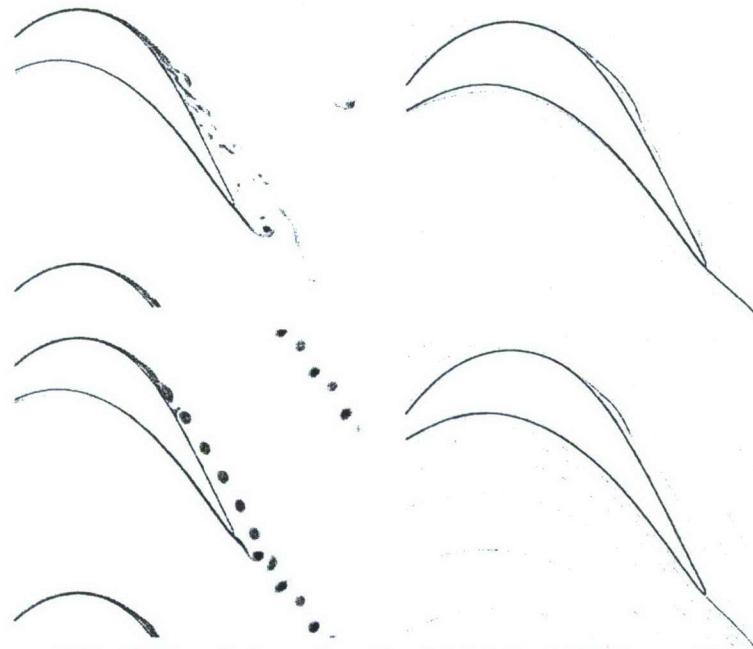


**Fig. 43:** Spanwise vorticity (left) and streamfunction (right) for L1M. Control by pulsed VGJs (top) and harmonic blowing and suction through slot (bottom).

A comparison of both controlled cases (Fig. 43) with the uncontrolled flow (Fig. 14) shows that both flow control strategies effectively reduce the size of the separated flow region. When considering the spanwise vorticity it appears that the flow control by pulsed VGJs results in an earlier transitioning of the flow. The attached turbulent boundary layer can withstand a larger adverse pressure gradient. In the contrary, control by harmonic forcing through a slot appears to weaken the amplification of 3-D structures. In this case, the flow can be seen to regularize, it becomes almost perfectly 2-D and time-periodic. The resulting strong spanwise 2-D structures appear to further decrease the size of the separation bubble (due to mixing provided by the spanwise highly coherent structures) when compared with the PVGJ control.

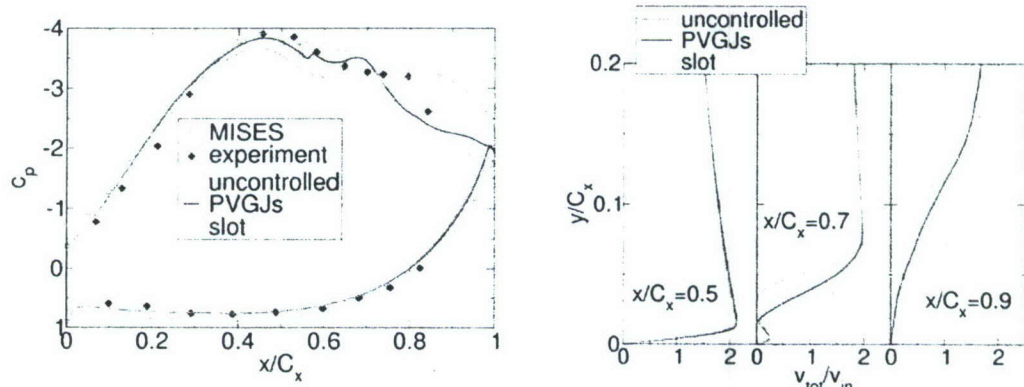


**Fig. 44:** Wall pressure coefficient (left) and wall normal velocity profiles (right) for L1M.

The wall pressure coefficient as computed from the temporal and spanwise average of the data and the attached flow pressure distribution obtained from a design code (MISES) (Reimann et al. 2006) are shown in Fig. 44. Both control schemes delay flow separation and thereby increase the length of the favorable pressure gradient region. The earlier suction side reattachment leads to a stronger pressure recovery in the aft part of the blade. Slightly upstream of the separation location, at  $x/C_x=0.5$ , the computed velocity profiles are almost identical. At  $x/C_x=0.7$ , all profiles indicate separated flow even for the cases with flow control. At  $x/C_x=0.9$  attached flow profiles are obtained for the cases with flow control. A larger wall shear and smaller displacement thickness is obtained for the case with harmonic blowing through a slot, indicating stronger wall normal momentum exchange (due to the spanwise coherent structures) than for the control by pulsed VGJs (which result in turbulent mixing).

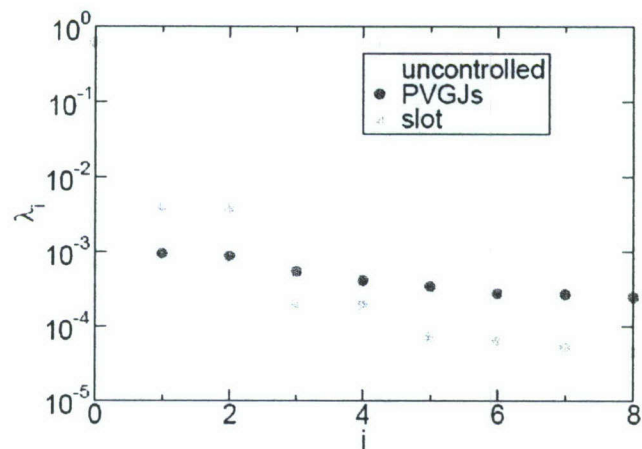
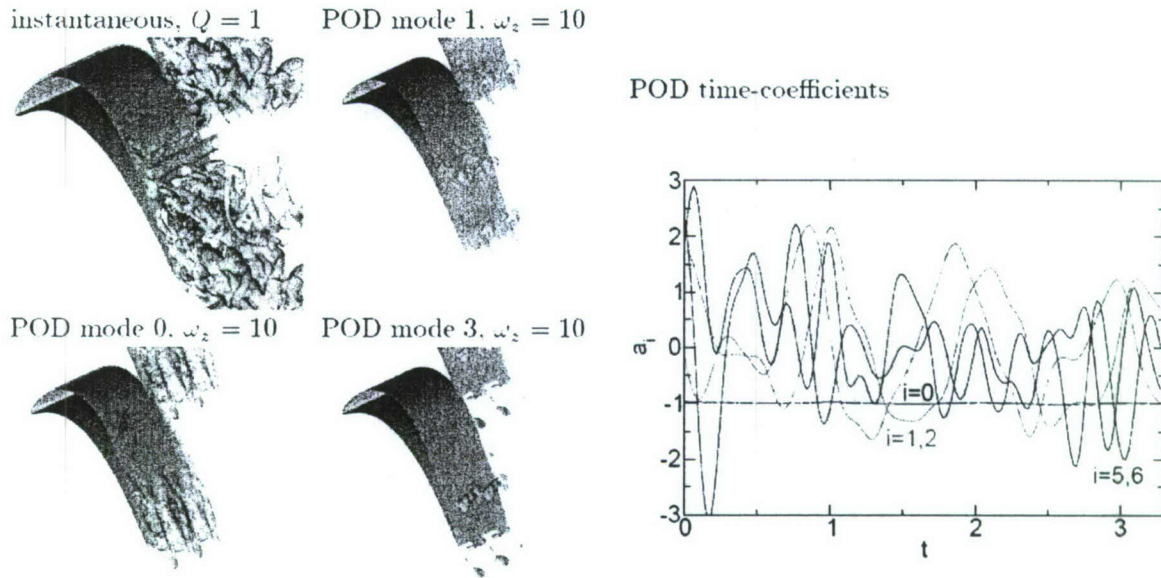
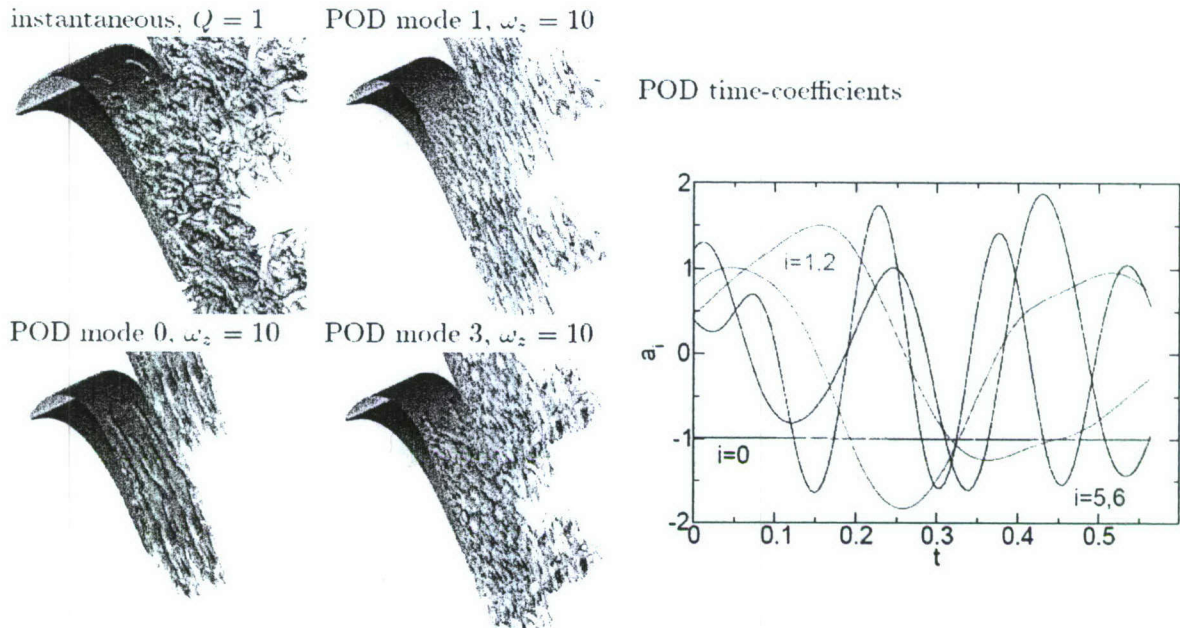


Fig. 45: POD eigenvalues for L1M.



*Fig. 46: Uncontrolled flow. POD eigenfunctions and time-coefficients for L1M.*

A proper orthogonal decomposition (POD) of the time dependent 3-D flow data was performed to gain more insight into the relevant flow dynamics. For the uncontrolled case, 165 snapshots over a time interval of  $\Delta t = 3.28$  were analyzed. The computed POD eigenvalues are shown in Fig. 45 while the POD modes and time-coefficients are shown in Fig. 46. For comparison, an instantaneous visualization of the flow was also included in Fig. 46. The dynamics of the uncontrolled flow can be seen to be somewhat chaotic and random. This was expected as no controlled time-periodic disturbances were introduced into the flow. The oscillation period of modes 1 and 2 is roughly 1. The mode shapes (mode 2 not shown) and time coefficients are phase shifted by  $90^\circ$  and the corresponding eigenvalues are of similar magnitude, indicating a similar energy contents (Fig. 45). The mode shapes reveal that this mode couple is related to the spanwise coherent structures (2-D vortices) of the initial shear layer roll-up. Modes 3 and 4 can also be associated with traveling spanwise coherent structures. They have an oscillation period of about 0.33 and are possibly non-linearly generated higher harmonics of the 1, 2 mode couple. The corresponding structures are situated within the transitional flow region, indicating that energetic spanwise coherent structures may survive in the turbulent flow. The drop-off in mode energy towards the higher modes is small as is typical for transitional and turbulent flows (Fig. 45). A large number of POD modes would be required for accurately capturing the dynamics of the flow.



**Fig. 47: Control with pulsed VGJs. POD eigenfunctions and time-coefficients for L1M.**

Results for the case with PVGJ control are shown in Figs. 45 and 47. For this analysis 114 snapshots over a time interval of  $\Delta t = 0.565$  (which corresponds to 4 time periods of the actuation) were analyzed. The instantaneous flow visualization which is included in Fig. 47 indicates that the flow is transitioning some distance downstream of the VGJ holes. The flow displays very little coherence and the drop-off in energy towards the higher modes is very low (Fig. 12). A comparison with the uncontrolled flow reveals a reduced energy content of the unsteady modes and a larger energy contents for mode 0. While the oscillation periods of modes 5 and 6 are almost identical to the forcing period, the oscillation periods of the more energetic mode couples 1 and 2 as well as 3 and 4 are considerably larger. When resorting to Fig. 47 it becomes apparent that the oscillation periods of these modes may be related to the dynamics of the spanwise coherent structures in the wake region. In general, the POD results will depend on the flow region that is being analyzed. For the present results it was decided to analyze flow data from blocks 3 and 4 (the O-topology block around the blade and the H-topology block in the wake region) only.

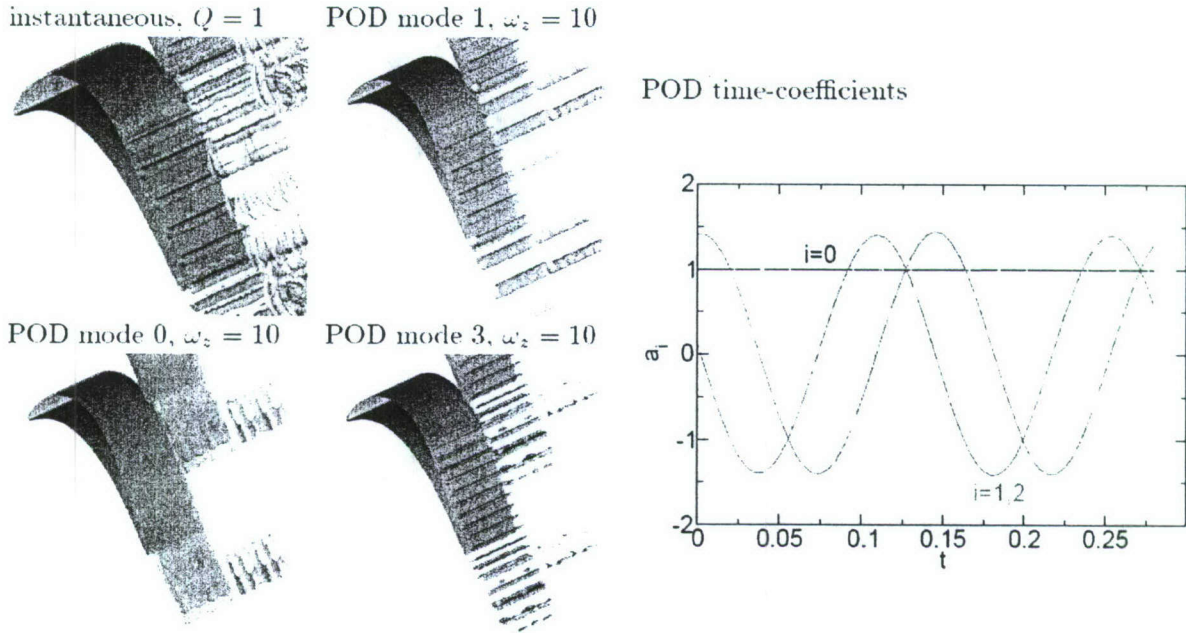


**Fig. 48: Control with harmonic blowing through slot. POD eigenfunctions and time-coefficients for L1M.**

Finally, POD results for the controlled case where the disturbances were introduced by harmonic blowing through a spanwise slot are shown in Figs. 45 and 48. For this analysis 57 snapshots over a time interval of  $\Delta t = 0.28$  (which corresponds to two time periods of the actuation) were analyzed. Compared with the uncontrolled case the energy contents of modes 1 and 2 is noticeably increased (Fig. 45). Modes 1 and 2 as well as modes 3 and 4 appear in pairs. Both pairs describe traveling spanwise 2-D structures. The oscillation periods of modes 1 and 2 are identical to the actuation period. These modes are a direct consequence of the harmonic forcing. The corresponding flow structures originate from the forcing slot and experience amplification in the downstream direction. Modes 3 and 4 have a three times larger oscillation frequency and can be interpreted as non-linearly generated higher harmonics of modes 1 and 2. Even in the wake region, the flow remains essentially 2-D over a considerable downstream distance. Starting from the uncontrolled flow the time interval that was needed for the flow to "lock in" to the new 2-D time-periodic state starting from the time instant when the control was activated was about  $\Delta t=7$ .

## 2.6 Closed-Loop Control

We also investigated different closed-loop control schemes for the L1M LPT blade (Brehm et al..2006, Gross and Fasel 2007c). Open-loop investigations show that within a certain frequency

range disturbances are amplified. This can be exploited for making the control more effective. The amplification is attributed to a hydrodynamic instability of the base flow. A simple closed-loop controller, where a downstream pressure signal is fed back to an upstream actuator, can be as effective as an optimized open-loop controller. The simple closed-loop controller can be improved by continuously adjusting the controller parameters during the run time of the simulation using a minimization algorithm that minimizes a desired objective such as drag over lift and control effort. This allows for an optimization of the gain and phase of the feedback resulting in a better "synchronization" or coupling of the actuation and the flow dynamics. We also employed neural networks for making real-time predictions of the unsteady separated flow field. The resulting models are shown to be both accurate and robust and to generalize well.

### 2.6.1 Open-Loop Control Parameter Study for L1M Blade

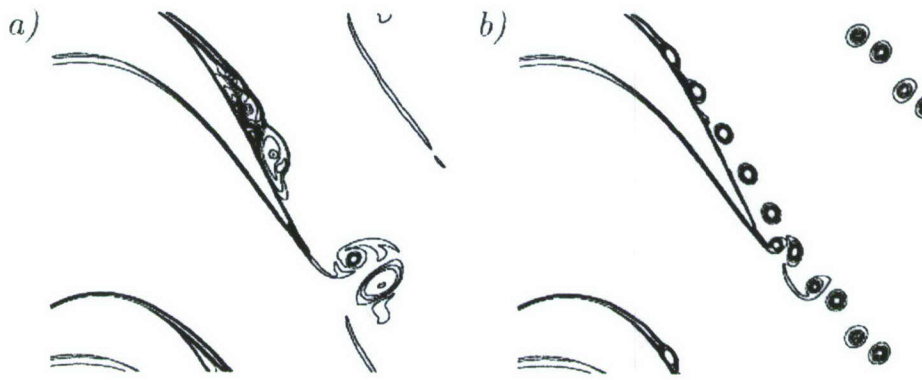


**Fig. 49: Control with harmonic blowing through slot. POD eigenfunctions and time-coefficients for L1M.**

We explored a wide range of forcing parameters was explored in simulations with open-loop flow control for determining the sensitivity of the flow with respect to the forcing frequency and amplitude. Instantaneous visualizations for the uncontrolled "natural" flow and a controlled flow are shown in Fig. 49. The uncontrolled flow is dominated by large vortical structures and features a large separation bubble (in the mean). When the open-loop control is activated the flow quickly "locks in" to the forcing (it becomes more regular) as shown in Fig. 49b and flow separation is reduced. As a result of the reduced separation, the pressure distribution around the blade changes as shown in Fig. 50a. The control also results in a change of the mean aerodynamic coefficients and a reduction of the oscillation amplitudes of the instantaneous aerodynamic coefficients (Fig. 3b). The aerodynamic coefficients,  $c_{x,y}$ , in axial ( $x$ ) and normal to the axial direction ( $y$ ) were

computed by integration of the pressure and friction forces over the entire blade geometry and normalized with the in flow velocity, density, and axial chord length.

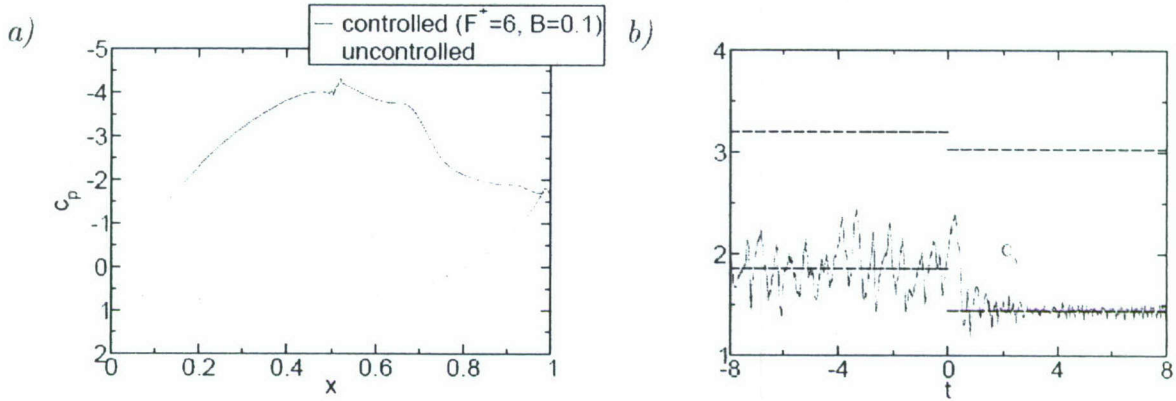


**Fig. 50:** a) Wall pressure coefficient and b) Time-history of normalized aerodynamic forces. Open-loop control with  $F^+ = 6$  and  $B = 0.1$  is activated at  $t = 0$ .

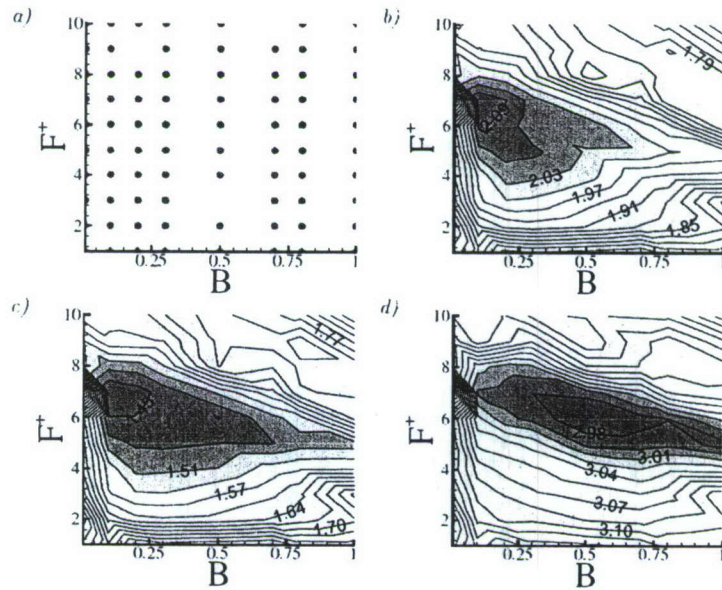


**Fig. 51:** Open-loop control. Exploration of parameter space (blowing ratio,  $B$ , and forcing frequency,  $F^+$ ) for open-loop control. a) Test matrix, b) performance index computed as  $\overline{c_y}/\overline{c_x}$ , and aerodynamics coefficients c)  $c_x$  and d)  $c_y$ .

As a measure for the effectiveness of the control, a performance index,  $\overline{c_y}/\overline{c_x}$ , was used where the overbars indicate time-averages. A simple momentum balance shows that this parameter is a measure for the total flow turning (difference between cascade in flow and outflow angle). Blowing ratios in the range  $B = 0.01 \dots 1$  and forcing frequencies in the range  $f = 1 \dots 10$  were explored in a systematic manner (Fig. 51a). For small blowing amplitudes the forcing is most effective when the

forcing frequency is close to 8 (Fig. 51b). As the blowing ratio is increased the most effective frequency is slightly decreased to 7. A clear maximum of the performance index is located at  $B = 0.1$  and  $f = 7$ . The frequency range for which the flow control is beneficial becomes largest for  $B = 0.1 \dots 0.2$ . As the blowing ratio is increased, the control slowly loses effectiveness. For larger blowing ratios the boundary layer separates from the wall at the blowing slot location. This is counter-productive: Although the control still leads to an earlier reattachment (when compared to the uncontrolled 'natural' case) the flow separates earlier. For high-enough blowing ratios the "mean" jet acts as a flow obstruction. Overall, the distribution of the performance index in Fig. 51b has a wedge shape where the frequency range for which flow control is effective becomes increasingly more narrow and the optimal frequency is reduced as the blowing ratio is increased. The parameter analysis also demonstrates that high performance gains are possible even with a non-optimal open-loop control. The data collected in Fig. 51 could in principle also be used as a look-up table for designing open-loop controllers that pick frequency and blowing ratio such that a certain desired  $c_x$  and  $c_y$  are obtained. When considering the individual aerodynamic forces it becomes clear that the gain in aerodynamic performance is mostly due to a reduction of  $c_x$ . The separation bubble is located near the trailing edge of the blade in the area of uncovered turning where the pressure recovery takes place. In the uncontrolled case, the flow cannot negotiate the adverse pressure gradient and separates, resulting in a pressure distribution that is below the design pressure in the aft part of the blade (Fig. 50a). Due to the curved geometry of the blade, this loss shows up mainly in the  $c_x$ -coefficient. When the control is turned on, separation is reduced, and the pressure at the aft part of the blade is raised.

### 2.6.2 Self-Adaptive Closed-Loop PD Controller

The simulation using a proportional differential (PD) controller (Brehm et al. 2006) was started from the uncontrolled "natural" flow. The initial dramatic reduction of the objective function (Fig. 52a) is a consequence of the initial control parameters already being well suited for an efficient feedback control. While most of the gain in aerodynamic performance,  $c_y=c_x$ , is achieved in the very beginning as the control is activated, the control effort is subsequently gradually lowered without loss in aerodynamic performance (Fig. 52b). The time evolution of the controller parameters is shown in Fig. 52c. The gain coefficients of both, the proportional and the differential part of the controller,  $K_P$  and  $K_D$ , are reduced by more than 50%. This adjustment is going hand in hand with an adjustment of the phase lags,  $n_{IP}$  and  $n_{ID}$ . Sensor and forcing signal are shown in Fig. 52d. The actuator signal is clearly related to the sensor signal. The controller picks a frequency of about 5

and an amplitude of about 0.1. These forcing parameters are close to the optimum values found in the parameter study ( $F^+ = 6, 7$  and  $B = 0.1$ ). The gain in aerodynamic performance,  $c_y/c_x$ , is 21%. This number is slightly lower than the optimal 24% determined earlier. Fig. 52c also shows that the adjustment of the step-size of the parameter changes is not sufficient for making the controller parameters converge. For the PakB blade we employed a gradient descent based method to improve convergence of the method.

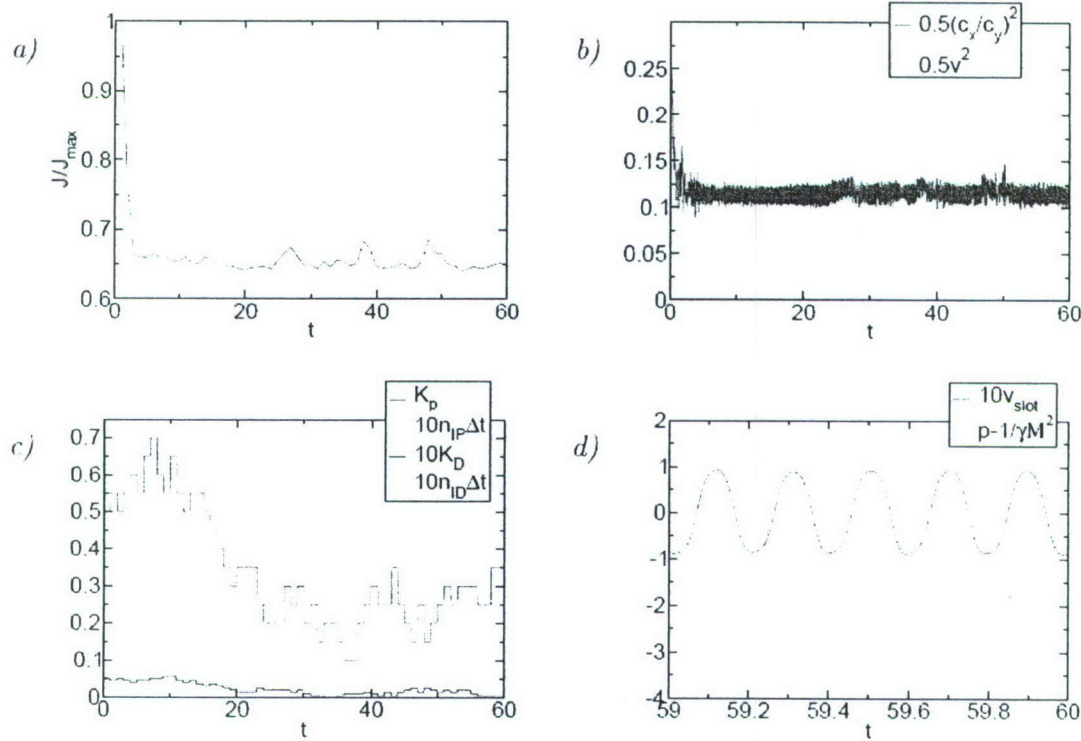


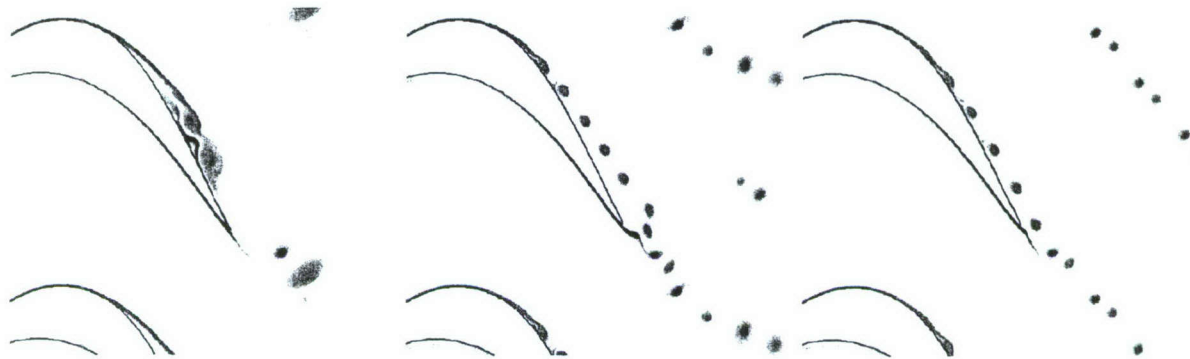
**Fig. 52: Self-adaptive PD controller.** a) Objective normalized with maximum value, b) individual components of objective (inverse of aerodynamic performance,  $1/2(c_x/c_y)^2$ , and control effort,  $1/2v^2$ ), c) controller parameters, and d) sensor and actuator signal.

Instantaneous visualizations of the uncontrolled “natural” flow and the controlled flow are shown in Fig. 53. A similar picture emerges as for the open-loop control (Fig. 49): The closed-loop controlled flow is now also governed by small scale vortices that appear in a very regular fashion but at a larger spacing compared to the open-loop result. The flow “locks in” to the forcing and separation (in the mean) is prevented.

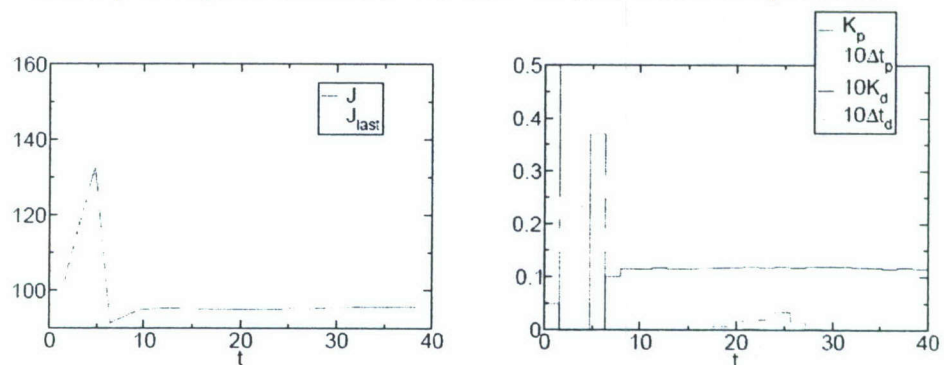


**Fig. 53: Control with harmonic blowing through slot. POD eigenfunctions and time-coefficients for L1M.**

We improved the algorithm by using the simultaneous perturbation stochastic approximation (SPSA, Spall 1992, 1997) for minimizing the objective (Gross and Fasel 2007c). With SPSA all variables are perturbed simultaneously and an approximate gradient is computed. The method requires less function approximations than gradient descent.



**Fig. 54: L1M LPT blade. Iso-contours of spanwise vorticity,  $w_z$ . From left to right: uncontrolled flow, open-loop control with  $f = 7$  and  $B = 0.1$ , and closed-loop control**



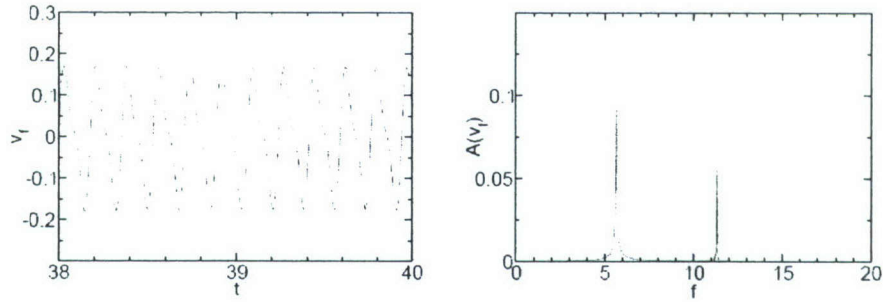


**Fig. 55:** Wall pressure coefficient  $c_p$  at locations  $x = 0.624, 0.681, 0.732$ , and  $0.773$  as obtained from Navier-Stokes simulation with  $F^+ = 7.5$  and  $B = 0.1$  (black lines) and as predicted by neural network (red lines). The neural network was trained for  $F^+ = 5, 6, 7, 8$  and  $B = 0.1$ .

For these simulations, the “sensor” is a pressure tab located at 81% axial chord on the suction side of the blade in the separated flow region. The objective was updated at time intervals of  $\Delta T = 0.8$  (roughly 5 vortex shedding cycles). The closed-loop simulation was started from the uncontrolled “natural” flow. Visual inspection of the instantaneous flow field (Fig. 54, right) suggests that the closed-loop control is at least as effective as the open-loop control. The early dramatic reduction of the objective (Fig. 55, top left) is a consequence of the initial control parameters already being well suited for an efficient feed-back control. The time-evolution of the controller parameters is shown in Fig. 55 (top right). The gain coefficient of the proportional part of the controller,  $K_P$ , is reduced to almost zero while the gain coefficient of the differential part of the controller,  $K_D$ , is slightly increased until it obtains a value of about 0.012. The phase shifts,  $\Delta_{tP}$  and  $\Delta_{tD}$ , converge to 0.02 and 0.03, respectively. The unsteadiness in the phases is caused by the minimization algorithm which constantly perturbs all parameters. The amplitude of this unsteadiness is identical to 2 timesteps.

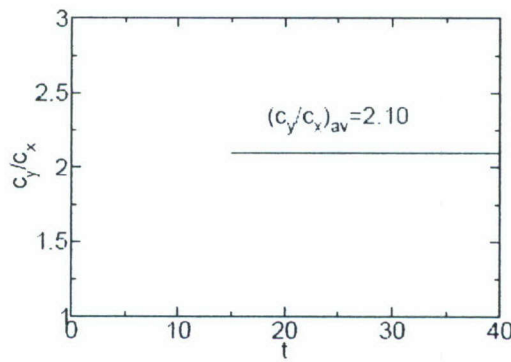


**Fig. 56:** Wall pressure coefficient  $c_p$  at locations  $x = 0.624, 0.681, 0.732$ , and  $0.773$  as obtained from Navier-Stokes simulation with  $F^+ = 7.5$  and  $B = 0.1$  (black lines) and as predicted by neural network

(red lines). The neural network was trained for  $F^+ = 5, 6, 7, 8$  and  $B = 0.1$ .

The actuation signal is shown in Fig. 55 (bottom left). During the time interval  $t = 1.6 \dots 4.8$ , the forcing signal is almost zero (as a result of the very low values of the two gain parameters). Figure 55 (bottom right) shows results from a Fourier transform of the forcing signal in the time interval  $t = 15 \dots 40$ . Dominant peaks are located at  $f = 5.7$  (amplitude  $A = 0.1$ ) and  $f = 11.3$  (amplitude  $A = 0.06$ ; first higher harmonic). A second higher harmonic with significantly lower amplitude is situated at  $f = 17$ . Frequency and amplitude of the first peak are close to the optimum values found in the open-loop study. The large amplitude oscillations of  $c_y/c_x$  which are a trademark of the uncontrolled flow disappear for  $t > 10$  (Fig. 56). While the uncontrolled flow is dominated by large vortical structures and features a large separation bubble (in the mean), with closed-loop control the flow "locks in" to the forcing (it becomes more regular) as shown in Fig. 54 (right), flow separation is reduced, and  $c_y=c_x$  is increased to 2.10. This value is identical to the optimum value achieved with open-loop flow control.

### 2.6.3 Neural Network Based Model

Neural networks (NNs) can be used for approximating functional relationships. One big advantage of NNs is their inherent ability to generalize. As will be shown in the following this can be used advantageously for deriving models of the L1M flow. If a reliable and robust NN model of the flow was available this model could be used subsequently for control purposes: The NN could be employed for prediction control. The trained NN could also be used in reverse mode by describing an inverse of the plant (or flow): A desired system state would be fed into the NN. The NN would then yield the forcing signal necessary to drive the plant (or flow) to the desired state. As mentioned earlier, NNs can also be employed directly as closed-loop controllers.

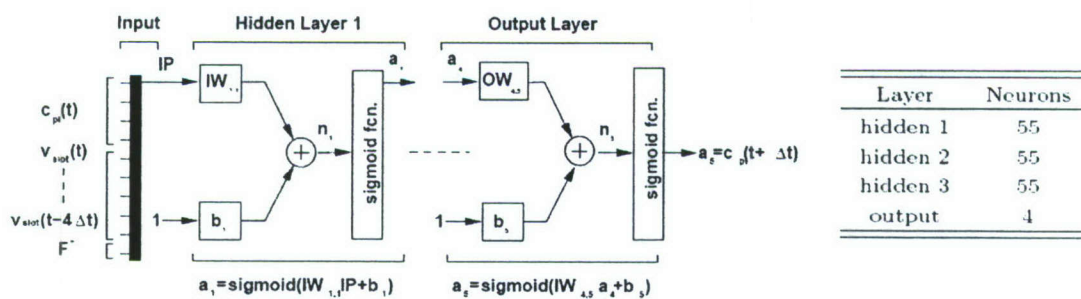


**Fig. 57: Neural network (NN) architecture, showing the first hidden layer and the output layer.  
Number of neurons per layer.**

Networks of varying complexity (hidden layers and neurons per layer) were investigated. The number of inputs and input time delays was varied and the dependence of the network training error on the ability to generalize was investigated. The space available in this paper is insufficient for reporting on all the various combinations that were tried. Instead, only one representative case is being discussed here. We decided to employ a NN for predicting the time-dependent pressure signal at 4 downstream locations ( $x = 0.624, 0.681, 0.732$ , and  $0.773$ ) on the suction side of the LPT blade. The unknown function that we wish to approximate is the relationship between the pressure sensor data at time level  $t$ ,  $cp(t)$  the forcing signal,  $v(t)$ , the forcing frequency,  $F^+$ , and the pressure sensor data at time level  $t + \Delta t$ ,  $cp(t + \Delta t)$ . The forcing signal,  $v$ , was fed into the network at 5 different time-levels,  $t$ ,  $t - \Delta t$ , ..., and  $t - 4\Delta t$ .

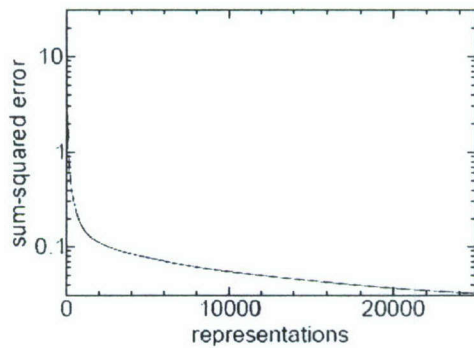


**Fig. 58: Sum-squared learning error over number of representations of training set.**

A schematic of the NN architecture that we employed for our current results is depicted in Fig. 57. The final network architecture had 3 hidden layers and 55 neurons per layer. The network was trained simultaneously with time-dependent data obtained from simulations with open-loop control for five different frequencies  $F^+ = 5, 6, 7$ , and  $8$ . The training objective was to predict the wall pressure at the sensor locations for the next time-step. This data was available from our simulations, which allowed us to employ the widely used back-propagation algorithm for training the network. The learning rate was  $\eta = 0.1$  and training was performed until the sum-squared error of the differences between the predicted and actual wall pressure data was less than 0.03 for the training data set (Fig. 58). After some experimentation we found that overtraining made the network less general and robust. The quality of the NN model was found to not only depend on the structure of the network but also on the way in which the training data was presented. The network was found to generalize poorly when the network was trained sequentially for each set (one after another). In this case, the performance of the NN depended on the chronological order in which the di

erent training sets were presented to the network, resulting in a network that was trained best for the set that was presented last. To circumvent this problem, input/output data pairs of the 4 training sets were scrambled in a random fashion before being presented to the network. We also realized that filtering of the wall pressure data obtained from CFD did greatly reduce the required training times and resulted in more robust networks that generalized better. For the NN results shown here, the wall pressure data was filtered in the frequency domain. This removed high-frequency noise and made the data more periodic in time. Finally, the input and output data were scaled to prevent saturation. The input of the sigmoid transfer function is in the interval  $[-\infty \dots \infty]$ , while the output interval is  $[0 \dots 1]$ .

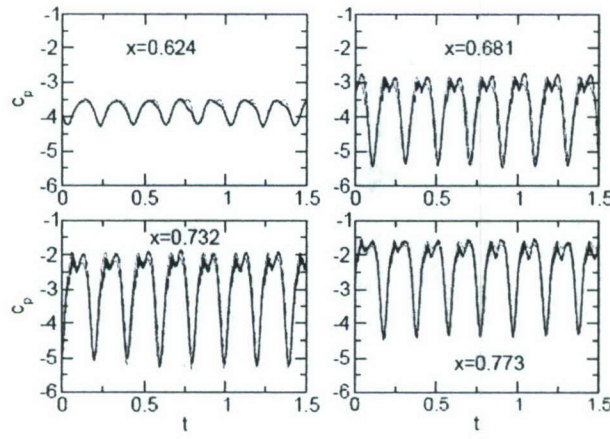


*Fig. 59: Wall pressure coefficient  $c_p$  at locations  $x = 0.624, 0.681, 0.732$ , and  $0.773$  as obtained from Navier-Stokes simulation with  $F^+ = 5$  and  $B = 0.1$  (black lines) and as predicted by neural network (red lines). The neural network was trained for  $F^+ = 5, 6, 7, 8$  and  $B = 0.1$ .*

In a second step, the trained network was then employed for predicting the future flow dynamics by prescribing a forcing function,  $v(t)$ , and forcing frequency,  $F^+$ , and feeding back the predicted wall pressure data (network output) to the network input. This was first done for the four cases that were used for network training. The result for  $F^+ = 5$  is shown in Fig. 59. The agreement between the dynamic behavior of the predicted wall pressure evolution and the wall pressure data as obtained from CFD is very good. The agreement between the predicted and computed (CFD) temporal wall pressure behavior was equally good for the 3 other cases.

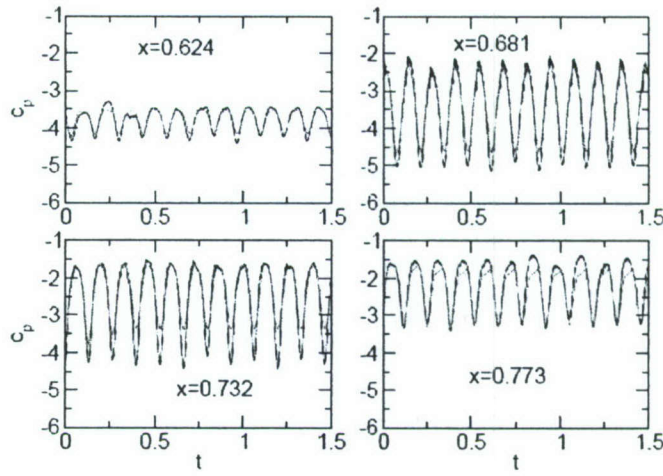


**Fig. 60:** Wall pressure coefficient  $c_p$  at locations  $x = 0.624, 0.681, 0.732$ , and  $0.773$  as obtained from Navier-Stokes simulation with  $F^+ = 7.5$  and  $B = 0:1$  (black lines) and as predicted by neural network (red lines). The neural network was trained for  $F^+ = 5, 6, 7, 8$  and  $B = 0.1$ .

An even more challenging test for the model is to predict the temporal behavior of the wall pressure sensor data for cases that were not in the training set. To this end, open-loop controlled simulations of the L1M flow with  $F^+ = 6.5$  and  $7.5$  and  $B = 0.1$  were conducted. The NN which was trained for  $F^+ = 5, 6, 7, 8$  and  $B = 0.1$  was then employed for predicting these two cases. This tested the ability of the model to generalize. Results for  $F^+ = 7.5$  are shown in Fig. 60. The quality of the network prediction is again surprisingly good. Given that the network was not trained for these forcing frequencies the current results demonstrate the tremendous potential of NNs for generalization. We also noticed that the neural network prediction was very robust. The predicted dynamics of the wall pressure data did always settle back into the correct time-periodic state even for inaccurate initial conditions or in the presence of disturbances.

### **3. DIRECT NUMERICAL SIMULATIONS OF ACTIVE FLOW CONTROL USING VORTEX GENERATOR JETS FOR MODEL GEOMETRIES**

#### **3.1 Case description**

In this approach, we investigated boundary layers on flat or curved plates subjected to the same streamwise pressure gradient as measured in the LPT experiments. The wall curvature for the curved plate matches that of the suction side of the blade used in experiments. The deliberate simplification allowed us to focus all computational resources on the regions of primary interest (the regions of actuation by the VGJs, boundary layer separation and transition). Furthermore, using simpler model geometries we were able to resolve all relevant scales from the laminar to the turbulent regime: Thus the relevant flow physics associated with LPT separation and transition as well as its control using steady and pulsed VGJs could be investigated in all necessary detail. By comparison of simulation results for the flat plate and the curved wall geometry the role of curvature on separation and its control by pulsed VGJs could be investigated. Although many questions remain open, essential details of the complicated interplay between laminar separation, hydrodynamic instability, transition and active flow control were uncovered and considerable advances were made towards understanding of the relevant mechanisms. In the following sections, results of some of the many simulations that we conducted are shown and an attempt is made to demonstrate the significant progress we have made in extracting the dominant mechanisms in LPT separation and its control.

#### **3.2 Computational Method**

For the model geometry simulations we used a highly efficient, fourth-order-accurate compact finite-difference code based on the incompressible Navier-Stokes equations in vorticity-velocity formulation which has been developed by our CFD group over many years. This code was originally developed for investigating transitional and turbulent boundary layer flows (Meitz & Fasel 2000). The code has been successfully applied for a wide range of CFD investigations of flow instability and transition, as well as for both passive and active flow control. The extensive experience with this code gives us great confidence in its accuracy and reliability. Since the effect of curvature on separation control by pulsed VGJs is poorly understood but crucial for LPT performance (Sharma 2007) we modified the high-order accurate DNS code to allow for simulations of curved wall

geometries. Care was taken that the same high-order accuracy (4<sup>th</sup> order) was maintained.

The code was optimized for massively parallel vector supercomputers such as the Cray X1E. Figure 61 shows the typical parallel performance for a three-dimensional benchmark case which was computed on the Cray X1E at AHPCRC. The problem size was increased along with the number of CPUs and ranged from ~2.1 million points (513x513x8) on 1 CPU to ~135 million points (513x513x512) on 64 CPUs. The speed-up is shown on the left, the parallel efficiency,  $\eta = (\text{ideal CPU time})/(\text{actual CPU time})$  is shown on the right. As can be seen in Fig. 61, the code scales well, especially when considering the amount of data communication that is required for such big simulations. For 64 CPUs, the speed-up is 43, which corresponds to a parallel efficiency of approximately 67%.

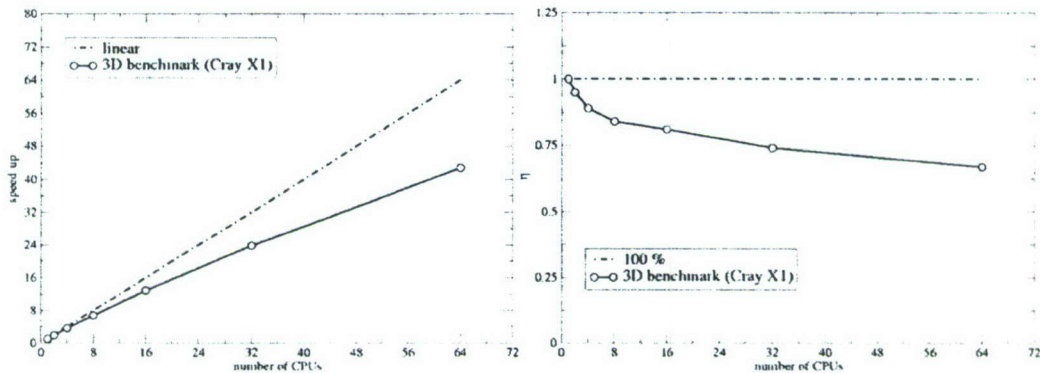


**Fig. 61: Parallel scaling of typical 3D simulations with the number of grid points ranging from  $2.1 \cdot 10^6$  to  $135 \cdot 10^6$ . The simulations were performed on the Cray X1E at the AHPCRC. Speed-up (left) and parallel efficiency (right).**

More recently we also tested this code on other supercomputers available to us that are not vector-processor machines. Figure 62 presents a comparison of run time over the number of processors on various computer platforms for a problem size of ~33 million points (1089x193x160). Although slower than the Cray X1E, close to linear speed-up is achieved on all supercomputers. However, the loss in speed compared to the Cray X1E can often be compensated for by the fact that modern supercomputers have a significantly larger number of available processors.

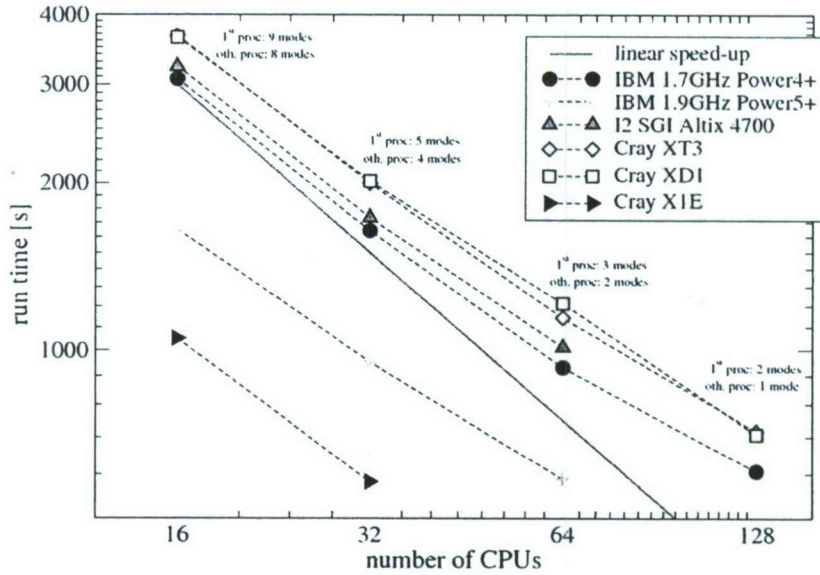


**Fig. 62: Comparison of run time as a function of processor count for typical 3D simulations using ~33 million grid points conducted on various supercomputers.**

### 3.3 Computational Domain and Boundary Conditions

Schematics of the computational setup for a curved wall and a flat plate model geometry are shown in Fig. 63 and Fig. 64. The choice of the integration domain was motivated by the setup of experiments at AFRL (Rivir, Sondergaard) and Brigham Young University (Bons). Note that for the flat plate simulations, the suction surface of the LPT blade was “unrolled”. This introduces two different coordinates, suction surface length,  $s$ , and axial chord length,  $x$ , for the downstream direction. In both cases, the flow was subjected to the same streamwise pressure gradient as measured in the experiments at AFRL at a Reynolds number of 25,000 (based on chord length,  $C_x$ ) resulting in the formation of a laminar separation bubble. A buffer domain technique was employed at the outflow boundary to prevent reflections of disturbances. While for the curved plate, a Dirichlet condition on  $v$  (suction profile) was enforced at the free-stream boundary to obtain the experimental pressure gradient, it was found to be more effective to use a gradient condition on  $v$  at the free-stream boundary for the flat plate case.

At the wall, the no-slip and no penetrations conditions were enforced, and the holes used for the VGJ investigations were modeled by prescribing appropriate Dirichlet conditions for the velocity components. The jet holes were located shortly upstream of the separation line. For simulations with flow control, both steady and pulsed VGJs were employed. The setup of the VGJ actuation is shown schematically in Fig. 65. Two different VGJ configurations were investigated: jets issued vertically into the boundary layer and jets that were pitched ( $30^\circ$ ) and skewed ( $90^\circ$ ) with respect to

the free-stream direction. For both configurations, steady and pulsed actuation was investigated. The VGJ holes were spaced at  $0.135C_x$ , had a diameter of  $0.0225C_x$ , and were resolved with  $24 \times 25$  points.

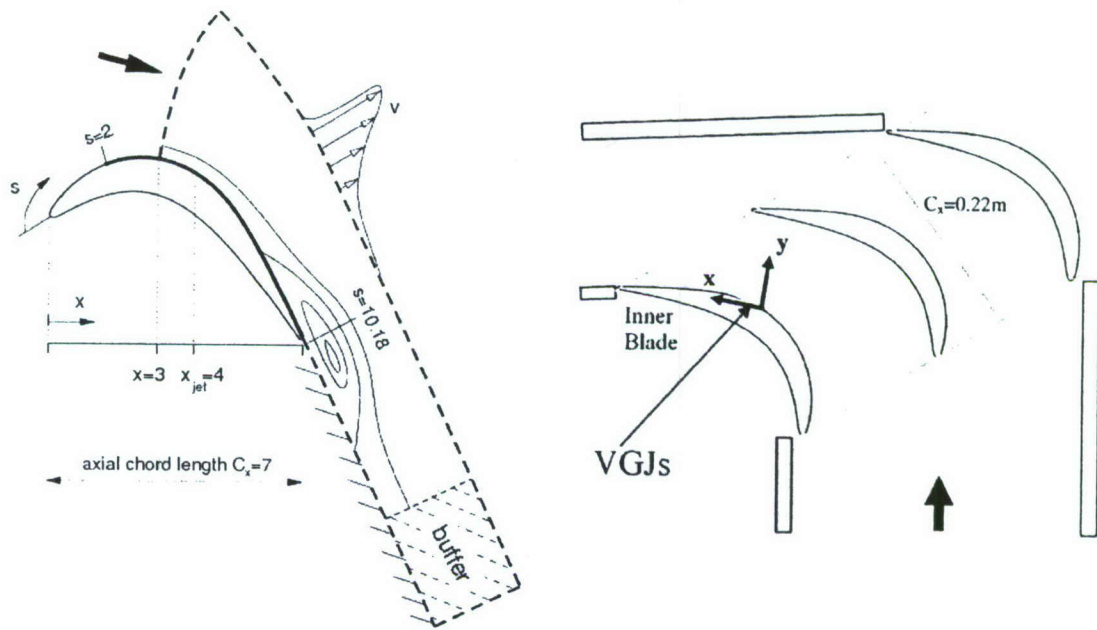


**Fig. 63: Computational setup for curved wall simulations (left) motivated by typical experimental setup (right, reproduced from Bloxham et al. 2006)**

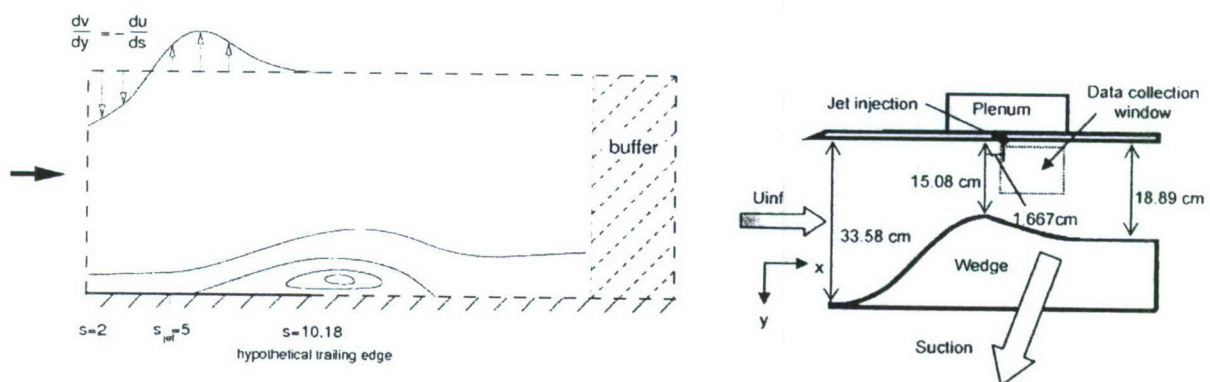


**Fig. 64: Computational setup for flat plate simulations (left) motivated by typical experimental setup (right, reproduced from Hansen and Bons 2006)**

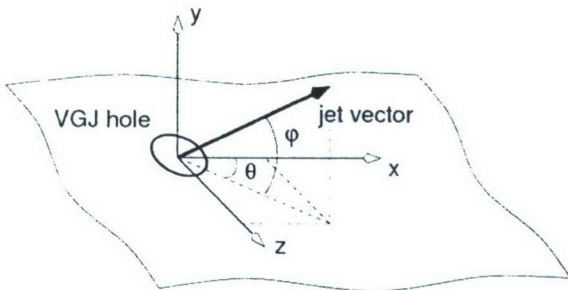


*Fig. 65: Schematic of VGJ forcing.  $\theta$ : skew angle.  $\varphi$ : pitch angle.*

The computational grids used for our simulations with the incompressible code are shown in Fig. 66. Grid point clustering is applied near the wall and near the VGJ holes. In case of the curved wall the grid was obtained from an iterative solver that was developed to generate orthogonal curvilinear grids based on the method of Duraiswami and Prosperetti (1992). At each step of the iteration a set of elliptic equations is solved using a multigrid algorithm similar to the one used in the Navier-Stokes code. The distribution of boundary points is obtained from a Newton-Raphson sub-iteration. Control over grid point clustering is provided by appropriate specification of a distortion function  $g$  in the elliptic equations. The grid generator was vectorized and ported to the Cray X1E to accelerate the grid generation process because it was found that for obtaining high-quality orthogonal grids, the set of elliptic equations had to be solved hundreds of thousands of times.

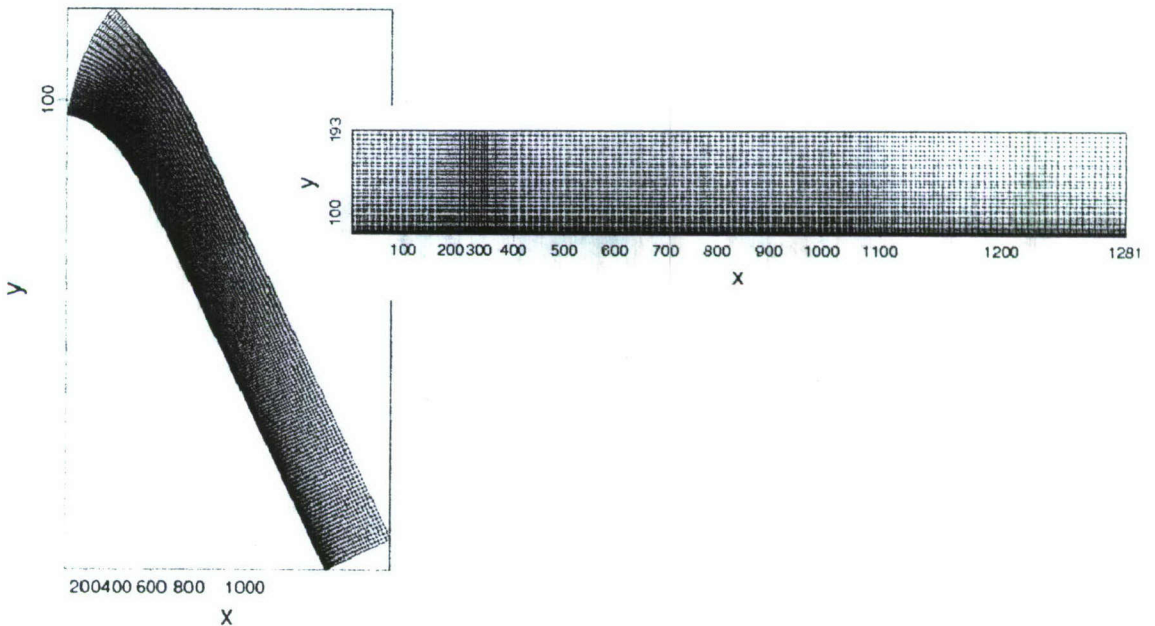


*Fig. 66: Schematic of typical computational grids employed for VGJ simulations on a curved wall (left) and a flat plate (right). For clarity, only every 4<sup>th</sup> point is shown in both x and y.*

### 3.4 Results

Results of simulations for the natural, uncontrolled flow are presented first. Then, results obtained from simulations for the controlled flow for the flat plate model geometry using steady and pulsed VGJs are discussed. Finally, we present results obtained for the curved wall geometry using pulsed VGJ actuators.

#### 3.4.1 Uncontrolled “Natural” Flow

A comparison of the wall-pressure coefficient versus the suction surface length  $s$  with experimental data for the uncontrolled case is shown in Fig. 67. In both cases (curved and flat plate), good agreement was obtained with the experimental pressure distribution (Bons et al. 2001a, Sondergaard et al. 2002a, Huang et al. 2003). The pressure distributions along the curved plate and the flat plate are not in perfect agreement which, at this point, prevented us from unequivocally identifying the effects of curvature. Achieving a perfect match in the pressure distributions (either along the wall or in the outer inviscid region) is by no means trivial and is left for future investigations. The pressure plateau downstream of 62% SSL indicates the region of boundary layer separation.

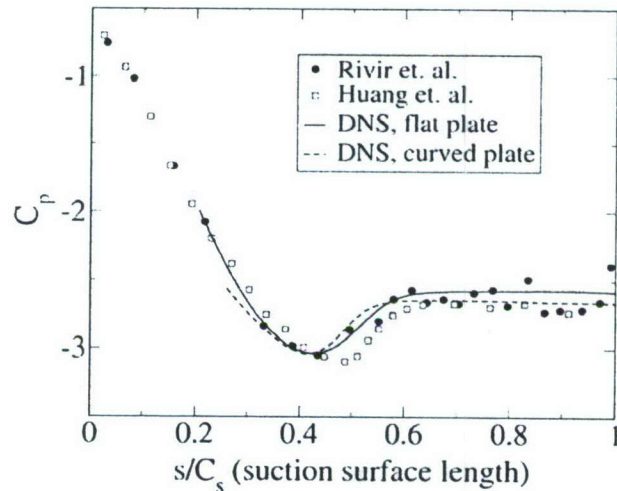
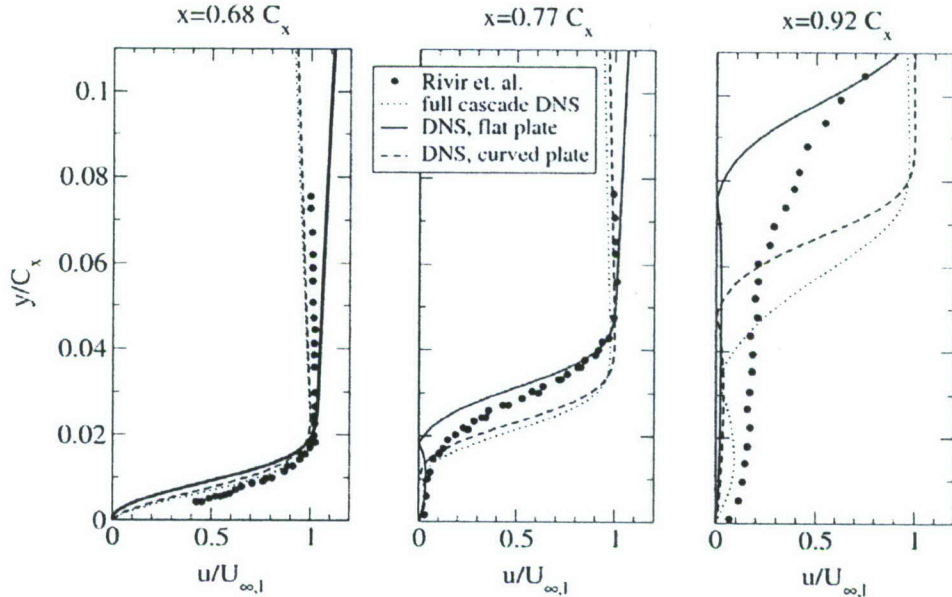


Fig. 67: Wall pressure coefficient  $C_p$  for the uncontrolled, separated flow plotted over the suction surface length. Comparison between simulations and experiments by Rivir and co-workers.

Velocity profiles at various downstream locations are shown in Fig. 68 together with experimental data and results obtained from a full blade DNS (section 2). The experimental profiles do not show negative velocities because they were obtained from hot-wire measurements. While

the experimental profile at 92%  $C_x$  indicates attached flow, it is in fact separated. The differences between the velocity profiles along the curved wall and the flat plate are not exclusively due to the difference in the imposed wall pressure distribution, but can also be attributed to the curvature itself which naturally introduces a surface-normal pressure gradient that is missing in the flat plate case.



**Figure 68. Velocity profiles for the uncontrolled, separated boundary layer.**

Overall, the careful setup of the numerical simulations resulted in a good agreement with the experimental data for the base flow. Typical results from a simulation of the uncontrolled, separated boundary layer on a curved plate are shown in Fig. 69. Flow structures shown in Fig. 69 are identified using the  $\lambda_2$  vortex criterion by Jeong & Hussain (1995). In the mean, the boundary layer separates at  $x=4.7$  and reattaches at approximately  $x=9.1$ . The values obtained from the “unrolled” flat plate simulation are  $x=5.7$  and  $x=15.8$  for separation and reattachment, respectively. Note that since the trailing edge of the PackB plate is located at  $x=7.0$  (curved wall), the results indicate that the flow for an actual LPT blade would, for this case, not reattach to the blade surface.

Although the pressure gradients for the flat plate and the curved wall are not exactly identical, we tried to qualitatively access the effect of curvature on the extent of separation. Comparing time- and spanwise averaged streamlines as well as contours of time-averaged spanwise wall vorticity along the flat plate and the “unrolled” curved wall (see Fig. 70), we find indications for a larger separated flow region for the curved wall. Separation occurs approximately at the same location for both cases since the simulation setup was tailored towards matching the experimental pressure distribution over the blade. However, for the curved geometry the flow reattaches (in the mean) much later.

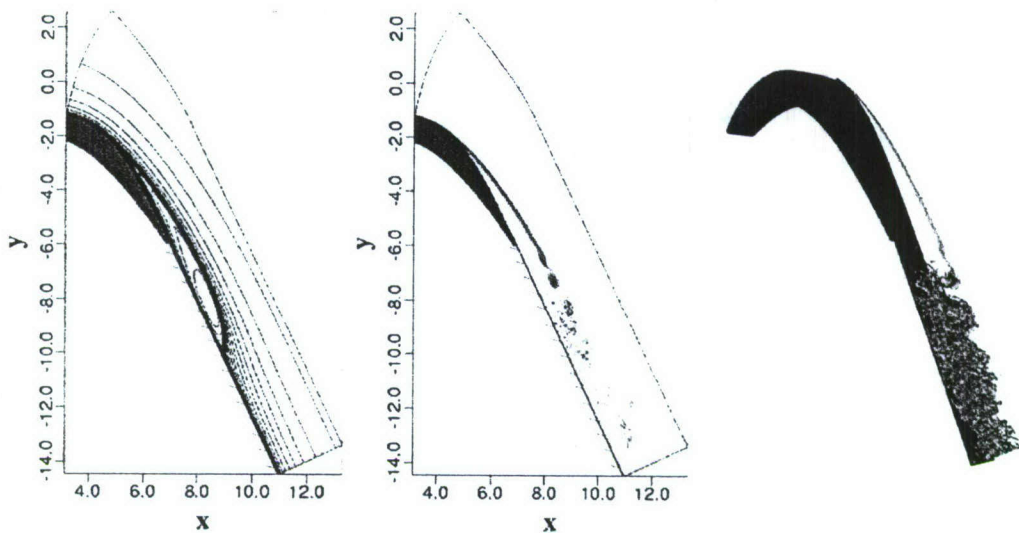


**Fig. 69: DNS of uncontrolled laminar separation bubble on curved wall geometry. Time- and spanwise-averaged streamlines (left); Instantaneous contours of spanwise vorticity (center); Instantaneous iso-surfaces of  $\lambda_2=25$  (right). Also shown are contours of instantaneous spanwise vorticity  $\omega_z$ .**

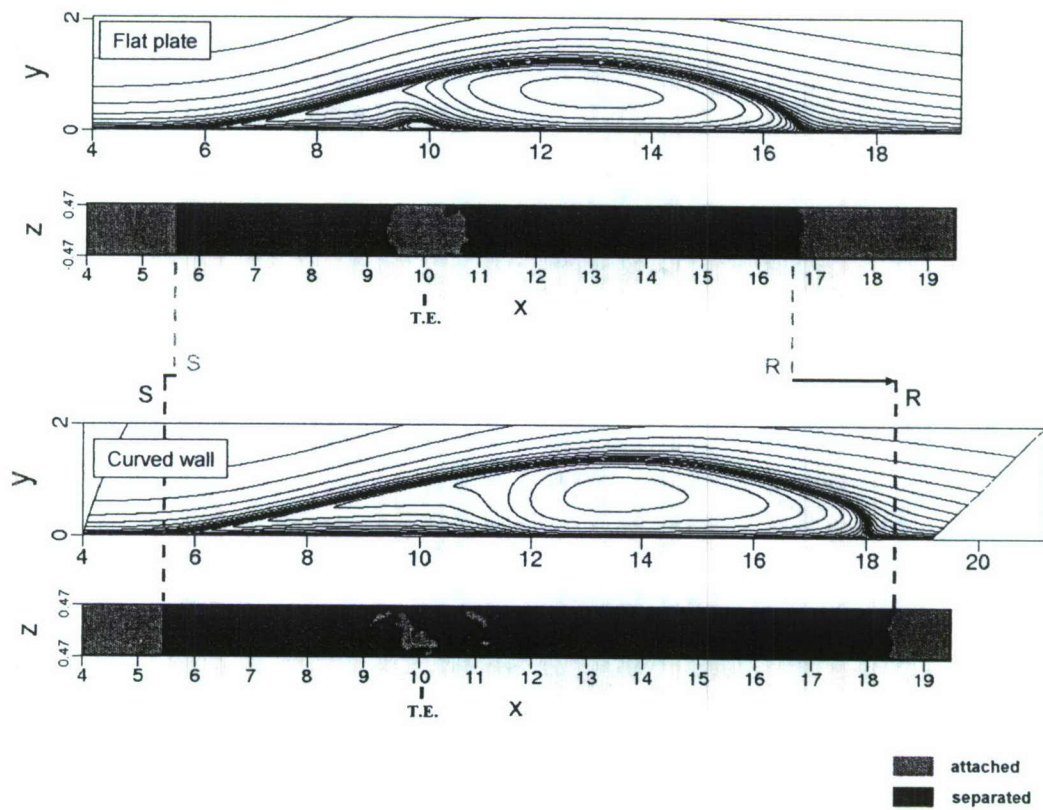


**Fig. 70: Time-and spanwise averaged streamlines and contours of time-averaged spanwise wall vorticity  $\omega_z$  for the uncontrolled laminar separation bubble on a flat plate (top) and a curved wall (bottom). T.E. indicates the location of the hypothetical trailing edge.**

### 3.4.2 Steady VGJs; Flat Plate Geometry

In this section we consider the effect of steady VGJ actuation on the separated flow along the flat plate model geometry. For a blowing ratio of  $B=0.316$ , vertical versus angled VGJ injection is compared in Fig. 71. Following a rapid decay immediately downstream of the forcing location, the longitudinal vortices generated by the jets become amplified in the region of strong streamline curvature associated with the separating boundary layer. A local stability analysis of streamwise velocity profiles indicates that a Görtler instability mechanism (due to streamline curvature caused by the separated boundary layer) may potentially be responsible for this amplification.

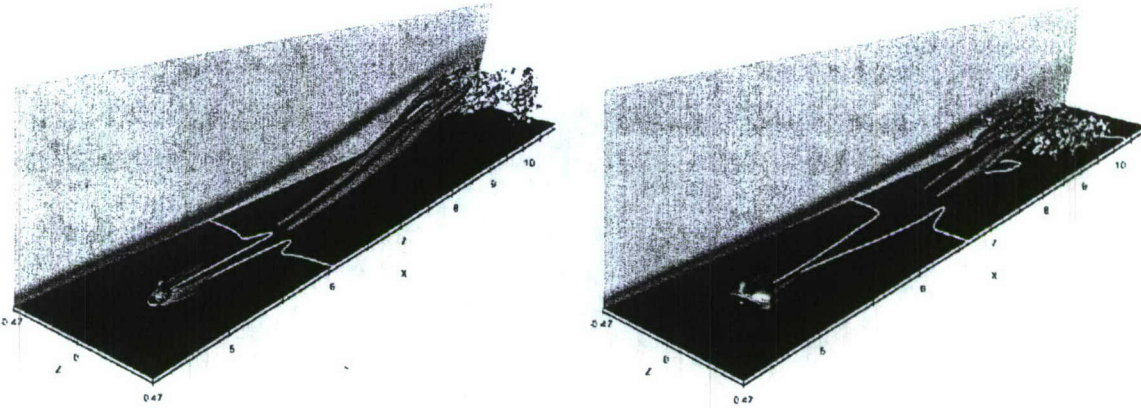


**Fig. 71: Flow control using steady VGJs. Time-averaged iso-surfaces of  $\lambda_2=-2$  and iso-contours of spanwise vorticity  $\omega_z$ . White lines indicate locations of  $\omega_z=0$  (separated line). Left: vertical injection; Right: angled injection.**

A detailed investigation of the unsteady flow structures reveals that the final stages of the laminar-turbulent transition process, in each of the two cases (angled and vertical jets), can be characterized by the formation of hairpin-like vortices (Fig. 72). The breakdown to turbulence occurs more rapidly for angled injection which can be attributed, in part, to the (in the spanwise direction) deeper penetration of the jets into the boundary layer. This is illustrated in Fig. 73. However, from this and many other simulations we found that, once the flow was separated, an accelerated breakdown to turbulence by itself does not necessarily provide the most effective mechanism for optimal separation control. In other words, the mixing associated with the small-scale flow structures appeared to be rather weak, and a considerable streamwise distance was required before enough free-stream momentum was entrained to reattach the flow.

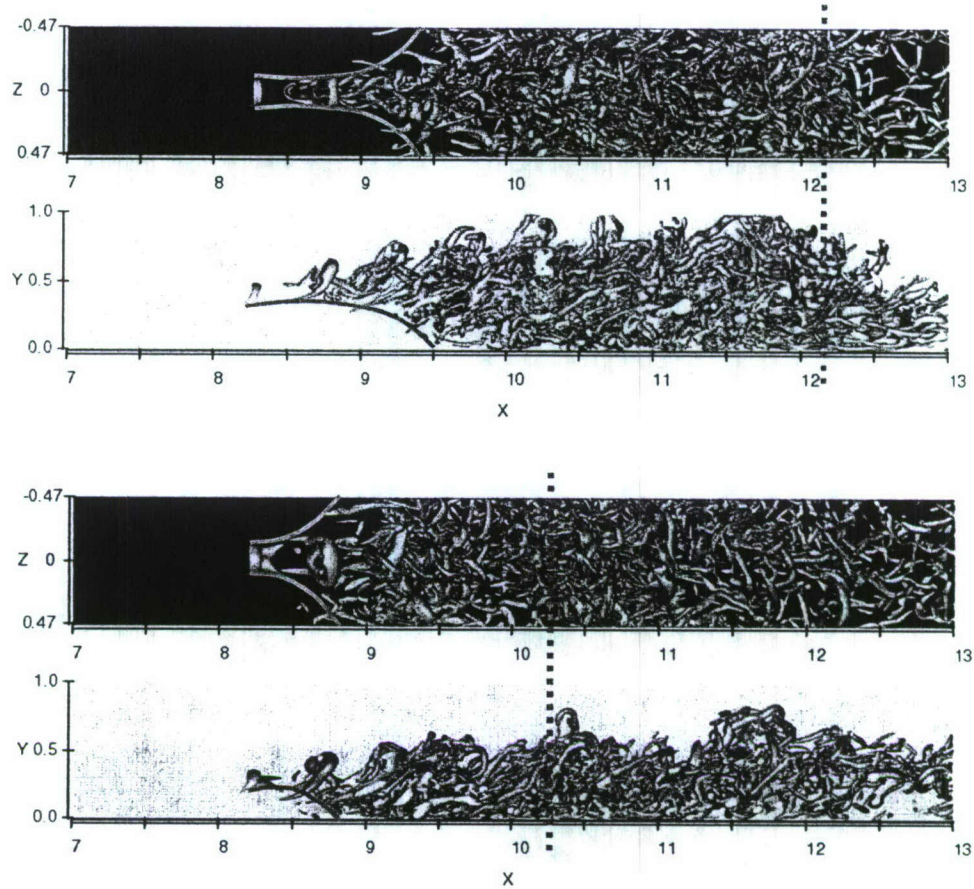


**Fig. 72:** Flow control using steady VGJs. Instantaneous visualizations (top and side views) of iso-surfaces of  $\lambda_2=50$ . Top: vertical injection; Bottom: angled injection. (- - -) spanwise averaged reattachment point.

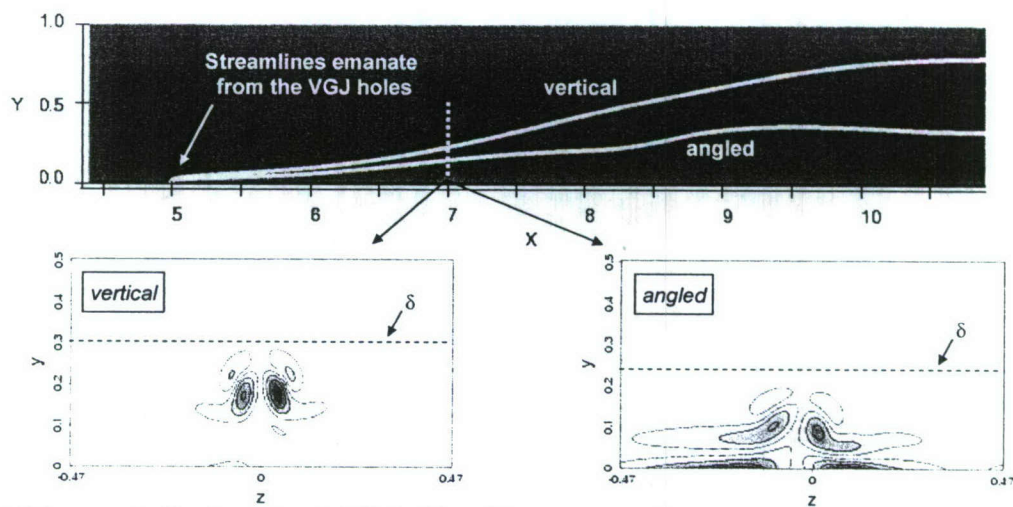


**Fig. 73:** Flow control using steady VGJs. Top: Time-averaged streamlines emanating from the center of the VGJ holes; Bottom: Iso-contours of streamwise vorticity at  $x=7$  (Blue: clockwise rotation, red: counter-clockwise rotation).

We also studied blowing ratios in the range from  $B=1$  to  $B=2$ . Mean flow results indicate that, up to a “threshold” blowing ratio of  $B=1$ , angled VGJs were more effective than vertical VGJs in reducing flow separation. Again, from many other simulations (not shown here) we learned that beyond this “threshold” value the trend was reversed, however, and vertical jet injection was more effective resulting in fully attached flow along almost the entire surface (in the spanwise average). A comparison for the two cases – vertical versus angled – by instantaneous visualizations of iso-surfaces of  $\lambda_2=-50$  for a blowing ration of  $B=2$  is shown in Fig. 74.

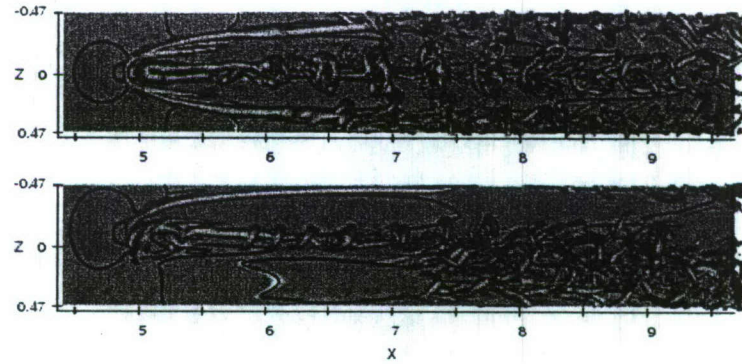


*Fig. 74: Flow control using steady VGJs with blowing ratio  $B=2$ . Instantaneous top views of iso-surfaces of  $\lambda_2=-50$ . Top: vertical jet injection; Bottom: angled jet injection (red color indicates separated flow).*

Comparison with Fig. 72 confirms that the dominant physical mechanism has changed as the jet amplitude was increased. For  $B=2$ , with vertical injection, a strong horseshoe vortex develops that “wraps around” the column of fluid injected by the jet (Fig. 75). As a result of this horseshoe structure, entrainment of high-momentum fluid from the free stream is increased significantly, thereby effectively generating a “new” boundary layer behind the jet exit hole. Due to the lack of symmetry associated with the cross-stream injection of the angled VGJs, the oncoming boundary layer for the case with angled VGJs was found to be mainly diverted in the direction of the jet injection. Consequently, only “one-legged” horseshoe structures developed, thus leaving “one side” of the surface essentially unaffected by the forcing. In fact, as a result of the entrainment of high-momentum fluid on the “upper side” of the surface (when viewed from above), low-momentum fluid appeared to be transported to the “lower side”, thereby further destabilizing the flow which is already at the verge of separation. This observation led to the conclusion that, for angled VGJs, even a further increase of the blowing ratio may not lead to an attached flow along the entire surface (for the present hole spacing and diameter). Comparison of Figs. 72 and 74 also illustrates that the laminar-turbulent transition process was delayed at the larger blowing ratio and that the primary control mechanism for both cases was “laminar” in nature. Also, and this is consistent with

experimental observations (Hansen and Bons 2006), the streamwise vortices maintain their coherence over a longer downstream distance for angled injection.

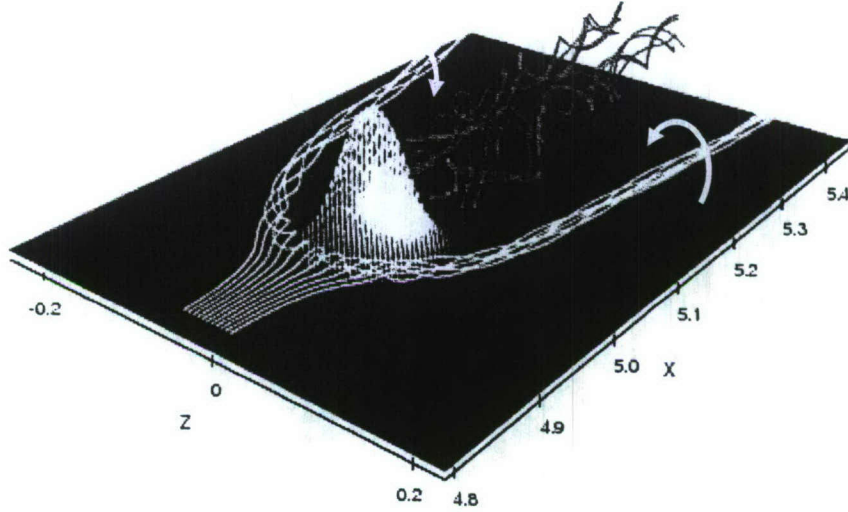


**Fig. 75: Visualization of the horseshoe vortex. Yellow: time-averaged streamlines passing through a horizontal rake located at  $x=4.8$ ,  $y/\delta \approx 0.14$ ; White: jet-exit velocity vectors.**

### 3.4.3 Pulsed VGJs; Flat Plate Geometry

First, results are presented for angled and vertical jet injection for a duty cycle of  $\tau=10\%$  and a blowing ratio of  $B=1$ . Since the flow structures that are generated downstream of the forcing location (see Fig. 76, *left*) closely resemble the hairpin vortices that develop in the late stages of Klebanoff-type transition scenarios (see Fig. 76, *right*), a “by-pass” transition mechanism was at first considered to be the most relevant mechanism for controlling LPT separation with pulsed VGJs. However, from other simulations we realized that other mechanisms may also play a significant role. An indication for this is already seen in Fig. 76 (*left*) as the hairpin vortices and longitudinal structures that were generated by the pulsed VGJs decay in the streamwise direction. This led us to speculate that the bypass mechanism and the resulting vortical structures may only be indirectly responsible for the effectiveness of pulsed VGJs.

More important, and surprising at first, the simulations revealed that for both vertical and angled injection, strong spanwise coherent vortical structures were found to develop in the separated flow region, only later and further downstream followed by the rapid generation of smaller and smaller scales (Fig. 77). Of particular importance was the observation that the developing small-scale structures were part of very large-scale, spanwise coherent structures, which led to the conjecture

that the formation of these spanwise coherent structures may be the primary cause for the increased effectiveness of pulsed VGJ actuation versus steady VGJs.

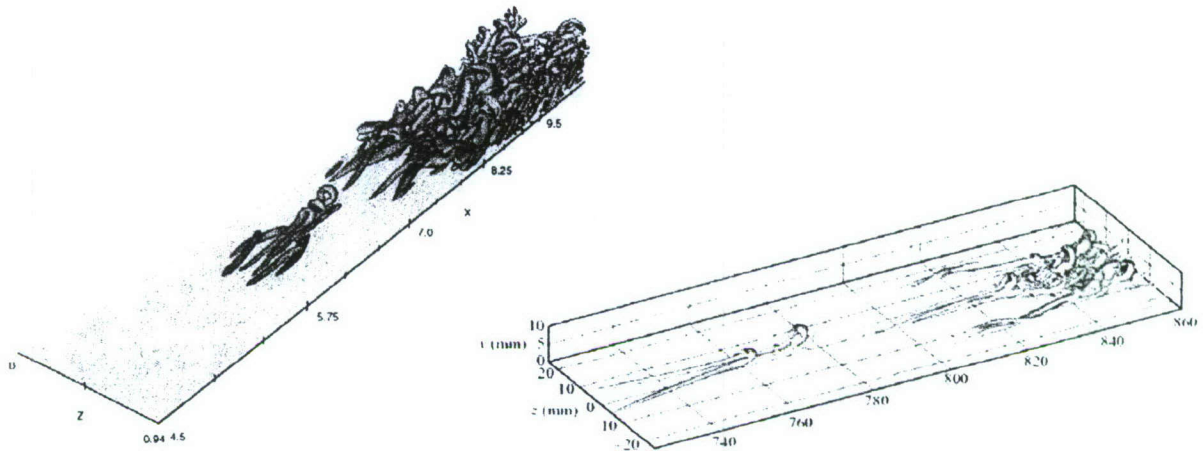


**Fig. 76:** Left: Flow control using pulsed vertical VGJs ( $\tau=10\%$ ,  $B=1$ ). Iso-surfaces of  $\lambda_2=-5$ ; Right:  $\Lambda$ -vortices in a transitional flat-plate boundary layer (reproduced from Bake et al., 2002).

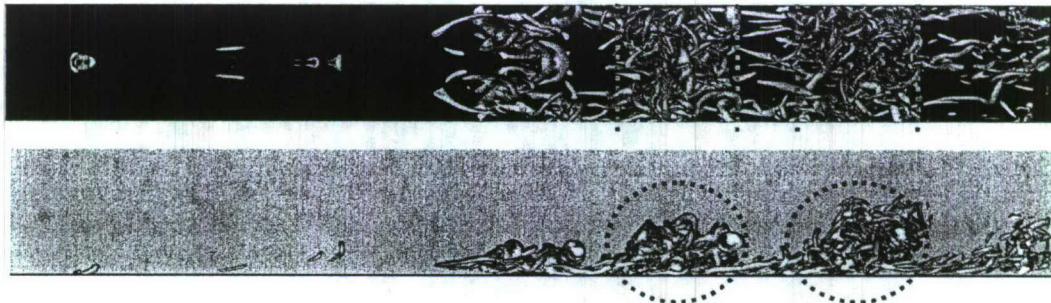


**Fig. 77:** Flow control using pulsed vertical VGJs ( $\tau=10\%$ ,  $B=1$ ). Instantaneous visualization of  $\lambda_2=-25$ ; top and side view.

A proper orthogonal decomposition (POD) (Lumley 1967, Sirovich 1987) of the time-dependent flow data confirmed this conjecture. The spanwise coherent structures are indeed by far the most energetic unsteady flow structures for both, vertical and angled pulsed injection. The formation of the structures was in perfect phase with the pulsed actuation in both instances indicating that these structures are generated by the pulsed VGJs. Results of the POD analysis for the case of vertical injection are shown in Fig. 78 for the case with vertical pulsing. It is obvious that the dominant physical mechanism must somehow be similar for both the vertical and angled jet injection. This, of course, is contrary to the findings for steady jets, as discussed before.

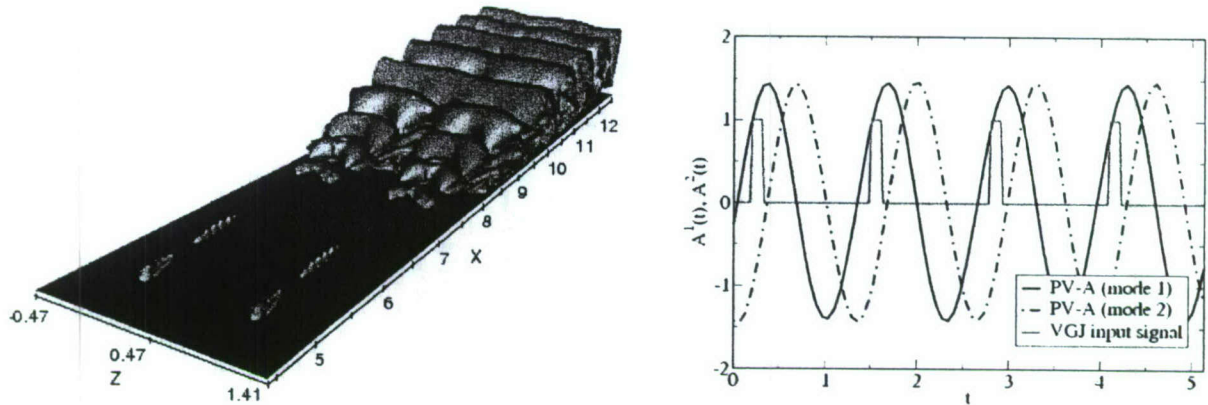


**Fig. 78: Flow control using pulsed vertical VGJs ( $\tau=10\%$ ,  $B=1$ ). Left: POD mode 1 for the case with vertical injection; Right: Normalized forcing signal at the VGJ injection location and POD time functions associated with mode 1 and mode 2.**

We conjectured that the similar effectiveness of angled and vertical jets must be due to the unsteady (periodic) pulsing and the resulting large-scale spanwise coherent structures must, therefore, be a consequence of the 2-D disturbance component of the localized forcing (as a result of employing the jets “in phase”). We now understand that due to the shear layer instability of the separated boundary layer (inflection point in the velocity profiles in the separated region), the 2-D disturbances undergo a strong amplification in downstream direction. This was confirmed by plotting the amplitude of the 2-D component of the velocity disturbance versus the downstream direction (Fig. 79). After a transient, downstream of the exit holes for the VGJs, the 2-D disturbances experience approximately exponential (in the log-plot linear) growth. (Exponential growth is an indication of a linear instability mechanism.) Thus, the main conclusion here is, that the control is so effective because a linear instability mechanism is exploited. As a consequence of this mechanism, the energy required for the amplification of the 2-D disturbances is provided by the base-flow and comes “free of charge”.

Additional results of simulations using pulsed VGJs at various sub-harmonic or higher frequencies (with respect to the “baseline case” frequency) are shown in Fig. 80. The duty cycle  $\tau=10\%$  was held constant for these simulations. Forcing with lower forcing frequencies had relatively little effect on the extent of the separated region when compared to the “baseline case”, while increasing the pulsing frequency lead to a significant reduction in the control effectiveness. This result can be explained by the hydrodynamic stability characteristics of the separated shear layer. Thus, the results of Fig. 80 are an additional confirmation, that for most effective and efficient control the instability of the underlying flow needs to be exploited. As shown by the amplitude

spectra in Fig.

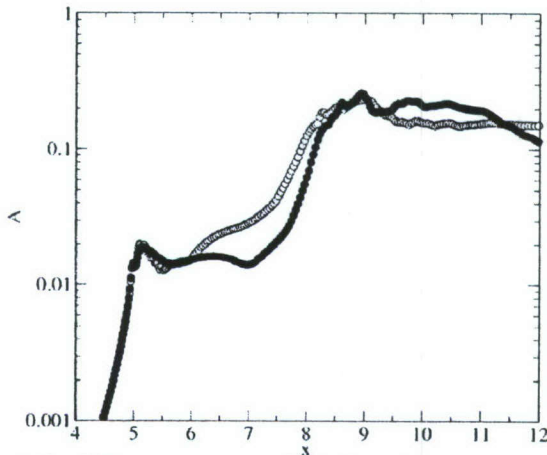


**Fig. 79:** Fourier amplitude of the 2-D component of  $u'$  disturbance velocity (max. over  $y$ ) for the fundamental frequency  $f=0.77$ . Open symbols: vertical injection; Closed Symbols: angled injection.

80 (right), pulsed forcing with a fixed duty cycle introduces a number of higher harmonics of the fundamental pulsing frequency, and the spectrum shifts to the right or left depending on the value of the fundamental pulsing frequency. Consequently, as long as the pulsed forcing generates frequencies to which the flow is hydrodynamically unstable, the amplification of the resulting instability modes will yield an effective control of the separation.

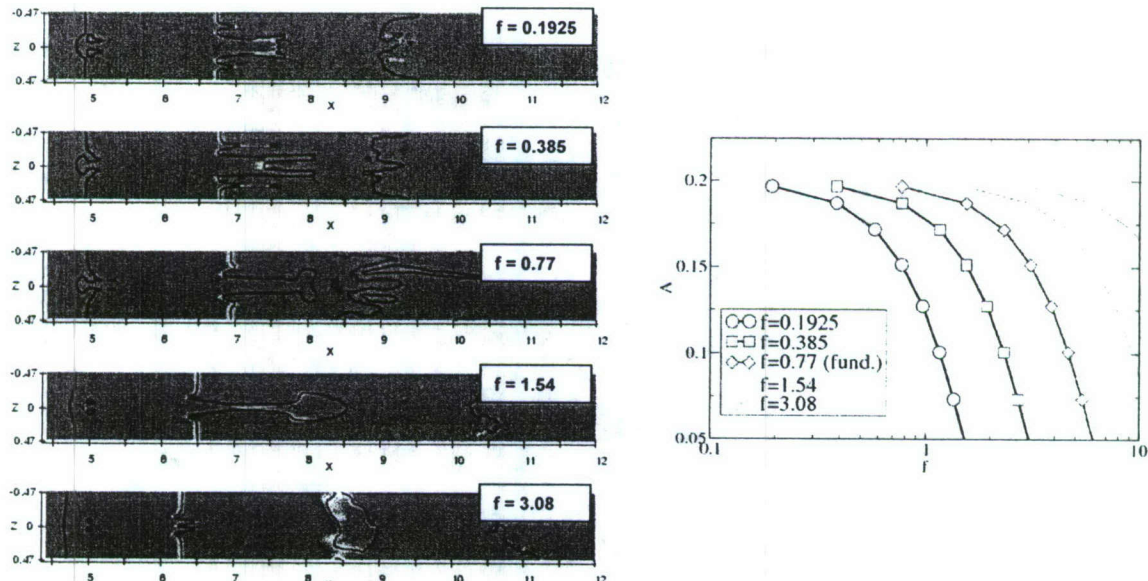


**Fig. 80:** Flow control using pulsed vertical VGJs for various pulsing frequencies ( $\tau=10\%$ ,  $B=1$ ). Left: Contours of spanwise wall vorticity  $\omega_z$  (red: separated flow; grey: attached flow) Right: Frequency spectra for pulsed VGJ.

We also carried out additional simulations where we investigated the effect of the duty cycle in the range from 10% to 100% (100% means steady forcing) and adjusted the blowing ratio for keeping the jet momentum coefficient,  $c_\mu$ , constant. In all cases the control was almost equally effective except when  $\tau$  reached 100%. In this case, the separation length increased significantly (not shown). While this observation alone was not surprising, the observation that this increase happened very "suddenly" certainly was. This finding further corroborated the conjecture that the exploitation of an inviscid linear hydrodynamic instability mechanism was primarily responsible for the stunning effectiveness of pulsed VGJs for LPT separation control. The observation that all the unsteady cases were equally effective led to the conclusion that, from an engineering point of view, the choice of the duty cycle does not seem to be as critical as that of the pulsing frequency, again a confirmation of the underlying 2-D instability mechanism. Lower duty cycles are preferable as they require a smaller mass flux (when the momentum coefficient,  $c_\mu$ , is not kept constant). Instantaneous flow visualizations (Fig. 81) and results obtained from a POD analysis of the flow data (Fig. 82) reveal that, for large duty cycles (here:  $\tau=40\%$ ), the flow structures are being concentrated in areas with oblique coherence. This stunning observation led to the conjecture that the amplification of 3-D instability modes may lead to the formation of oblique coherent structures, which, to the best of our knowledge, has not been reported in the literature in the context of laminar separation bubbles. Since no conclusive explanation could be offered for the observed shift from spanwise to oblique coherence, additional investigations are needed to further clarify this issue. Currently, we are speculating that an oblique resonance instability mechanism may be present.

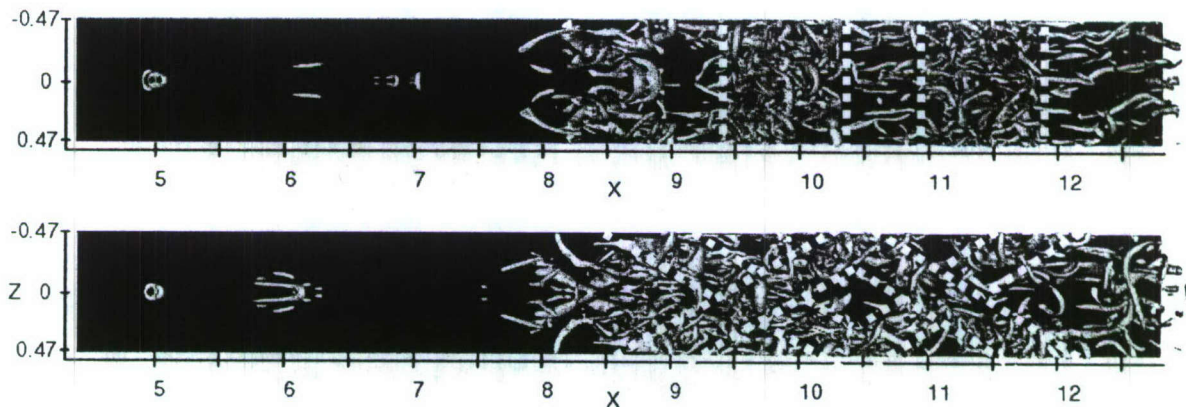


**Fig. 81: Flow control using pulsed vertical VGJs. Instantaneous top views of iso-surfaces of  $\lambda_2=-2$ . Top: duty cycle  $\tau=10\%$ ; Bottom:  $\tau=40\%$ .**

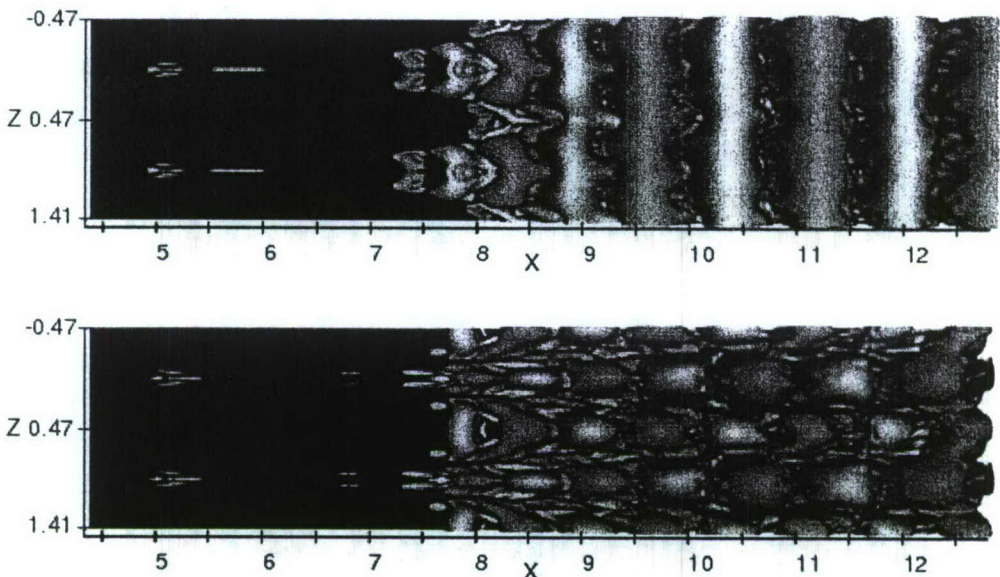


**Fig. 82: Flow control using pulsed vertical VGJs. POD mode 1, top view towards the surface. Top: duty cycle  $\tau=10\%$ ; Bottom:  $\tau=40\%$ .**

### 3.4.4 Pulsed VGJs; Curved Wall Geometry

Our numerical investigations for the flat plate geometry showed that pulsed VGJ actuation is both effective and efficient. We repeated some of the most interesting flat plate cases for the curved wall geometry in order to determine whether curvature affects the physical mechanisms that we identified for the flat plate. However, as mentioned earlier, since the pressure gradients were not exactly identical in the flat plate and curved wall simulations, our comparisons of both cases are of a qualitative nature only.

For the first curved wall case discussed here we employed pulsed VGJs with a forcing frequency  $f=64$  Hz, a blowing ratio of  $B=1$  and a duty cycle of  $\tau=10\%$ . A side view and a close-up of the instantaneous flow structures in the separation flow region are shown in Fig. 83. As for the flat plate, the VGJ actuation leads to the formation of hairpin vortices and longitudinal structures. In addition, as for the flat plate case, the flow dynamics in the transition region are dominated by spanwise coherent structures. These observations lead us to the conclusion that the mild geometric curvature of the curved plate investigated here does not significantly alter the flow physics as identified for the flat plate. Thus, our understanding of the relevant flow physics is not affected by the presence of curvature and it does not affect the effectiveness of the VGJ actuation for reducing and controlling separation. Rather, these results can serve as a justification for the simplifications that we made earlier when we employed a flat plate geometry for studying active flow control for LPT blades.



**Figure 83.** Instantaneous flow visualizations (iso-surfaces of  $\lambda_2=25$ ) for uncontrolled “natural” flow (left) and controlled flow using pulsed vertical VGJs with  $\tau=10\%$  (right). Also shown are iso-contours of instantaneous spanwise vorticity  $\omega_z$ .

On the other hand, certain differences in the overall flow field do exist and might become more important when the wall curvature is increased. For example, when comparing Figs. 70 and 84 it can be seen, that for the flat plate VGJ actuation delays separation whereas for the curved wall, separation occurs approximately at the same location as for the uncontrolled flow. We believe that this can be attributed to the stronger decay of the longitudinal vortices associated with the VGJ actuation in case of the curved wall (convex wall). For the flat plate these vortices are much less attenuated in downstream direction. Streamwise vortices can help entrain free stream momentum towards the wall and thus aid in delaying separation.

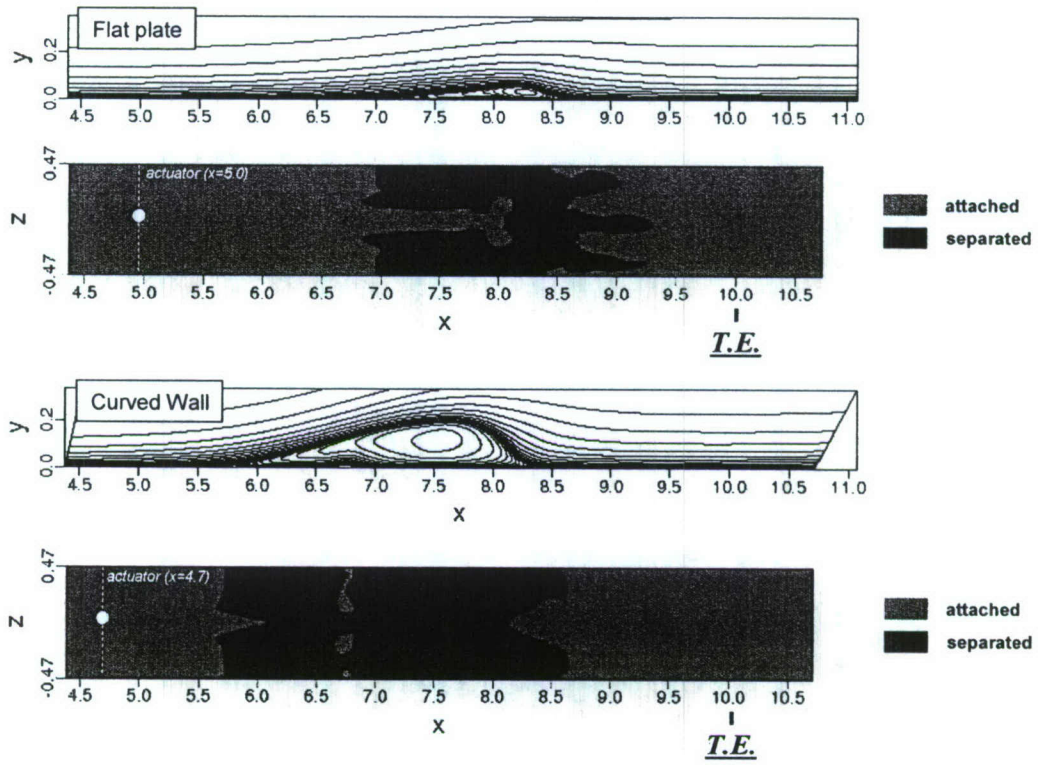


**Fig. 84:** Time-and spanwise averaged streamlines and contours of time-averaged spanwise wall vorticity  $\omega_z$  for the controlled laminar separation bubble on a flat plate (top) and a curved wall (bottom) using pulsed VGJ actuation. T.E. indicates the location of the hypothetical trailing edge.

Next, it was of interest to explore whether oblique coherent structures for intermediate duty cycles (e.g.  $\tau=40\%$ ) which we identified for the flat plate also appeared on the curved wall. We conducted simulations with duty cycles ranging from  $\tau=10\%$  to  $\tau=80\%$ . Figure 85 shows time- and spanwise averaged data for the spanwise vorticity component  $\omega_z$ . Separated flow regions on the curved wall are marked in red. A comparison of the wall-pressure coefficient for all cases is depicted in Fig. 86. These results confirm our previous conclusion that the duty cycle does not substantially influence the effectiveness of pulsed VGJ actuation. However, a POD analysis of the flow fields obtained from the cases with  $\tau=10\%$  and  $\tau=40\%$  (see Fig. 87) reveals once again a fundamental change in the organization of the coherent flow structures when the duty cycle is changed from 10 to 40%. Apparently, the presence of a curved wall does not alter this behavior.

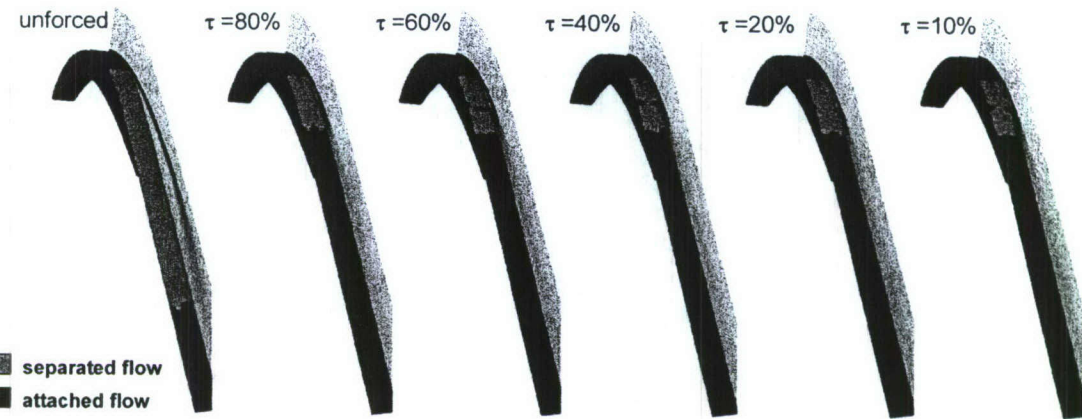


*Fig. 85: Time- and spanwise averaged vorticity component  $\omega_z$  (side wall) and time-averaged wall contours  $\omega_z$  for flow control simulations using pulsed VGJs and various duty cycles  $\tau$ .*

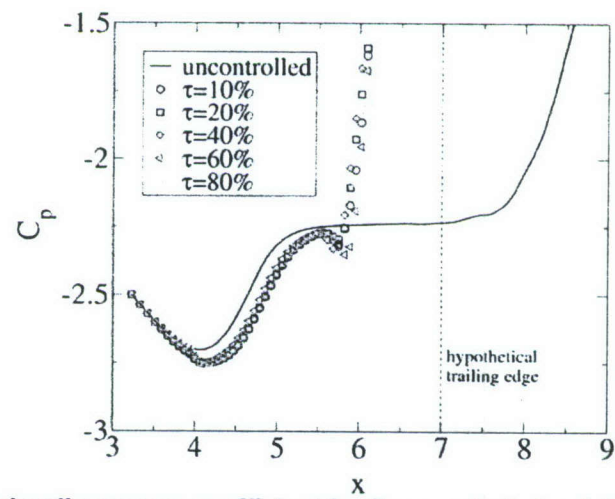


*Fig. 86: Time-averaged wall pressure coefficient for flow control simulations using pulsed VGJs and various duty cycles  $\tau$ .*



**Fig. 87:** Flow control using pulsed vertical VGJs. POD mode 1 and 2 for duty cycle  $\tau = 10\%$  (left, center left), POD mode 1 and 2 for duty cycle  $\tau = 40\%$  (center right, right).

### 3.4.5 Effect of Hole Spacing

In all previously presented simulations using the incompressible code the spanwise domain extent was 13.5% of the axial chord length  $C_x$ . The holes had a diameter of  $D=4\text{mm}=2.25\% C_x$ . Due to the assumed symmetry and spectral discretization in the spanwise direction this length is equivalent to the spacing of the VGJ holes. Furthermore, the spanwise extent represents the smallest wavenumber (largest wavelength) that is resolved by the spectral discretization – smaller wavenumbers are suppressed, but could possibly be important. We deemed it necessary to investigate the effect of the hole spacing and of the domain width as both parameters will influence the behavior and interaction of 2-D and 3-D modes in the domain. In particular, the hole spacing determines what 2-D and 3-D modes are introduced in the domain and the domain width determines what 3-D modes are resolved (or suppressed). In summary, these studies allow us to determine the importance of 2-D vs. 3-D instability mechanisms for effective separation control using pulsed VGJs. Many open questions remain such as the question if the hole spacing can be chosen such that 3-D breakdown is delayed and the 2-D hydrodynamic instability mechanisms can be optimally exploited for flow control.

First we conducted a series of simulations where we decreased or increased the hole spacing by computing with a smaller or larger spanwise domain with one VGJ located in the center of the domain. The spanwise resolution was identical in all cases and the momentum coefficient  $c_\mu$  (per unit depth in spanwise direction) was kept constant by adjusting the blowing ratio  $B$  (a larger hole

distance requires a larger blowing ratio). The results presented below include hole spacings of  $2D$  (4.5% chord length  $C_x$ ),  $6D$  (13.5%  $C_x$ ),  $10D$  (22.5% chord length  $C_x$ ) and  $20D$  (45.5%  $C_x$ ) where  $D$  is the hole diameter. Instantaneous visualizations of iso-surfaces of  $\lambda_2$  are presented in Fig. 88. As expected, we observe a higher degree of two-dimensionality (spanwise coherence) when the holes are closer together. For larger hole spacings ( $10D$ ,  $20D$ ) the 2-D coherence is weaker. Surprisingly, however, even VGJ actuation with a  $20D$  hole spacing is still effective in reducing separation on the curved wall geometry. This can be concluded from Fig. 89 which shows time- and spanwise averaged streamlines for the smallest ( $2D$ ) and largest ( $20D$ ) hole spacing that we considered.

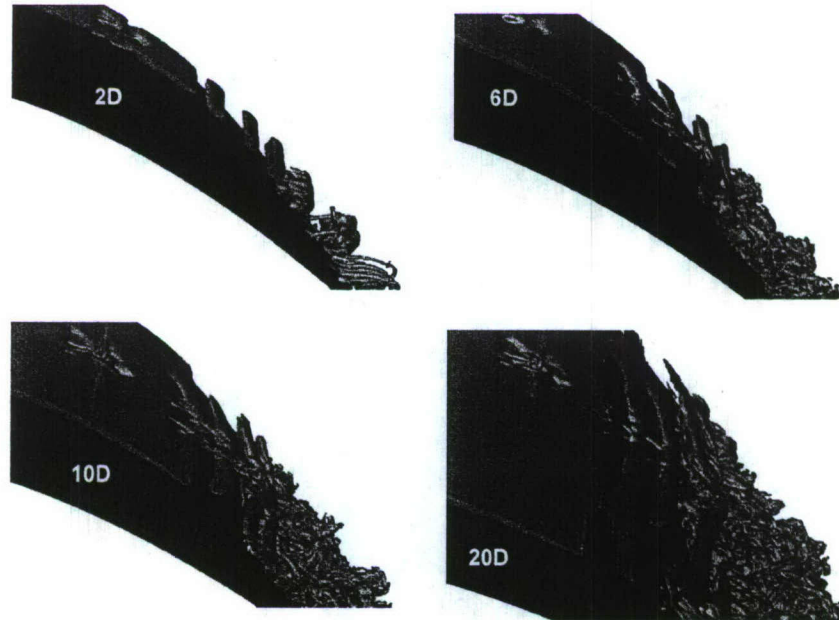


**Fig. 88: Instantaneous visualizations of iso-surfaces of  $\lambda_2=2.5$  for flow control DNS using pulsed VGJs and various hole spacings: 2D (upper left), 6D (upper right), 10D (lower left), 20D (lower right) where  $D$  is the hole diameter.**

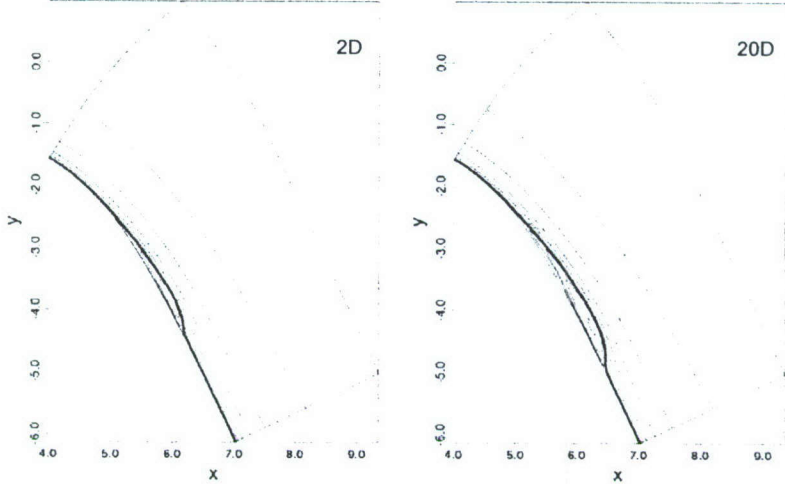


**Fig. 89:** Time- and spanwise averaged streamlines for flow control simulations using pulsed vertical VGJs with small (2 hole diameters, left) and large (20 hole diameters, right) hole spacings.

The results of a POD analysis for all flow fields in this investigation are presented in Figs. 90 and 91. Considering the first POD mode in Fig. 90, we conclude that for all hole spacings the main energy of the flow is organized in and dominated by spanwise coherent structures even in the case of only 2 holes per chord length (case 20D). The eigenvalues plotted in Fig. 91 represent the kinetic energy content in the first 10 POD modes. In all cases the mean flow (mode 0) contains significantly more energy than any of the “unsteady” eigenfunctions. Modes one and two represent the observed spanwise coherent structures. It can be observed that the drop-off in the magnitude of the eigenvalues occurs more gradually for cases of larger hole spacing and more sudden for cases of smaller hole spacing. This implies that the higher POD modes which are three-dimensional in nature become more and more important as the hole spacing is increased. However, even for the largest hole spacing the most energetic flow structures are still two-dimensional. This again is a strong indicator that the 2-D instability mechanism that we identified for the flat plate is of great importance for pulsed VGJ flow control.

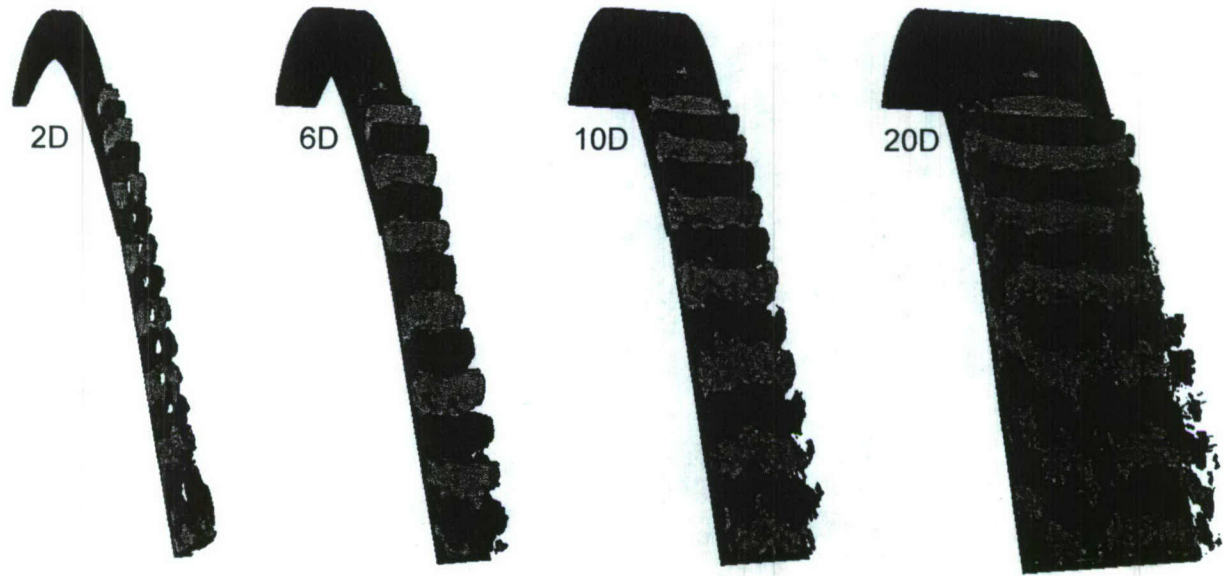


**Fig. 90:** Flow control using pulsed vertical VGJs. POD mode 1 for various hole spacings: 2D (left), 6D (center left), 10D (center right), 20D (right) where  $D$  is the hole diameter.

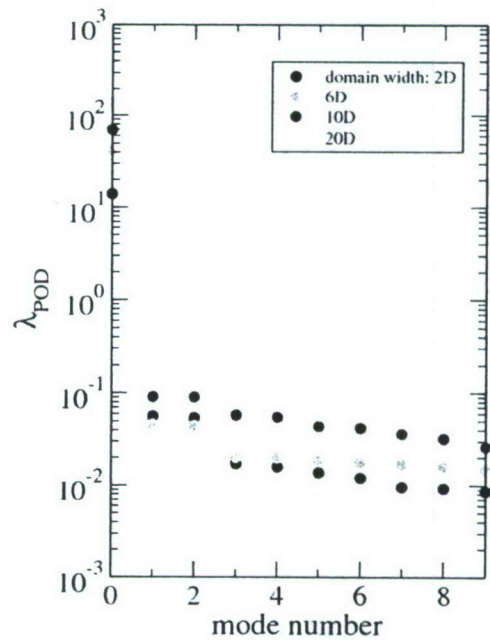


**Fig. 91:** POD eigenvalues for vertical VGJ simulations with different hole spacings.

Next, we investigated how the suppression of spanwise modes by the domain width affected the flow physics. We considered three domains with different spanwise domain extent but equal hole spacing (two hole diameters) for the pulsed VGJ actuators. Schematics of all three setups are depicted in Fig. 92. Due to the applied symmetry conditions the same AFC flow scenario is

computed in all simulations. However, for the integration domain with the smallest spanwise extent (2 hole diameters  $D$ ) waves or structures with a spanwise wavelength of  $4D$  or  $6D$  are suppressed. Mechanisms that would result in an energy transfer to such modes are therefore impossible.

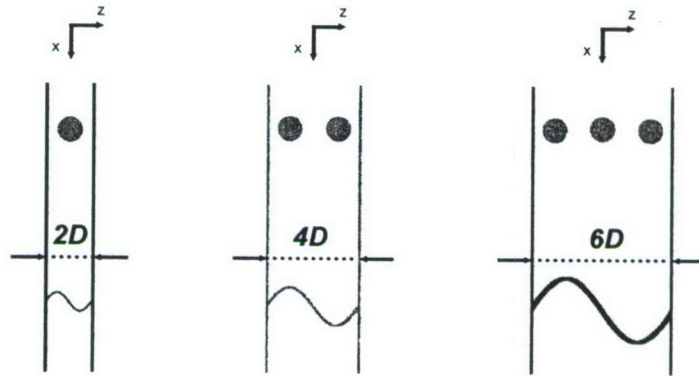


**Fig. 92: Schematics of the computational setup for VGJ simulations with various spanwise domain extents. The hole spacing (two hole diameters) is kept constant in all cases.**

In Fig. 93 results for a hole spacing of  $2D$  and domain width of  $2D$  (left) and for a hole spacing of  $2D$  and a domain width  $6D$  (right) are compared. Here, instantaneous visualizations of iso-surfaces of  $\lambda_2$  are shown. For visualization purposes the results for the narrower domain ( $2D$ ) were repeated once in the positive and negative  $z$ -direction to allow for a better comparison. Fig. 93 shows that the two-dimensional spanwise structures associated with the pulsed VGJs are breaking up much faster for the wider domain whereas transition is delayed for the narrow domain. This lead us to the conclusion that the suppression of modes with higher spanwise wavelengths that cannot be represented by the spectral discretization in the narrower domain is indeed important in the transition process. Such modes should not be excluded.

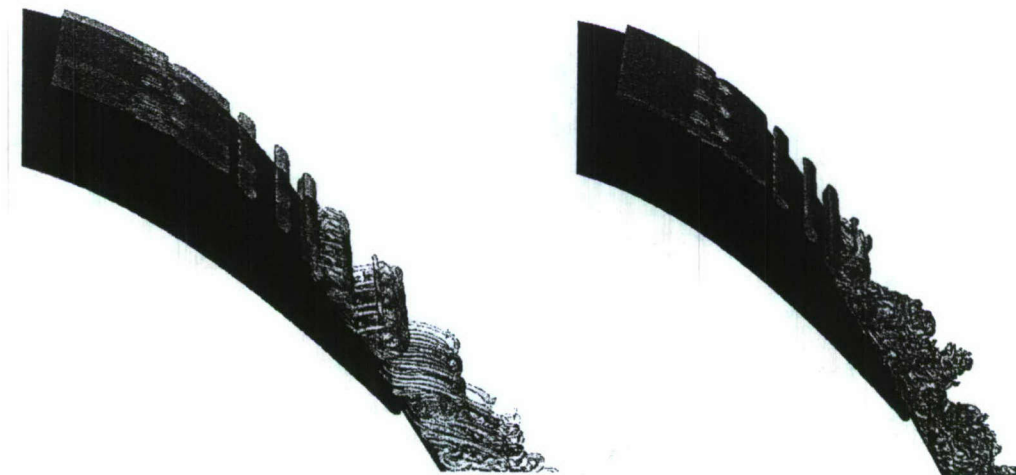


**Fig. 93: Instantaneous visualizations of iso-surfaces of  $\lambda_2=2.5$  for flow control DNS using pulsed VGJs and a constant hole spacing of two hole diameters. Narrow domain (left, 1 hole computed) and a wide domain (right, 3 holes computed). For comparison results on the left were repeated in positive and negative spanwise direction.**

Further prove for this conclusion can be obtained by studying the streamwise development of selected disturbance components for the different cases. Fourier amplitudes of the streamwise velocity component at the “fundamental” frequency (i.e. the forcing frequency  $f=64\text{Hz}$ ) are plotted in Fig. 94. The notation,  $(h,k)$ , is commonly used to identify Fourier modes according to their frequency,  $h$ , and spanwise wavenumber,  $k$ . In Fig. 94, the two-dimensional mode  $(1,0)$  as well as the “first” oblique mode  $(1,1)$  are shown. The highest amplitude levels in all instances are attained by the two-dimensional mode which represent the observed spanwise “rollers”. However, in the transition region the amplitude level of the 2-D mode is twice as large for the narrow domain ( $2D$ , 1 hole computed) when compared to the wide domain ( $6D$ , 3 holes computed). Near the natural separation location, the disturbance mode  $(1,1)$  (and others, not shown here) experience growth rates that are larger than for the two-dimensional mode. These modes correspond to disturbances with twice and three times the spanwise wavelength of the computed hole spacing which were suppressed when the narrow domain was employed. The energy for their growth is provided by the base flow. Although the growth rates are very high all higher modes saturate below the amplitude level of the two-dimensional mode  $(1,0)$  indicating that the turbulent flow is still organized in predominantly two-dimensional structures. However, as discussed earlier there might be cases when three-dimensional, oblique modes are dominating the flow as was observed for the cases with intermediate duty cycles.

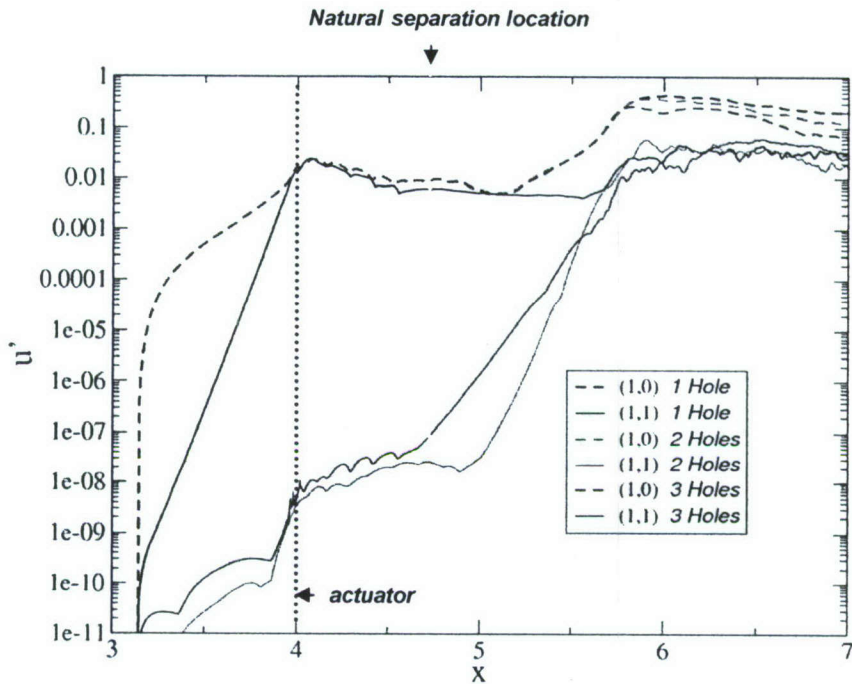


**Fig. 94: Fourier amplitude of the disturbance velocity  $u'$  (max. over y) for one, two and three VGJ actuator holes.**

### 3.4.6 Additional Results

Recently, we also investigated the role of secondary instability mechanisms in both forced and unforced laminar separation bubbles (Fasel et al. 2005, Embacher and Fasel). By employing a local stability analysis of a spatially periodic base flow, we were able to show that the unforced laminar separation bubble can exhibit a strong secondary absolute instability with respect to three-dimensional disturbances resulting in a rapid transition to turbulence (Fig. 95, top). Based on our analytical analysis we determined that by introducing a large amplitude high frequency 2-D disturbance shortly upstream of the separation the 3-D secondary instability could be suppressed and as a consequence transition to turbulence prevented. Even more stunning, by large amplitude 2-D forcing, we were able to relaminarize an already transitioned flow. Obviously, this finding may have profound consequences for practical applications, both for separation, and transition control. This finding was supported by 3-D DNS. Figure 95 (bottom) shows that the flow can be kept laminar over a substantial downstream distance.



*Fig. 95: DNS of laminar separation bubble on flat-plate. Iso-contours of spanwise vorticity. Unforced flow (top) and controlled flow (bottom). Harmonic excitation of 2-D mode at right frequency relaminarizes flow.*

These results encouraged us to investigate new forcing strategies for the LPT geometry. Fig. 96 shows instantaneous flow visualizations (iso-surfaces of  $\lambda_2=-2.5$ ) and instantaneous contours of the spanwise vorticity component  $\omega_z$  for flow control scenarios using a two-dimensional slot and closely spaced VGJ actuators. Harmonic forcing with  $f=64\text{Hz}$  is applied in both cases and the blowing ratio is adjusted such that a constant energy input, i.e.  $c_\mu$ , is maintained. In both cases separation is effectively reduced and transition to turbulence is significantly delayed.



*Fig. 96: Instantaneous iso-surfaces of  $\lambda_2=-2.5$  and contours of instantaneous spanwise vorticity  $\omega_z$  for flow control using a two-dimensional slot (left) and closely spaced VGJ actuators (right).*

#### 4. Summary

With funding from AFOSR we have developed reliable simulation tools that allow us to perform high-fidelity simulations of entire turbine blades (approach 1) and of closely related model problems (approach 2). Using Direct Numerical Simulation (DNS) we demonstrated that the shear layer instability of the separated boundary layer can be exploited for effective flow control. In addition, we were able to show that pulsed VGJs resulted in a “by-pass” transition of the flow leading to reduced flow separation. Harmonic blowing through a slot (similar effect as plasma actuators) was shown to result in the generation of strong spanwise vortices that effectively suppressed separation and also reduced the amplification of 3-D disturbances.

Although these simulations provide valuable insight of why and how the various flow control strategies are effective, only fully resolved direct numerical simulations (DNS) can establish the necessary in-detail understanding of the relevant flow physics. Simulations of a separation bubble as generated by LPT conditions for which all scales of turbulent motion could be resolved enabled us explain the physical mechanisms responsible for separation control by steady and pulsed VGJs. The stunning effectiveness of pulsed VGJs could be attributed to the exploitation of a hydrodynamic instability of the separated boundary layer leading to an exponential amplification of the 2-D disturbance wave component. The energy required for this amplification is provided by the base-flow (instead of the actuator input) and therefore is “free of charge”. As a result, the VGJs can be operated at a relatively small blowing ratio and with a small duty cycle resulting in significant savings in the energy expense required for the actuation.

In summary, we obtained a clear understanding of the relevant physical mechanism governing separation control by steady and pulsed VGJs. However, these results should by no means be considered entirely conclusive. A much broader parameter range has to be investigated in order to substantiate the findings from our research and to scientifically support the conjectures regarding some of the fundamental mechanisms that we have found. Furthermore it is encouraged to explore the “universality” of these findings for a real LPT turbine operating environment which is characterized by (among others) wakes generated by upstream stages, free-stream turbulence (FST) resulting from the combustor, and wall roughness. We also believe that considerable further improvements in control effectiveness are possible as other instability mechanisms may be exploited (see for example “oblique” coherent structures).

## 5. CONFERENCES, PRESENTATIONS, AND PAPERS

*This research grant resulted in the following publications:*

- Gross, A., Fasel, H.F., "High-Order-Accurate Numerical Method for Complex Flows," AIAA Journal, Volume 46, Issue 1, 2008, pp. 204-214
- Gross, A., Fasel, H., "Self-Adaptive Closed-Loop Control of Low-Reynolds Number Laminar Separation," AIAA-2007-3913, 25th AIAA Applied Aerodynamics Conference, 25 - 28 Jun 2007, Miami, FL
- Balzer, W., Gross, A., Fasel, H.F., "Active Flow Control of Low-Pressure Turbine Separation," Proceedings of the HPCMP Users Group Conference 2007, June 18-21, 2007, Pittsburgh, PA, editor: D.E. Post, pages 73-82
- Fasel, H.F., Balzer, W., and Gross, A., "Numerical Investigation of Active Control for Low-Pressure Turbine Blades," Minnowbrook V 2006 Workshop on Unsteady Flows in Turbomachinery, NASA/CP-2006-214484, December 2006, eds. J.E. LaGraff, D.E. Ashpis, M.L.G. Oldfield, and J.P. Gostelow, pages 51-52
- Embacher, M. and Fasel, H.F., 2007, "Absolute Secondary Instability in Laminar Separation Bubbles: A Local and Global Analysis Using Direct Numerical Simulations," Submitted to J. Fluid Mech.
- Gross, A., and Fasel, H.F., "Control-Oriented Proper Orthogonal Decomposition Models for Unsteady Flows," AIAA Journal, Volume 45, Issue 4, 2007, 814-827
- Gross, A., Fasel, H.F., "Investigation of Low-Pressure Turbine Separation Control," AIAA-2007-520, 45th AIAA Aerospace Sciences Meeting and Exhibit, 8-11 January 2007, Reno, Nevada
- Gross, A., Fasel, H.F., "Characteristic Ghost Cell Boundary Condition," AIAA Journal, Volume 45, Issue 1, 2007, 302-306
- Brehm, C., Gross, A., Fasel, H.F., "Closed-Loop Control of Low-Pressure Turbine Laminar Separation," AIAA-2006-3021, 3rd AIAA Flow Control Conference, 5-8 June 2006, San Francisco, California
- Gross, A., Fasel, H.F., "Reduced Order Models for Closed-Loop Control of Time-Dependent Flows," AIAA-2006-1403, 44th AIAA Aerospace Sciences Meeting and Exhibit, 9-12 January 2006, Reno, Nevada
- Gross, A., Fasel, H.F., "Numerical Investigation of Low-Pressure Turbine Blade Separation Control," AIAA Journal, Volume 43, Issue 12, 2005, 2514-2526
- Fasel, H.F., Postl, D., Gross, A., (Invited) "Instability and Control of Laminar Separation Bubbles: Direct Numerical Simulations," 3rd Symposium on Global Flow Instability and Control, 27-30 September 2005, Hersonissos, Crete
- Gross, A., Fasel, H.F., "Turbulence modeling for low pressure turbine blades," AIAA-2005-5292, 35th AIAA Fluid Dynamics Conference and Exhibit, 6-9 June 2005, Toronto, Ontario, Canada

## REFERENCES

- Abdessemed, N., Sherwin, S., and Theofilis, V., 2004, "On Unstable 2D Basic States in Low-pressure Turbine Flows at Moderate Reynolds Numbers," AIAA-2004-2541.
- Abdessemed, N., Sherwin, S., and Theofilis, V., 2006, "Linear Stability of the flow past a low-pressure turbine blade," AIAA-2006-3530.
- Bake, S., Meyer, D.G.W., and Rist, U., 2002, "Turbulence Mechanism in Klebanoff Transition: A Quantitative Comparison of Experiment and Direct Numerical Simulation," *J. Fluid Mech.* 459: 217-243.
- Bons, J.P., Sondergaard, R., and Rivir, R.B., 1999, "Control of Low-Pressure Turbine Separation Using Vortex Generator Jets," AIAA-99-0367.
- Bons, P.B., Sondergaard, R., and Rivir, R.B., 2000, "Turbine Separation Control Using Pulsed Vortex Generator Jets," Proceedings TURBOEXPO 2000, Munich, Germany, May 8-11.
- Bons, J.P., Sondergaard, R., and Rivir, R.B., 2001a, "Turbine Separation Control Using Pulsed Vortex Generator Jets," *Transactions of the ASME* 198, Vol. 123.
- Bons, J.P., Sondergaard, R., and Rivir, R.B., 2001b, "The Fluid Dynamics of LPT Blade Separation Control Using Pulsed Jets," Proceedings of TURBOEXPO 2001, New Orleans, LA.
- Bons, J.P., Taylor, R.P., McClain, S.T., and Rivir, R.B., 2001c, "The Many Faces of Turbine Surface Roughness," *J. of Turbomachinery*, 123: 739-748.
- Bons, J.P., 2002, "St and cf Augmentation for Real Turbine Roughness With Elevated Free-stream Turbulence," *J. of Turbomachinery*, 124: 632-644.
- Bons, J.P., Hansen, L.C., Clark, J.P., Koch, P.J., and Sondergaard, R., 2005, "Designing Low-Pressure Turbine Blades with Integrated Flow Control," Proceedings of GT2005, ASME Turbo Expo 2005: Power for Land, Sea, and Air, June 6-9, 2005, Reno-Tahoe, NV.
- Brehm, C., Gross, A., Fasel, H.F., 2006, "Closed-Loop Control of Low-Pressure Turbine Laminar Separation," AIAA-2006-3021
- Clark, J.P., 2004, "An integrated Design, Analysis, and Optimization System for Turbine Airfoils," AFRL Internal Report.
- Corke, C., and Post, M.L., 2005, "Overview of Plasma Flow Control: Concepts, Optimization, and Applications," AIAA-2005-0563.
- Dong, Y. and Cumpsty, N.A., 1990, "Compressor Blade Boundary Layer: Part2 – Measurements with incident wakes," *J. of Turbomachinery*, 112: 231-241.
- Dunn, M.G., 2001, "Convective Heat Transfer and Aerodynamics in Axial Flow Turbines," *J. of Turbomachinery*, 123: 637-686
- Duraiswami, R. and Prosperetti, A., 1992, "Orthogonal mapping in two dimensions," *J. Comp. Phys.*, 98: 254-268.
- Eldredge, R., and Bons, J., 2004, "Active Control of a Separating Boundary Layer with Steady Vortex Generating Jets," AIAA-2004-0751.
- Embacher, M. and Fasel, H.F., 2007, "Absolute Secondary Instability in Laminar Separation Bubbles: A Local and Global Analysis Using Direct Numerical Simulations," Submitted to *J. Fluid Mech.*
- Fasel, H., 1976, "Investigation of the Stability of Boundary Layers by a Finite Difference Model of the Navier-Stokes Equations," *J. Fluid Mech.* 78:355-383.
- Fasel, H. and Kral, L.D., 1989, "Numerical Investigation of the Control of the Secondary Instability Process in Boundary Layers," AIAA-89-0984.
- Fasel, H., Rist, U., and Konzelmann, U., 1991, "Numerical Investigation of the Three-Dimensional Development in Boundary-Layer Transition," *AIAA J.*, 28:29-37.

- Fasel, H.F., Seidel, J., and Wernz, S., 2002a, "A Methodology for Simulations of Complex Turbulent Flows," *Journal of Fluids Engineering*, 124(4): 933-942.
- Fasel, H., 2002b, "Numerical Investigation of the Interaction of the Klebanoff Mode with Tollmien-Schlichting Waves," *J. Fluid Mech.*, 450:1-33.
- Fasel, H.F., Postl, D., Gross, A., (Invited), 2005, "Instability and Control of Laminar Separation Bubbles: Direct Numerical Simulations," 3rd Symposium on Global Flow Instability and Control, 27-30 September 2005, Heronissos, Crete.
- Goldstein, D., Handler, R., and Sirovich, L., 1993, "Modeling a no-slip flow boundary with an external force field," *J. Comp. Phys.*, 105(2): 354-366.
- Gaster, M., 2003, "The Influence of Surface Roughness on Boundary Layer Transition," *Symposium on Advances in Fluid Mechanics*.
- Gross, A., Fasel, H., 2002, "High-Order WENO Schemes Based on the Roe Approximate Riemann Solver," *AIAA-2002-2735*.
- Gross, A., and Fasel, H.F., 2005a, "Numerical investigation of low-pressure turbine blade separation control," *AIAA J.*, 43(12): 2514-2525.
- Gross, A., and Fasel, H.F., 2005b, "Simulation of Active Flow Control for a Low Pressure Turbine Blade Cascade," *AIAA-2005-0869*.
- Gross, A., and Fasel, H.F., 2007a, "Characteristic Ghost Cell Boundary Condition," *AIAA J.*, 45(1): 302-306.
- Gross, A., and Fasel, H., 2007b, "Investigation of Low-Pressure Turbine Separation Control," *AIAA-2007-520*.
- Gross, A., Fasel, H., 2007c, "Self-Adaptive Closed-Loop Control of Low-Reynolds Number Laminar Separation," *AIAA-2007-3913*
- Gross, A., Fasel, H.F., "High-Order-Accurate Numerical Method for Complex Flows," *AIAA Journal*, Volume 46, Issue 1, 2008, pp. 204-214
- Halfon, E., Nishri, B., Seifert, A., Wygnanski, I., 2004, "Effects of Elevated Free-Stream Turbulence on Actively Controlled Separation Bubble", *J. Fluid Eng.*, 126: 1015-1024.
- Hansen, L., and Bons, J., 2006, "Flow Measurements of Vortex Generator Jets in Separating Boundary Layer," *Journal of Propulsion and Power*, 22(3): 558-566.
- Hipp-Kalthoff, C. and Fasel, H., 1990, "Numerical Simulations of Two-Dimensional Temporal and Spatial Free Shear Layers: A Comparison," *Proceedings of the IUTAM Symposium on Separated Flows and Jets*, Novosibirsk, USSR, July 9-13 (Eds. V. V. Kozlov, and A. V. Dovgal), Springer:617-628.
- Hourmouziadis, J., 2000, "Das DFG Verbundvorhaben Instationäre Strömung in Turbomaschinen," Deutscher Luft- und Raumfahrtkongress, Leipzig, Germany, September 18-21, DGLR-JT2000-030.
- Howell, R.J., Hodsun, H.P., Schulte, V., Stieger, R.D., Schiffer, H.-P., Haselbach, F., and Harvey, N.W., 2002, "Boundary Layer Development in the BR710 and BR715 LP Turbine – The Implementation of High-Lift and Ultra-High-Lift Concepts," *J. of Turbomachinery*, 124: 385-392.
- Huang, J., Corke, T., and Thomas, F., 2003, "Plasma Actuators for Separation Control of low pressure turbine Blades," *AIAA-2003-1027*.
- Huang, J., Corke, T.C., and Thomas, F.O., 2006a, "Plasma Actuators for Separation Control of Low-Pressure Turbine Blades," *AIAA Journal*, 44(1): 51-57.
- Huang, J., Corke, T.C., and Thomas, F.O., 2006b, "Unsteady Plasma Actuators for Separation Control of Low-Pressure Turbine Blades," *AIAA Journal*, 44(7): 1477-1487.
- Hunt J.C.R., Wray A.A., and Moin P., 1988, "Eddies, stream, and convergence zones in turbulent flows," Report CTR-S88, Center For Turbulence Research, Stanford, California.

- Jeong, J., and Hussain, F. 1995, "On the Identification of a Vortex," *J. Fluid Mech.*, 285: 69-94.
- Kalitzin, G., Wu, X., and Durbin, P.A., 2003, "DNS of fully turbulent flow in a LPT passage," *Int. J. Heat & Fluid Flow*, 24: 636-644.
- Klebanoff, P.S., and Tidstrom, K.D., 1972, "Mechanism by Which a Two-Dimensional Roughness Element Induces Boundary-Layer Transition," *Physics of Fluids*, 15(7): 1173-1188.
- Kloker, M. and Fasel, H. 1989, "Numerical Simulation of Two- and Three-Dimensional Instability Waves in Two-Dimensional Boundary Layers with Streamwise Pressure Gradient," In *Laminar-Turbulent Transition, Proceedings of the IUTAM Symposium*, Toulouse, France, Sept. 11-15 (Eds. D. Arnal and R. Michel), Springer.
- Kloker, M. and Fasel, H., 1994, "Direct Numerical Simulation of Boundary Layer Transition Under Strong Adverse Pressure Gradient," *Proceedings of the IUTAM Symposium on Laminar Turbulent Transition*, Sendai, Japan, Sept. 5-9 (Ed. R. Kobayashi), Springer: 481-488.
- Kral, L.D. and Fasel, H., 1994, "Direct Numerical Simulation of Passive Control of Three-Dimensional Phenomena in Boundary Layer Transition Using Wall Heating," *J. Fluid Mech.* 264:213-254.
- Lardeau, S., and Leschziner, M.A., 2004, "Unsteady Reynolds-Averaged Navier-Stokes Computations of Transitional Wake/Blade Interaction," *AIAA J.*, Vol. 42(8): 1559-1571.
- Linnick, M.N., and Fasel, H.F., 2005, "A high-order immersed interface method for simulating unsteady incompressible flows on irregular domains," *J. Comp. Phys.*, 204(1): 157 – 192.
- Lodefier, K., and Dick, E., 2005, "Modeling of Unsteady Transition in Low-Pressure Turbine Blade Flows with Two Dynamic Intermittency Equations," *Flow, Turbulence and Combustion*, 76: 103-132.
- Lumley, J.L., 1967, "The Structure of Inhomogeneous Turbulent Flows," *Atmospheric turbulence and radio wave propagation*, Nauka, Moscow and Toulouse, France, eds. A.M. Yaglom and V.I. Tatarsky: 166-178.
- Margolin, L.G., and Rider, W.J., "A rationale for implicit turbulence modeling," *Int. J. Numer. Meth. Fluids*, Vol. 39, 2002, pp. 821-841
- Meitz, H.L. and Fasel, H., 1994, "Numerical Simulation of Boundary-Layer Flow Over Suction Holes," In *Laminar-Turbulent Transition, Proceedings of the IUTAM Symposium on Laminar Turbulent Transition*, Sendai, Japan, Sept. 5-9 (Ed. R. Kobayashi), Springer:237-244.
- Meitz, H.L. and Fasel, H., 2000, "A Compact-Difference Scheme for the Navier-Stokes Equations in Vorticity-Velocity Formulation," *J. Comp. Phys.* 157:371-403.
- Michelassi, V., Wissink, J.G., Fröhlich, J., and Rodi, W., 2003, "Large-Eddy Simulation of Flow Around Low-Pressure Turbine Blade with Incoming Wakes," *AIAA J.*, 41(11): 2143-2156.
- Morkovin, M.V., 1969, "The many faces of transition," In *Viscous Drag Reduction* (ed. C.S. Wells). Plenum Press.
- Morkovin, M.V., 1979, "On the Question of Instabilities Upstream of Cylindrical Bodies," NASA, CR-323.
- Nagarajan, S., Lele, S.K., Ferziger, J.H., 2007, "Leading-edge effects in bypass transition," *J. Fluid Mech.*, 572: 471-504.
- Postl, D., Gross, A., and Fasel, H.F., 2003, "Numerical Investigation of Low-Pressure Turbine Blade Separation Control," *AIAA-2003-0614*.
- Postl, D. Gross, A., and Fasel, H.F., 2004, "Numerical Investigation of Active Flow Control for Low-Pressure Turbine Blade Separation," *AIAA-2004-0750*.
- Reimann, D., Bloxham, M., Crapo, K., Pluim, J., and Bons, J., 2006, "Influence of Vortex Generator Jet-Induced Transition on Separating Low Pressure Turbine Boundary Layers," *AIAA-2006-2852*.
- Reimann, D., Pluim, J., and Bons, J., 2007, "Influence of Two-Dimensional vs. Discrete Disturbances on Separating Low Pressure Turbine Boundary Layers," *AIAA-2007-525*.
- Reshotko, E., and Leventhal, L., 1981, "Preliminary Experimental Study of Disturbances in a Laminar

- Boundary-Layer due to Distributed Surface Roughness," AIAA-81-1224.
- Reshotko, E., and Tumin, A., 2001, "Role of Transient Growth in Roughness-Induced Transition," AIAA J., 42(4): 766-77.
- Rist, U. and Fasel, H., 1995, "Direct Numerical Simulation of Controlled Transition in a Flat-Plate Boundary Layer," J. Fluid Mech. 298:211-248.
- Rizzetta, D.P., and Visbal, M.R., 2003, "Numerical Investigations of Transitional Flow Through a Low-Pressure Turbine Cascade," AIAA-2003-3587.
- Rizzetta, D.P., and Visbal, M.R., 2004, "Numerical Simulation of Separation Control for a Transitional Highly-Loaded Low-Pressure Turbine," AIAA-2004-2204.
- Rizzetta, D.P., and Visbal, M.R., 2005, "Numerical Simulation of Separation Control for Transitional Highly Loaded Low-Pressure Turbines," AIAA Journal, 43(9): 1958-1967.
- Rizzetta, D.P., and Visbal, M.R., 2007, "Numerical Investigation of Plasma-Based Flow Control for a Transitional Highly-Loaded Low-Pressure Turbine," AIAA-2007-938.
- Roberts, S.K., and Yaras, M.I., 2005, "Boundary Layer Transition Affected by Surface Roughness and Free-Stream Turbulence," J. of Turbomachinery, 127: 449-457.
- Roberts, S.K., and Yaras, M.I., 2006, "Effects of Surface-Roughness Geometry on Separation-Bubble Transition," J. of Turbomachinery, 128: 349-356.
- Rumsey, C.L., and Gatski, T.B., 2001, "Recent Turbulence Model Advances Applied to Multielement Airfoil Computations" J. of Aircraft, 38(5): 904-910.
- Schlichting, H., and Gersten, K., 2000, "Boundary Layer Theory," 8th edition, Springer, pp. 292, 353, 354.
- Schubauer, G.B., and Klebanoff, P.S., 1956, "Contributions on the Mechanics of Boundary-Layer Transition," NACA Report 1289.
- Seidel, J. and Fasel, H., 2001, "Numerical investigations of heat transfer mechanisms in the forced laminar wall jet," J. Fluid Mech. 442:191-215.
- Sharma, O., 1998, "Impact of Reynolds Number on LP Turbine Performance," Proceedings of the 1997 Minnowbrook II Workshop on Boundary Layer Transition in Turbomachines, NASA CP-1998-206958: 65-69.
- Sirovich, L., 1987, "Turbulence and the Dynamics of Coherent Structures," Quarterly of Applied Mathematics, XLV(3): 561-590.
- Sohn, K.H., Shyne, R.J., DeWitt, K.J., 1998, "Experimental Investigation of Boundary Layer Behavior in a Simulated LowPressure Turbine," NASA/TM 1998-207921
- Sondergaard, R., Bons, J.P., Rivir, R.B., 2002a, "Control of Low-Pressure Turbine Separation Using Vortex Generator Jets," Journal of Propulsion and Power 18 (4): 889-895.
- Sondergaard, R., Bons, J.P., Sucher, M., Rivir, R.B., 2002b, "Reducing Low-Pressure Turbine Stage Blade Count Using Vortex Generator Jet Separation Control," Proceedings of TURBOEXPO 2002, Amsterdam, The Netherlands, June 3-6.
- Spalart, P. R., Jou, W.-H., Strelets, M., and Allmaras, S. R., 1997, "Comments on the Feasibility of LES for Wings and on the Hybrid RANS/LES Approach," Advances in DNS/LES, Proceedings of the First AFOSR International Conference on DNS/LES.
- Spalart, P.R., Deck, S., Shur, M.L., Squires, K. D., Strelets, M.K., and Travin, A., 2006, "A New Version of Detached-eddy Simulation, Resistant to Ambiguous Grid Densities," Theoretical and Computational Fluid Dynamics 20(3): 181-195.
- Spall, J.C., 1992, "Multivariate Stochastic Approximation Using a Simultaneous Perturbation Gradient Approximation," IEEE Transactions on Automatic Control, Vol. 37, No. 3, 1992, pp. 332-341
- Spall, J.C., 1997, "A One-measurement Form of Simultaneous Perturbation Stochastic Approximation,"

Automatica, Vol. 33, No. 1, 1997, pp. 109-112

Speziale, C.G., 1998, "Turbulence Modeling for Time-Dependent RANS and VLES: A Review," AIAA J., 36(2): 173-184.

Stieger, R.D., Vera, M., Zhang, X.F., and Hodson, H.P., "Transition Mechanisms and the Use of Surface Roughness to Enhance the Benefits of Wake Passing in LP Turbines," Proceedings of the 2003 Minnowbrook IV Workshop on Transition and Unsteady Aspects of Turbomachinery Flows, NASA TM-2004-212913, eds. J.E. LaGraff and D.E. Ashpis, August 2004: 40-41.

Suzen, Y.B., and Huang, P.G., 2004, "Numerical Simulation of Transitional Flows as Affected by Passing Wakes," AIAA-2004-0103.

Theofilis, V., and Sherwin, S.J. , 2004, "Global Instability and Control of Low-Pressure Turbine Flows," Proceedings of the 2003 Minnowbrook IV Workshop on Transition and Unsteady Aspects of Turbomachinery Flows, NASA TM-2004-212913, eds. J.E. LaGraff and D.E. Ashpis, August 2004: 31-32.

Volino, R.J., 2002a "Separated Flow Transition Under Simulated Low-Pressure Turbine Airfoil Conditions – Part 1: Mean Flow and Turbulence Statistics," J. of Turbomachinery, 124: 645-655.

Volino, R.J., 2002b "Separated Flow Transition Under Simulated Low-Pressure Turbine Airfoil Conditions – Part 2: Turbulence Spectra," J. of Turbomachinery, 124: 656-664.

Wang, Z.J., Chi, X.K., Shih, T., Bons, J., "Direct Simulation of Surface Roughness Effects with RANS and DES Approaches on Viscous Adaptive Cartesian Grids," AIAA-2004-2420.

Wernz, S. and Fasel, H., 1997, "Numerical Investigation of Forced Transitional Wall Jets," AIAA-97-2022.

Wernz, S. and Fasel, H., 1999, "Numerical Investigation of Resonance Phenomena in Wall Jet Transition," In Laminar-Turbulent Transition, Proceedings of the IUTAM Symposium, Sedona, AZ, Sept. 13-17 (Eds. H. F. Fasel and W. S. Saric), Springer: 215-222.

Wissink, J.G., Rodi, W., Hodson, H.P., 2006a, "The influence of disturbances carried by periodically incoming wakes on the separating flow around a turbine blade," Int. J. Heat & Fluid Flow, 27:721-729.

Wissink, J.G., Rodi, W., 2006b, "Direct Numerical Simulations of Transitional Flow in Turbomachinery," J. of Turbomachinery, 128: 668-678.

Wolff, S., Brunner, S., and Fottner, L., 2000, "The Use of Hot-Wire Anemometry to Investigate Unsteady Wake-Induced Boundary-Layer Development on a High-Lift LP Turbine Cascade," J. of Turbomachinery, 122: 644-650.

Wu, X., Jacobs, R.G., Hunt, J.C.R., and Durbin, P.A., 1999, "Simulation of boundary layer transition induced by periodically passing wakes," J. Fluid Mech., 398: 109-153.

Wu, X., and Durbin, P.A., 2001, "Evidence of longitudinal vortices evolved from distorted wakes in a turbine passage," J. Fluid Mech., 446: 199-228.

Zhang, X.F., and Hodson, H., 2005, "Combined Effects of Surface Trips and Unsteady Wakes on the Boundary Layer Development of an Ultra-High-Lift LP Turbine Blade," J. of Turbomachinery, 127: 479-488.